



**structure  
and  
shear  
in a  
cohesive  
powder**



## Stellingen

behorende bij het proefschrift  
"Structure and shear in a cohesive powder"  
van R.J.M. Janssen

1. Het gebruik van de term "steady-state" in relatie tot het stromen van poeder kan microscopisch gezien niet standhouden.
2. Het afschuifvlak in een cohesief poeder opgelegd door een "direct shear tester" is veel breder dan 10 deeltjesdiameters.
3. De "flow function" is geen eenduidige karakteristiek voor het stromingsgedrag van een poeder.
4. Elk poeder vertoont "stick-slip" gedrag.
5. De uit de grondmechanica bekende cilindrische triaxiale tester heeft slechts biaxiale controle omdat de derde principiële spanning azimuthaal gericht is.
6. ... no physical theory begins with formulae but rather with ideas and notions ... (Einstein and Infeld, 1958)
7. Een echte muzikfan weet welke CD's hij niet bezit.
8. Ni sama be mogo min gne, nomi t'i bugo. (Afrikaans spreekwoord)  
(He who rides an elephant is not dampened by the dew)
9. De term "wereldmuziek" doet tekort aan de veelheid en rijkheid aan muzikale stijlen die deze term omvat.
10. Beleid dat erop gericht is het gevoel van veiligheid te vergroten zonder de veiligheid zelf aan te pakken, mist zijn doel.
11. Pure objectiviteit is niet menselijk.

## Stellingen (English version)

belonging to the thesis  
"Structure and shear in a cohesive powder"  
of R.J.M. Janssen

1. The use of the term "steady-state" in relation to the flow of powder is not correct from a microscopic view.
2. The shear region within a cohesive powder, as applied by a direct shear tester, is much wider than 10 particle diameters.
3. The flow function is not an unambiguous characteristic of the flow behavior of a powder.
4. Each powder exhibits "stick-slip" behavior.
5. The cylindrical triaxial tester, which is commonly used in soil mechanics, has only biaxial control because the third principal stress is azimuthal.
6. ... no physical theory begins with formulae but rather with ideas and notions ... (Einstein and Infeld, 1958)
7. A real music fan knows which CD's he doesn't own.
8. Ni sama be mogo min gne, nomi t'i bugo. (African saying)  
(He who rides an elephant is not dampened by the dew)
9. The term "worldmusic" is deficient with respect to the multitude and richness of the musical styles which it contains.
10. Policy that is aimed at increasing the awareness of safety without considering safety itself, misses its goal.
11. Pure objectivity is not human.

3808  
765912

# Structure and shear in a cohesive powder

TR3804

PROEFSCHRIFT



ter verkrijging van de graad van doctor  
aan de Technische Universiteit Delft,  
op gezag van de Rector Magnificus prof. ir. K.F. Wakker,  
voorzitter van het College voor Promoties  
in het openbaar te verdedigen op maandag 17 december 2001 om 16:00 uur

door

Richard Johannes Matheus JANSSEN

scheikundig ingenieur

geboren te Margraten

Dit proefschrift is goedgekeurd door de promotor:  
Prof. B. Scarlett M.Sc.

Samenstelling promotiecommissie:

Rector Magnificus,  
Prof. B. Scarlett, M.Sc.,  
Prof. Dr.-Ing. J. Schwedes,  
Prof. D. Muir Wood,  
Prof. dr. ir. G. Ooms,  
Prof. G. Ferrari,  
Dr. M. Th. Rekveldt,  
Dr. E. Grolman,

voorzitter  
Technische Universiteit Delft, promotor  
Technische Universität Braunschweig  
University of Bristol  
Technische Universiteit Delft  
Università degli Studi di Salerno  
Technische Universiteit Delft  
DSM Research

Published and distributed by:

Delft University Press  
P.O. Box 98  
2600 MG Delft  
The Netherlands  
DUP@library.tudelft.nl

ISBN 90-407-2241-2

COPYRIGHT © 2001 BY R.J.M. JANSSEN

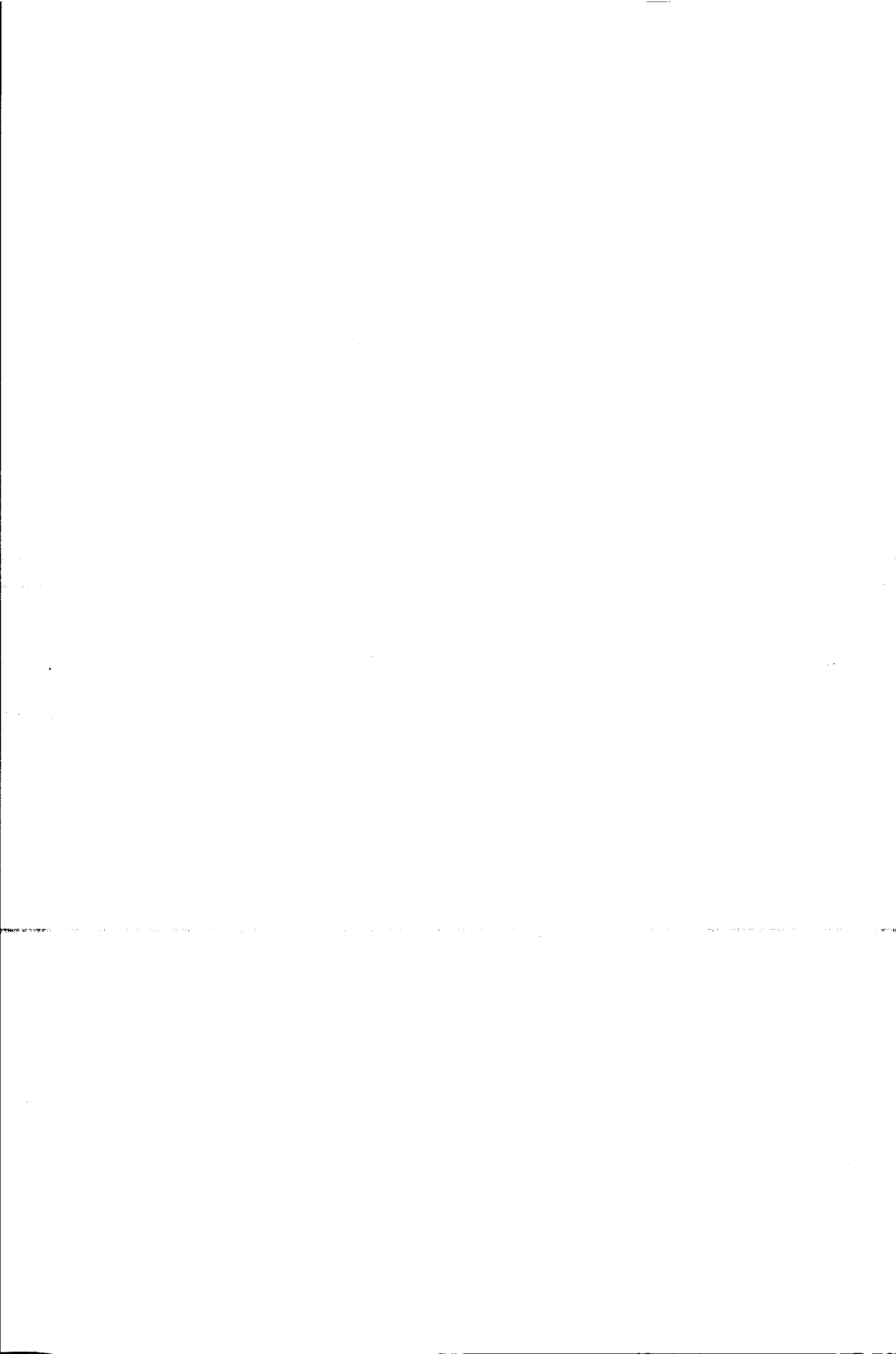
All rights reserved. No part of the material protected by this copyright notice may be reproduced or utilized in any form or by any means, electronic or mechanical, including photocopying, recording or by any information storage and retrieval system, without written permission from the publisher: Delft University Press.

*Veur pap en mam.*

*Cover by Erik Thomassen*

*"Of all the two hundred thousand million men, women and children who, from the beginning of the world, have ever walked on wet sand, how many, ..., if asked, 'Is the sand compressed under your foot?' would have answered otherwise than 'Yes'?"*

*Lord Kelvin, Baltimore Lectures 1904.*





# Abstract

Handling of powders and granular materials is of great importance to industry. However, the knowledge of many powder related processes in industry is poor. This thesis deals with one of those processes that is characterized by a very slow progress: the flow behavior of powder. The basic knowledge in this area is based on a procedure and a tester that Jenike designed in the early 1960s. Many other powder flow testers have been developed after that, but most of these used Jenike's principles, e.g. the yield locus. The yield locus describes the stress that is needed to break a powder sample, i.e. make it flow, as a function of the history of that sample. The definition of the yield locus is an example of the lack of knowledge on the relation between microscopic properties of the particles and the macroscopic behavior of the powder. In the microscopic view, particles are moving and orientating and they form contacts with other particles. These processes are influenced by the particle size, shape and the material of the particles. One can imagine that the relation between the microscopic behavior of the particles and the resulting macroscopic properties of the powder is very complex. The yield locus does not use any direct information about the microscopic state and therefore, it is not surprising that it lacks accuracy in describing powder flow. The aim of this work is to enhance the knowledge about the flow behavior of cohesive powder focussing on the shear zones and on the structure in powder.

Shear regions form when a powder flows and these are the regions in which most of the movement of the particles is thought to take place. In literature (Scarlett et al. 1968 among others) the rule of thumb for the width of such a shear region in cohesionless powder is 10 particle diameters. In this thesis the shear region in a simple direct shear tester has been investigated with the Neutron Depolarization technique. This method is very powerful because it gives information about the rotations of the particles, the porosity, and the shape and width of the shear region.

It has been shown that in a mixture of cohesive BCR-limestone and 3 weight % Ferroxdure the shear region is about 1000 to 2000 particle diameters wide. The particles in the shear region rotate proportionally with the applied shear deformation in a preferred direction. Less rotation and without a preferred direction occurred when the sample was only consolidated. The shear region appeared to be lens shaped from the Neutron Depolarization technique, but direct observation revealed a wave shaped zone. The latter pattern has been seen by other researchers (Schwedde, 1971). The assumption that is made for many direct shear testers - that the shear zone is horizontal and flat - is invalid.

---

In the fundamental investigation of the flow of cohesive BCR-limestone the Flexible Wall Biaxial Tester (Kraan, 1996) has been used. It has been shown that the stress curve of a biaxial consolidation is higher than that of a uniaxial consolidation. This is due to the deviatoric stress or strain that is higher in the uniaxial consolidation and probably facilitates the rearrangement of particles. In comparison with the Braunschweig Biaxial Tester it has been remarked that the spread in the consolidation curves versus the bulk density is quite large. However, the relation between the major and minor principal stress does agree very well for both the biaxial and the uniaxial consolidation.

The classical characteristic that describes powder flow is the flow function. The standard flow function for BCR-limestone (Akers, 1992) has been shown to deviate from the flow function measured with the Flexible Wall Biaxial Tester. This deviation is due to time consolidation in the Flexible Wall Biaxial Tester. The flow function has been proven to be dependent on the intermediate principal stress. Therefore, it is concluded that the definition of the unconfined yield strength is incomplete because it does not include the intermediate principal stress.

Anisotropy also influences the flow function. A 90 degree rotation in the direction of the major principal stress in the determination of the unconfined yield strength reduced the flow function. This cannot be explained by the existing theory. The reason is that an important parameter is missing in the existing theory: the structure of the particles in the powder. The effect of an induced structure is shown by investigating the powder with different strain deformations while the total volume has been kept constant. In these experiments indications have been found that the powder behaves inhomogeneously and therefore locally non-coaxiality of the principal axes of stress and strain could occur. This non-coaxiality has been shown by Wong and Arthur (1985) for non-cohesive sand. A specialized tester is needed to investigate non-coaxiality in cohesive powder more accurate.

The structure in an assembly of particles has been investigated by simulating them with the 3DSHEAR code of Walton and Braun (1986a, 1986b). These simulations proved that the difference between a biaxial and a uniaxial consolidation curve of cohesionless particles is caused by the directional distribution of the normals of the particle contacts. Also a shear region in a direct shear tester has been simulated. The width of that shear region agrees with literature for non-cohesive materials, but not with the Neutron Depolarization experiments done on BCR-limestone. The reason for this difference is probably cohesion.

Future research on powder flow should now focus on the structure in powder. The porosity of an assembly of particles is a scalar and fails to describe the total structure. It is believed that the combination of discrete element simulations of non-spherical particle assemblies together with the development of sophisticated triaxial testers will lead to the full perception of powder flow.

# Contents

<b>ABSTRACT</b>	<b>V</b>
<b>INTRODUCTION</b>	<b>1</b>
1.1 Powder handling.....	1
1.2 Flow behavior of powders.....	2
1.3 Aim and outline of this thesis.....	2
<b>CONCEPTS OF POWDER FLOW BEHAVIOR</b>	<b>5</b>
2.1 Introduction.....	5
2.2 Stress, strain and structure.....	5
2.2.1 The state of stress.....	6
2.2.2 The state of strain.....	8
2.2.3 The state of structure.....	9
2.3 Soil mechanics.....	9
2.4 Powder flow theory.....	10
2.4.1 Flow of powder.....	10
2.4.2 Dilatancy and the critical state.....	11
2.4.3 Jenike procedure.....	12
2.5 Johanson Hang-Up Indicizer.....	13
2.6 Advanced shear testers.....	16
2.6.1 Postec Flexible Wall Biaxial Tester.....	16
2.6.2 Braunschweig Biaxial Tester.....	18
2.6.3 Directional Shear Cell.....	18
<b>VISUALIZATION OF THE SHEAR REGION IN A DIRECT SHEAR TESTER</b>	<b>21</b>
3.1 Observations on shear regions.....	21
3.2 Shear region models.....	24
3.3 Theory of Neutron Depolarization.....	25
3.4 Instruments and experimental setup.....	29
3.4.1 Polyaxis neutron depolarization analyzer (PANDA).....	29
3.4.2 Small shear tester.....	29
3.4.3 Sample powder.....	30

---

3.5	Consolidation experiment.....	33
3.5.1	Procedure.....	33
3.5.2	Effect of increasing load.....	33
3.5.3	Effect of time.....	38
3.6	Shear region experiment.....	40
3.6.1	Procedure.....	40
3.6.2	Bulk density.....	41
3.6.3	Rotation of particles in the shear zone.....	42
3.6.4	Width of the shear zone.....	45
3.6.5	Shape of the shear region.....	46
3.7	Conclusion.....	48

**APPENDIX 51**

3A.1	Data increasing consolidation experiment.....	51
3A.2	Data time consolidation experiment.....	52
3A.3	Data shear plane experiment.....	53

**EVALUATION OF THE FLEXIBLE WALL BIAXIAL TESTER 59**

4.1	Introduction.....	59
4.2	BCR-limestone.....	60
4.3	The Flexible Wall Biaxial Tester.....	61
4.3.1	Setup.....	61
4.3.2	Definitions for the FWBT.....	63
4.3.3	Stress and strain control.....	64
4.3.4	Control program and preparation of an experiment.....	65
4.3.5	Filling procedure.....	66
4.3.6	Calibration of the membranes.....	66
4.3.7	Wall friction.....	68
4.4	Consolidation experiments.....	69
4.4.1	Introduction.....	69
4.4.2	Biaxial consolidation.....	70
4.4.3	<b>Uniaxial consolidation with two moving walls.....</b>	<b>73</b>
4.4.4	Uniaxial consolidation with one moving wall.....	77
4.4.5	Strain rate experiments.....	80
4.4.6	Shear planes after consolidation.....	80
4.5	Steady-state shear of BCR-limestone.....	82
4.6	Comparison of the Braunschweig Biaxial Tester and the Delft Flexible Wall Biaxial Tester.....	87

4.7	Flow function of BCR-limestone .....	90
4.7.1	Flexible Wall Biaxial Tester flow function .....	90
4.7.2	Correction of the flow function measured in the FWBT by Kraan (1996) .....	94
4.7.3	Influence of intermediate principal stress.....	94
4.7.4	Shear planes after determination of the unconfined yield strength.....	99
4.8	Conclusion.....	99
<b>APPENDIX</b>		<b>101</b>
4A.1	Flow function experiments.....	101
<b>ANISOTROPY IN POWDER FLOW BEHAVIOR</b>		<b>103</b>
5.1	Introduction .....	103
5.2	The occurrence of anisotropy .....	104
5.2.1	Definition of anisotropy.....	104
5.2.2	Anisotropy investigations with simple testers.....	105
5.2.3	Anisotropy in biaxial and triaxial testers.....	107
5.3	Microscopic view on anisotropy .....	111
5.4	Measurement of anisotropy with the Flexible Wall Biaxial Tester.....	112
5.4.1	Preparation of the sample .....	113
5.4.2	Rotation of the principal axes of strain.....	113
5.4.3	Six other deformations .....	117
5.4.4	Shear planes.....	122
5.5	Principal axes of stress and strain .....	123
5.6	Anisotropic flow function.....	124
5.7	Conclusion.....	127
<b>APPENDIX</b>		<b>129</b>
5A.1	Type I, II, IIIa, IIIb, IVa, IVb, Va and Vb experiments .....	129
5A.2	Anisotropic flow function.....	131
<b>MICROSCOPIC STRUCTURE IN POWDER FLOW</b>		<b>133</b>
6.1	Introduction .....	133
6.2	Structure in literature .....	134
6.3	Simulation software code by Walton and Braun.....	136
6.4	Consolidation simulations.....	138
6.5	Shear simulation .....	140
6.6	Suggestions for the structure tensor in powder.....	143
6.7	Conclusion.....	146
<b>CONCLUSION</b>		<b>149</b>

---

<b>LIST OF SYMBOLS</b>	<b>153</b>
<b>REFERENCES</b>	<b>157</b>
<b>SAMENVATTING</b>	<b>161</b>
<b>ACKNOWLEDGEMENT</b>	<b>163</b>
<b>CURRICULUM VITAE</b>	<b>165</b>

# Introduction

## 1.1 Powder handling

Handling of powders and granular materials is of great importance to industry. In the chemical industry alone, about one half of the products and at least three quarters of the raw materials are in the form of granular solids or powders (Nedderman 1992). On the other hand, powders and granular materials are very poorly understood compared to gases and liquids. The analogy of the Navier-Stokes equation for pneumatic transport of solids has still to be written down. This lack of knowledge has a large negative effect on the industry.

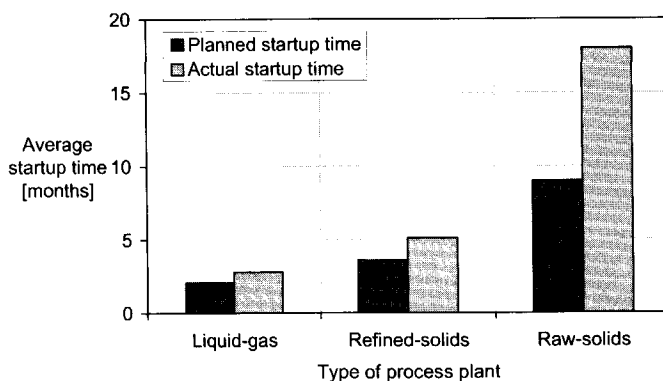


Figure 1.1: Planned versus actual startup times for plants using different types of feedstock (Merrow 1988).

The poor knowledge about powder handling results in, for example, startup problems of newly built plants. Merrow (1988) investigated 39 solids-processing plants on their startup times. The average scheduled startup time was slightly over three months, but the actual averaged startup time was nearly nine months. Thirteen of the 39 plants needed more than one year to start up. Figure 1.1 makes a distinction between raw and refined solids as a feedstock and the difference with plants processing gas or liquid is remarkable. By far the most common problems resulted from the tendency of solids to plug, stick, flow unevenly, and go where they should not (Merrow 1988).

The knowledge with which solids-processing plants are built nowadays is still mainly based on experience with other plants and on empirical tests. Therefore, research on the topic of powder behavior is essential.

## 1.2 Flow behavior of powders

A study of powders requires a macroscopic and a microscopic view. One is interested in the average behavior of the bulk, but the macroscopic properties of the bulk cannot be interpreted unless they can be related to the properties of the particles which make up the bulk. If the properties of molecules are related to those of a gas, it can be assumed that each molecule is the same. This simplification can, however, not be applied to the relation between particle and bulk properties. Every particle can have a different size and shape and there are an infinite number of ways to position and orientate all particles together in order to make up the bulk. However, experiments do show that the behavior of this bulk is reproducible to a certain extent and thus the relationship between the microscopic and macroscopic properties is not unique (Scarlett et al. 1998). Not much is known about how to relate particle properties and bulk properties.

The first major discovery on the bulk behavior of powder came from Reynolds in 1885 who found that the volume of densely packed granular material has to increase in order for the individual particles to start moving relative to each other. This phenomenon, called dilatancy, is very typical for powder. Hvorslev (1937) and Roscoe (1958) then defined the critical porosity, which is the minimum space between particles needed to move relative to each other without volume change of the sample. If the space between the particles is less than the critical porosity, the particle assembly has to dilate.

In 1961 Jenike used the concept of critical porosity to define a macroscopic function, the flow function, of a powder and designed the Jenike tester as a experimental tool to measure this function. In the flow function Jenike captures the "history" of a powder. This is an important concept because the flow properties of powder depend on the state it is in. This state is formed by previous processing. Jenike defined the history state of a powder in terms of its porosity.

The occurrence of anisotropy - the dependence of the flow of powder on the direction in which it is tested - clearly proves that porosity only describes part of the history of the powder. It is believed that structure is the missing link that can describe the state of the powder fully.

## 1.3 Aim and outline of this thesis

In this thesis, cohesive powder will be studied on its flow properties with the aim of enhancing the knowledge about powder flow behavior. The focus will be on proving that structure in powder is the missing parameter in the understanding of powder flow behavior.

When a powder flows, shear regions are formed. These shear regions are often seen as relatively small discontinuities between continuum blocks of powder. On a microscopic level, not much is known about these shear regions. In chapter 3 the Neutron Depolarization technique will be used to look into a shear region and



determine the bulk density, the rotation of the particles and the width and shape of the shear region. For this experiment a simple direct shear tester will be developed.

As an experimental tool for the measurement of the flow properties of powder, the Flexible Wall Biaxial Tester (Kraan, 1996) will be used. This is an advanced shear tester which can apply stresses or strains on a macroscopic powder sample in two directions. In chapter 4, the Flexible Wall Biaxial Tester will be evaluated and the flow function of BCR-limestone will be measured. In chapter 5 anisotropy in powder flow behavior will be investigated in order to prove that porosity is not the right parameter to describe the structure in powder. In conclusion, in chapter 6 a particle assembly will be simulated with the discrete element method to investigate the internal structure. In this chapter a number of tensors will be introduced that are thought to describe various aspects of the structure.



# Concepts of powder flow behavior

This chapter gives an introduction to powder flow behavior. The basic parameters that are used in powder flow theory are introduced together with the concepts Jenike (1961, 1964) defined. Next to this a number of powder flow testers is presented whose results will be used in later chapters.

## 2.1 Introduction

When one is first introduced to the term "powder flow", one could associate it to the flow of liquid or gas. This is a wrong conception. Jenike (1964) lists the differences between liquid and powder. Powder can transfer shearing stresses under static conditions and the static angle of friction is not equal to zero as with liquids. Many powders possess a cohesive strength after they have been consolidated and can form a stable arch. Liquid cannot do that. The shearing stresses which occur in a slowly deforming bulk solid can usually be considered independent of the rate of shear and dependent on the mean pressure acting within the solid. In a liquid, the situation is reversed. Thus, powder and granular materials have specific properties that have to be understood in order to engineer powder handling equipment or, more sophisticated, to engineer powder itself.

Early contributions to the investigation of the flow of powders and granular materials came from Reynolds (1885), Janssen (1895), Hvorslev (1937) and Roscoe (1958). However, Jenike is regarded as the first to use the concepts of the early powder flow theory as an engineer. He developed a procedure for the design of a silo based on the flow characteristics of powder (Jenike 1961, 1964). The parameters used are stress, strain and porosity and these are introduced in this chapter. Next to this, an overview of the existing powder flow theory is given and some existing powder flow testers are presented with some typical features.

## 2.2 Stress, strain and structure

The stress and strain tensor are known parameters in powder technology. Next to these tensors, bulk density or porosity is a scalar parameter that represents the state or, more correct, the structure in a powder. Structure will be treated more extensively in chapter 6.

### 2.2.1 The state of stress

The continuum representation of the equilibrium stresses on a cubical sample is given on the left side in figure 2.1.

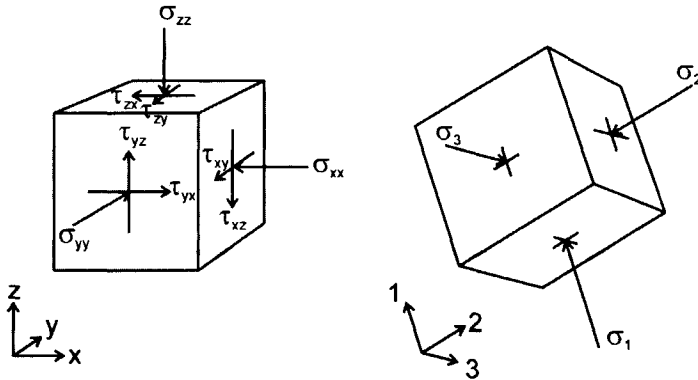


Figure 2.1: Cubic sample under a certain state of stress (left) and the principal axes and principal stresses for the same state of stress (right).

The nine stresses acting on the specimen are arranged in the stress tensor.

$$\underline{\underline{T}} = \begin{pmatrix} \sigma_{xx} & \tau_{xy} & \tau_{xz} \\ \tau_{yx} & \sigma_{yy} & \tau_{yz} \\ \tau_{zx} & \tau_{zy} & \sigma_{zz} \end{pmatrix} \quad (2.1)$$

The normal stresses are often presented with a single index:  $\sigma_x$ ,  $\sigma_y$  and  $\sigma_z$ . If the body is in rest the stress tensor is symmetric and thus has only six independent components. Compressive stresses are taken positive, as is usual in powder technology.

The stress tensor can be characterized by three invariant scalars: the principal stresses. If the principal stresses line up with the coordinate axes, these are called the **principal axes of stress**. For these principal axes all shear components of the stress tensor have vanished as shown on the right side in figure 2.1. The stress tensor is then written as:

$$\underline{\underline{T}} = \begin{pmatrix} \sigma_1 & 0 & 0 \\ 0 & \sigma_2 & 0 \\ 0 & 0 & \sigma_3 \end{pmatrix} \quad (2.2)$$

It presents the same state of stress as in the left side of figure 2.1, only the orientation of the coordinate axes has changed. The largest stress of this unique set of principal stresses is called the major principal stress ( $\sigma_1$ ), the smallest the minor principal stress ( $\sigma_3$ ) and the one in between the intermediate principal stress ( $\sigma_2$ ). The principal

stresses can be obtained from the so called characteristic equation (Macosko, 1994 and others):

$$\sigma^3 - I\sigma^2 + II\sigma - III = 0 \quad (2.3)$$

I, II and III are invariants which are independent on the orientation of the axes.

$$\begin{aligned} I &= \sigma_x + \sigma_y + \sigma_z = \\ &= \sigma_1 + \sigma_2 + \sigma_3 \end{aligned} \quad (2.4)$$

$$\begin{aligned} II &= \sigma_x \sigma_y + \sigma_x \sigma_z + \sigma_y \sigma_z - \tau_{xy} \tau_{yx} - \tau_{xz} \tau_{zx} - \tau_{yz} \tau_{zy} = \\ &= \sigma_1 \sigma_2 + \sigma_1 \sigma_3 + \sigma_2 \sigma_3 \end{aligned} \quad (2.5)$$

$$\begin{aligned} III &= \sigma_x \sigma_y \sigma_z + \tau_{xy} \tau_{yz} \tau_{zx} + \tau_{xz} \tau_{zy} \tau_{yx} + \\ &\quad - \sigma_x \tau_{yz} \tau_{zy} - \sigma_y \tau_{xz} \tau_{zx} - \sigma_z \tau_{xy} \tau_{yx} = \\ &= \sigma_1 \sigma_2 \sigma_3 \end{aligned} \quad (2.6)$$

The principal stresses are the eigenvalues of the stress tensor and form the roots of the characteristic equation. The directions of the principal stresses are given by the eigenvectors. By using 2.4, 2.5 and 2.6 many other invariants can be formed, as for example the mean stress:

$$\sigma_m = \frac{\sigma_x + \sigma_y + \sigma_z}{3} \quad (2.7)$$

Feise (1996) defined the second invariant being some measure of the root mean square average of the three largest shear stresses:

$$II = \sigma_r = \sqrt{(\sigma_1 - \sigma_2)^2 + (\sigma_2 - \sigma_3)^2 + (\sigma_1 - \sigma_3)^2} \quad (2.8)$$

This definition of the deviatoric stress will be used in this thesis.

Very often the state of stress is represented by two principal stresses, the major and minor principal stress, in a Mohr diagram (figure 2.2). The intermediate stress is thereby neglected, because the largest and smallest principal stress will dictate the formation of a shear plane and therefore the flow of the powder.

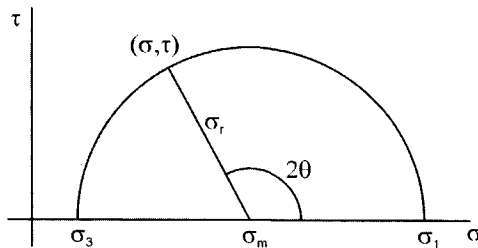


Figure 2.2: Mohr circle for a certain state of stress.

The normal and shear stress on any plane perpendicular to the plane formed by the major ( $\sigma_1$ ) and minor ( $\sigma_3$ ) principal stresses are given by the circle,  $\theta$  being the angle of the plane to the direction of the major principal stress. The normal and shear stresses on each plane with an angle  $\theta$  to the direction of the major principal stress, can be calculated with the following equations:

$$\sigma = \sigma_3 + \frac{\sigma_1 - \sigma_3}{2} (1 + \cos(2\theta)) \quad (2.9)$$

$$\tau = \frac{\sigma_1 - \sigma_3}{2} \sin(2\theta) \quad (2.10)$$

The mean stress, which forms the center of the Mohr circle, is now defined as:

$$\sigma_m = \frac{\sigma_1 + \sigma_3}{2} \quad (2.11)$$

and the deviatoric stress as:

$$\sigma_r = \frac{\sigma_1 - \sigma_3}{2} \quad (2.12)$$

The plane of failure in a powder lies on the left side of the Mohr circle because there the greatest ratio of shear stress to normal stress is found. The exact position can, however, not be determined mathematically.

### 2.2.2 The state of strain

The state of stress acting on a cubical sample can cause deformation that will change the volume and shape of the sample. The deformation of the sample is given by its state of strain. Its presentation by the strain tensor is analogue to the stress tensor.

$$\underline{\underline{E}} = \begin{pmatrix} \epsilon_{xx} & \gamma_{xy} & \gamma_{xz} \\ \gamma_{yx} & \epsilon_{yy} & \gamma_{yz} \\ \gamma_{zx} & \gamma_{zy} & \epsilon_{zz} \end{pmatrix} \quad (2.13)$$

Strain can be defined in different ways, but in this thesis the Cauchy definition is used. In figure 2.3 two types of deformation have been defined.

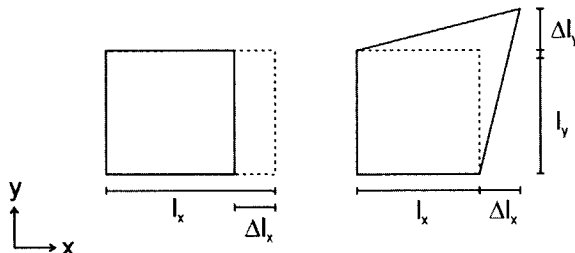


Figure 2.3: Cubic sample under a certain state of strain.

The definition for the normal strain is:

$$\epsilon_x = -\frac{\Delta l_x}{l_x} \quad (2.14)$$

and for the shear strain:

$$\gamma_{xy} = -\frac{1}{2} \left( \frac{\Delta l_x}{l_y} + \frac{\Delta l_y}{l_x} \right) \quad (2.15)$$

These definitions can easily be changed for three dimensional strains. Strain is defined positive for contraction and negative for extension as is common in powder mechanics. In plastically deforming samples, one often uses the strain rate tensor instead of the strain tensor. The strain rate and the shear strain rate are defined in equations 2.16 and 2.17.

$$\dot{\epsilon}_x = \frac{d\epsilon_x}{dt} \quad (2.16)$$

$$\dot{\gamma}_{xy} = \frac{d\gamma_{xy}}{dt} \quad (2.17)$$

### 2.2.3 The state of structure

The third parameter in powder flow theory is the porosity, which is the volume fraction of free space between the particles. The porosity is related to the bulk density in the following way if the voids are filled with air:

$$\epsilon = 1 - \frac{\rho_{\text{bulk}}}{\rho_{\text{material}}} \quad (2.18)$$

The bulk density is the total mass of the sample divided by its volume. It will be shown in this thesis that the porosity fails as a parameter to describe some specific powder properties. The porosity is regarded as not more than a shadow of the real parameter describing the structural state of the powder (Scarlett et al. 1998). The porosity has a major advantage being the ease of measurement.

## 2.3 Soil mechanics

The field of powder technology has many overlaps with the field of soil mechanics. The Jenike Tester, for example, has been developed according to the shear box known in soil mechanics. The cylindrical tester, in soil mechanics known as triaxial tester, has been used without much adaptations for the characterization of flow behavior of powder (Gerritsen, 1985 among others). Also many elements of the theory are taken from earlier developments in soil mechanics (Roscoe et al. 1958, Roscoe 1970). In general the research in soil mechanics can be said to be much further developed than the field of powder technology. It is, therefore, very important to keep the links

between the two fields established, while keeping in mind the important differences. Kruyt (1994) points out these differences:

- Flow: in powder mechanics one is interested in flow of the material, while in soil mechanics the emphasis is on what happens before failure of the material.
- Stress level: usually the stress level in powders is lower (about a factor ten) than that encountered in geotechnical applications.
- Deformation level: powders are often subjected to larger deformations, usually in a silo.
- Strain rate: the rate with which deformations are applied to powder are normally much faster.
- Transient phenomena: experiments show that during discharge of granular materials from a silo significant deviations from stationary conditions occur in the stress field at the wall. These transient phenomena are more pronounced than in soil mechanics.
- Pore pressure: in soil mechanics the liquid content can play an important role by generating a pore pressure. The influence of the gas pore pressure of granular materials in silos is very small and is usually neglected.

## 2.4 Powder flow theory

The following paragraphs will give an overview of the existing powder flow theory. A large part of it, consists of the work of Jenike (1961, 1964) who engineered the existing knowledge of powder flow into the flow function.

### 2.4.1 Flow of powder

The concept of powder flow is best defined by introducing the Jenike Tester (figure 2.4). This basic tester consists of two parts and a separate lid that form a box which contains the sample powder. A powder is brought to "flow" by moving the top half of the tester relative to the bottom part causing a shear plane in the powder. This action results in a steady-state shear force ( $\tau$ ) that depends on the normal weight ( $\sigma$ ) that is put on the powder via the lid.

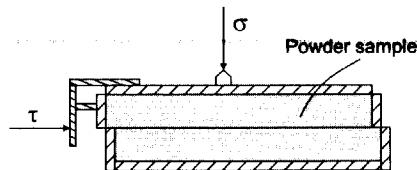


Figure 2.4: Jenike Tester.

The flow behavior of powder depends on its history and therefore the actions that define this history are part of the investigation of powder flow behavior. In section 2.4.3 it is shown how Jenike (1961, 1964) captured this history in the so called flow function that characterizes the flow behavior of a powder.



### 2.4.2 Dilatancy and the critical state

A very peculiar property of powder or granular matter is dilatancy. Reynolds (1885) observed that a compacted material expands on initiation of shear. This means that under a compressive stress the volume of a powder sample increases. The increase of volume does not take place in all cases, only when the particles in the powder are in such a compact state relative to the exerted compressive force that before they can move, space has to be created (figure 2.5). This state is called overconsolidated.

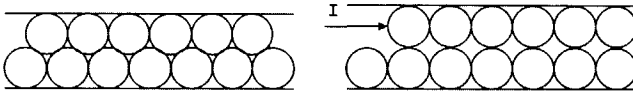


Figure 2.5: Dilatancy due to an overconsolidated state in the sample.

In an underconsolidated state the powder volume decreases when shear deformation is applied in for example the Jenike Tester. In between the underconsolidated state and the overconsolidated state a critical consolidated state exists. In this state, the volume of the sample does not change when the shear experiment is performed. These are macroscopic observations, which are thought to be explained on a microscopic scale by means of the space between the particles in the shear zone: the porosity. It is believed that when the shear stress and the volume of the sample in the Jenike Tester become constant the porosity in the shear zone also reaches a constant value: the critical porosity. This critical porosity depends on the normal stress ( $\sigma$ ). In the overconsolidated and underconsolidated state the porosity is respectively lower and higher than the critical one for the applied normal load and it will change such that the critical porosity is reached.

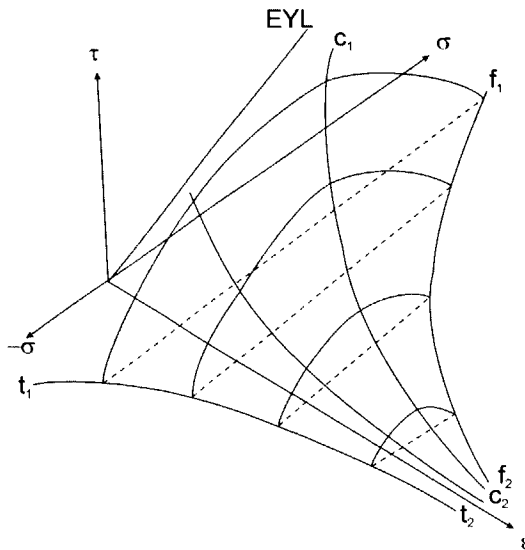


Figure 2.6: Hvorslev diagram:  $t_1t_2$  tensile strength line;  $c_1c_2$  critical state line;  $f_1f_2$  normal consolidation line; EYL effective yield locus.

A three dimensional state diagram (figure 2.6) that incorporates the normal stress ( $\sigma$ ), the shear stress ( $\tau$ ) and the porosity ( $\epsilon$ ) of powder was first defined by Hvorslev (1937) and later completed by Roscoe et al. (1958). Three characteristic lines make up the consolidation (Roscoe) surface and the flow (Hvorslev) surface in this diagram. The normal consolidation line  $f_1f_2$  represents the decrease in the porosity with increasing normal stress in the absence of shear. The relation between the tensile strength and the porosity in absence of shear is given by the line  $t_1t_2$ . The third characteristic line is the critical state line  $e_1e_2$  that determines the critical porosity at steady-state shear. The critical state line is the intersection between the consolidation surface and flow surface.

### 2.4.3 Jenike procedure

The procedure of Jenike (1961 and 1964) is specifically for the design of silos and it combines silo properties with powder flow properties: the silo defines the conditions the powder will be submitted to and depending on its flow properties the powder will or will not flow. This paragraph focuses on the powder part of Jenike's procedure.

For the measurement of powder flow properties Jenike used the concept of similar (rectangular) shear testers that were known in soil mechanics research. The modified version, the Jenike Tester, is still accepted as the standard powder flow tester (figure 2.4). Detailed descriptions of the tester are numerous in literature (Jenike 1961 and 1964, Schwedes 1971, EFCE Working Party on the Mechanics of Particulate Solids 1989, Akers 1992, Verlinden 2000, among others).

Jenike's procedure for the measurement of powder flow properties consists of two steps. The first step, the preshear step, applies the history to the powder and the second step measures the resulting strength. The first step is such that the powder is in an overconsolidated state during the second step. These two steps simulate the situation in a silo, in which a powder undergoes a certain history of shear and consolidation in the top of the silo that gives it a strength when it reaches the bottom part of the silo. This strength has to be overcome in order for the powder sample to break and flow out of the silo. The critical situation in the bottom part of the silo occurs when an arch forms that blocks the silo. The stress state in the arch is special because the minor principal stress that works on the free side at the bottom of the arch is zero. The stress that is needed to break the powder sample in the case that the minor principal stress for an element of powder in the bottom of the arch is zero, is called the unconfined yield strength  $f_c$  (figure 2.7).

The stress state of the unconfined yield strength is a limit case that cannot be measured directly in the Jenike Tester. However, the unconfined yield strength can be extrapolated from measurements in which the major principal stress ranges between the unconfined yield strength and the value of the major principal stress during the preshear step in the procedure (figure 2.7). The latter value is a limit, because a higher value would bring the powder in an underconsolidated state which means that the sample will consolidate instead of dilate. The combined measurements for one type of history make up a yield locus (figure 2.7). Yield loci are often thought of as straight lines, but for cohesive powders they are curved. The angle of the yield locus approximated by a straight line is called the angle of internal friction.

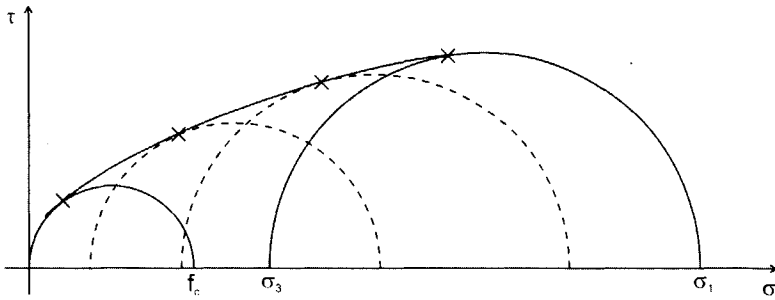


Figure 2.7: Yield locus characterized at the endpoint by a Mohr circle that defines steady-state shear with  $\sigma_1$  and  $\sigma_3$ . The unconfined yield strength ( $f_c$ ) for this yield locus is determined from the Mohr circle through the origin touching the yield locus.

The history of the powder that is applied in the first step is defined by the major principal preshear stress  $\sigma_{1p}$  (the suffix "p" is often dropped) in that step. This stress is determined by fitting a Mohr circle through the measured point  $(\sigma, \tau)$  that also touches the yield locus. The unconfined yield locus is determined by fitting a Mohr circle through the origin, because the minor principal stress equals zero, and touching the yield locus.

The procedure is repeated for different histories in the preshear step, which means that the normal load is varied and the powder is brought to steady-state preshear. This leads to multiple yield loci and for each one the unconfined yield strength is determined and the pairs of  $\sigma_{1p}$  and  $f_c$  are plotted in a figure to make up the flow function of the powder.

Yield loci are in fact projections of the yield surface in the Hvorslev diagram (figure 2.6) on the  $\sigma, \tau$  plane. Each endpoint of a yield locus is a point on the critical state line, which defines the critical porosity for the steady-state flow characterized by  $\sigma$  and  $\tau$  of a powder. In theory, the projection of the critical state line onto the  $\sigma$ - $\tau$  plane is called the effective yield locus (EYL). This line goes through the origin and touches all Mohr circles that define the endpoints of yield loci. The angle of the effective yield locus is called the effective angle of internal friction. In practice, the line touching the Mohr circles deviates from the projection of the critical state line (Nedderman, 1992).

Jenike compares the flow function with a characteristic line that describes the stress situation in a silo. The intersection between the lines is the critical point that defines whether a powder will flow in that silo.

## 2.5 Johanson Hang-Up Indicizer

The Jenike Tester has gotten many successors. Some of these, like the rotational testers, have been developed to overcome the inconvenience of the limited shear deformation in the Jenike Tester. Some researchers have tried to simplify Jenike's experimental procedure (uniaxial testers) or developed new principles (e.g. Warren Spring Bradford Cohesion Tester, powder rheometers, Hosokawa Tester, among

others) and new procedures (e.g. Peschl Tester) to measure flow. One of these testers is the Johanson Indicizer. In this paragraph, the calculation procedure of this tester will be clarified (Orange project, 2000).

In 1992 Johanson (1992a) published an article in which he compared the Jenike Shear Tester with the Johanson Indicizer. This article gave rise to a lively discussion (Carson 1992, Schwedes et al. 1992, Enstad et al. 1992, Johanson 1992b, Bell et al. 1994, Marjanovic et al. 1995). Although, it was clear how the Johanson Indicizer worked, it was unclear how exactly the calculation procedure of the unconfined yield strength was performed (Schwedes 1999). Kraan (1996) suggested that in the software program of the tester an internal angle of friction for the yield locus of 25 degrees has been assumed.

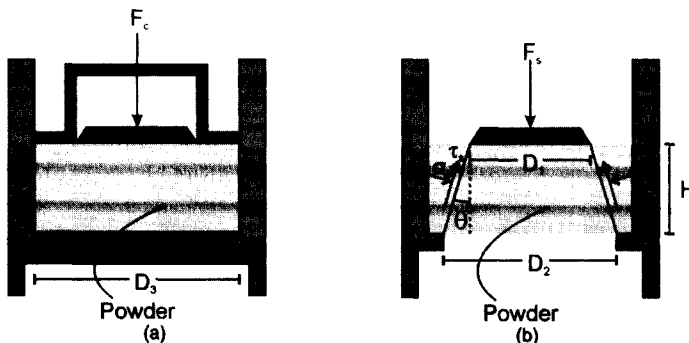


Figure 2.8: Schematic view of the Johanson Indicizer: the consolidation stage (a) and the determination of the unconfined yield strength (b).  $D_1 = 41.48$  mm;  $D_2 = 46.63$  mm;  $D_3 = 52.55$ ;  $H \approx 23$  mm.

The Johanson Indicizer is designed to duplicate the initial deposition of a bulk solid in a bin. This initial deposition is essentially without shear deformation according to Johanson. In figure 2.8 the configuration of the tester is shown for the consolidation stage (a) and for the measurement of the unconfined yield strength (b). The weighted sample is consolidated in a cylindrical mold using a retractable bottom and a two-piece piston on top that measures the consolidation pressure directly on the inner piston while the inner and outer pistons move together. The outer piston receives all the drag effects on the cylinder walls and thereby eliminates any drag effects in the inner piston when the compaction pressure is measured (Johanson, 1992a). It is claimed that the sample is consolidated uniformly to a known major principal stress level (figure 2.8a).

In the second stage of the procedure the consolidation load is removed. The bottom piston retracts and the sample is unconfined. The upper outer piston is also retracted and the inner piston is moved downwards. The sample will fail and the unconfined yield strength is directly measured (figure 2.8b).

It should be remarked that no preshear takes place in the sample as defined in the Jenike procedure. Johanson (1994) argues that preshear to a steady-state flow condition is unnecessary. The flow function measurements with and without preshear by Harder (1986) and Schwedes et al. (1990) show that this argument is incorrect.

Preshear is thought to have a consolidating effect on the powder sample and for this reason the measurement of the unconfined yield strength in the Johanson Hang-Up Indicizer will be lower from that measured with the Jenike Tester. This is confirmed by Marjanovic (1995).

The pressure in the consolidation stage is equal to the force on the inner piston divided by the area of the inner piston (figure 2.8):

$$\sigma_c = \frac{F_c}{\frac{\pi}{4} D_1^2} \quad (2.19)$$

The consolidation pressure is applied for a preset time, during which the control software continually adjusts the top piston position to maintain the required pressure. This consolidation pressure is chosen according to:

$$\sigma_c = \alpha \cdot \rho_{\text{bulk}} g \quad (2.20)$$

in which the constant  $\alpha$  equals 1.5 m. The mass of the sample is measured before the test is performed. The choice for this criterion is disputed by Bell et al. (1994). The height of the sample after the consolidation is recorded.

The unconfined yield strength in the second stage is calculated by writing down the force balance on the volume of powder that is pressed out of the tester. The shear plane is thought to form between the edge of the top piston and the ridge in the bottom of the tester (see figure 2.8b). The force balance is as follows:

$$F_s + \rho_{\text{bulk}} gV = \tau_s S \cos(\theta) - \sigma_s S \sin(\theta) \quad (2.21)$$

$F_s$  is the force measured on the top piston when the powder fails and  $S$  the surface of the shear plane. The volume of the powder being pressed out of the tester (truncated cone) is:

$$V = \frac{1}{12} \pi H (D_1^2 + D_1 D_2 + D_2^2) \quad (2.22)$$

The surface area of the shear zone equals:

$$S = \frac{1}{4} \pi \frac{D_2^2 - D_1^2}{\sin(\theta)} \quad (2.23)$$

The angle  $\theta$  that the shear plane makes is defined by the dimensions of the tester:

$$\tan(\theta) = \frac{D_2 - D_1}{2H} \quad (2.24)$$

To find expressions for the normal ( $\sigma_s$ ) and shear stress ( $\tau_s$ ) on the shear plane a yield locus is considered (figure 2.9). This yield locus is assumed to be a straight line with an angle of internal friction  $\phi$ . This angle actually varies for different yield loci but it assumed here to be constant and to be equal to the effective angle of internal friction.

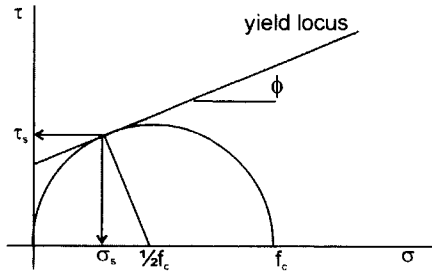


Figure 2.9: Calculation of the unconfined yield strength in the procedure of the Johanson Indicizer.

The following relations for  $\sigma_s$  and  $\tau_s$  can be conducted from figure 2.9:

$$\sigma_s = \frac{1}{2} f_c (1 - \sin(\phi)) \quad (2.25)$$

$$\tau_s = \frac{1}{2} f_c \cos(\phi) \quad (2.26)$$

Substitution of  $\sigma_s$ ,  $\tau_s$  and  $\tan(\theta)$  in equation 2.21 gives:

$$f_c = \frac{1}{3} \frac{\gamma \pi H (D_1^2 + D_1 D_2 + D_2^2) + 12 F_s}{\pi H \cos(\phi) (D_1 + D_2)} \quad (2.27)$$

This is how the unconfined yield strength is calculated in the Johanson Indicizer. The tester has two modes: a normal mode and a scientific mode. In the latter the angle of internal friction can be given in; in the normal mode an angle  $\phi = 24.6^\circ$  is assumed. By using this angle and by realizing that the first term in the counter of equation (2.27) is much smaller than the second term equation 2.27 reduces to (Johanson, 1993):

$$f_c = 2.2 \cdot \tau_s \quad (2.28)$$

In the control program of the Johanson Indicizer it is assumed that the inaccuracy of the internal angle of friction does not add up greatly to the overall inaccuracy of the outcome of any other powder flow tester.

## 2.6 Advanced shear testers

An overview of the most common powder shear testers known at this moment is given by Schwedes (1999). More recently, Verlinden (2000) compared a variety of powder flow testers for a number of powders.

Next to these testers a different group of testers has been developed with the aim to fundamentally investigate the flow behavior of powder. These testers have more possibilities in the stress and strain paths that they apply to the sample. Most of these testers are true biaxial testers and they will be introduced in this paragraph.

### 2.6.1 Postec Flexible Wall Biaxial Tester

In a true biaxial tester control of two directions of a powder sample is possible. The main idea is that these directions match the principal directions of stress or strain.

Therefore, effort is put in applying only normal components of stress or strain and no shear components. For stress this is especially difficult because frictionless walls do not exist. The solution to this problem is the use of prestretched membranes that deform homogeneously with the sample.

The Postec Biaxial Tester (PBT) uses such membranes in the form of balloons that make up the walls of the rectangular shaped sample holder (figure 2.10). These walls are flexible and are not backed up by a rigid wall, but the walls can move inwards and outwards by motors. The sample volume is covered by membranes in the z direction as well, but these are backed up by rigid plates and these walls cannot move. The minimum size of the sample volume is  $80 \times 80 \times 100 \text{ mm}^3$  and the maximum size is  $120 \times 120 \times 100 \text{ mm}^3$ . The PBT has been developed by the Telemark Institute of Technology in Norway by Maltby (1993) and is an automated version of an earlier biaxial tester (Arthur et al., 1985). The main goal of the tester was to measure the flow function directly without the extrapolation that is needed in the Jenike Tester. This is done by performing a stress controlled experiment (figure 4.43).

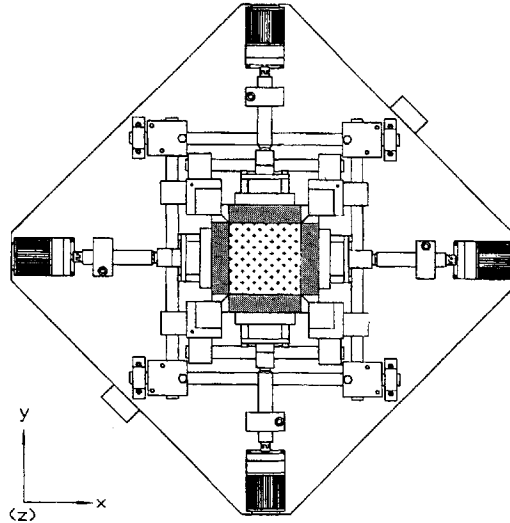


Figure 2.10: Postec Biaxial Tester (PBT). The gray areas indicate the membranes; the dotted area is the sample (Maltby 1993).

The balloons that form the walls of the sample holder can be pressurized and in this way a stress can be applied on the powder sample. However, the balloon wall will deform because of the change in stress and this has to be corrected by moving the whole wall inwards or outwards. The detection of the deformation of the balloon walls is done by make and break contacts. This make and break mechanism proved to be the weakest link of this tester because it did not seem accurate enough for the detection of dilation (Maltby, 1993). However, the application of consolidation gave very reproducible results.

### 2.6.2 Braunschweig Biaxial Tester

The true biaxial tester of the Institut für Mechanische Verfahrenstechnik of the Technical University of Braunschweig differs from the Postec Biaxial Tester in that it has rigid instead of flexible walls. Again prestretched membranes are used to reduce the friction between the sample and the walls. Between the membranes and the rigid walls a lubricant is used to reduce that friction as well. The top and bottom of the sample are covered by rigid plates and membranes too. However, no strain can be applied in the z direction. Since the boundaries of the sample are always parallel to the x, y and z axes, the applied strains are the principal strains.

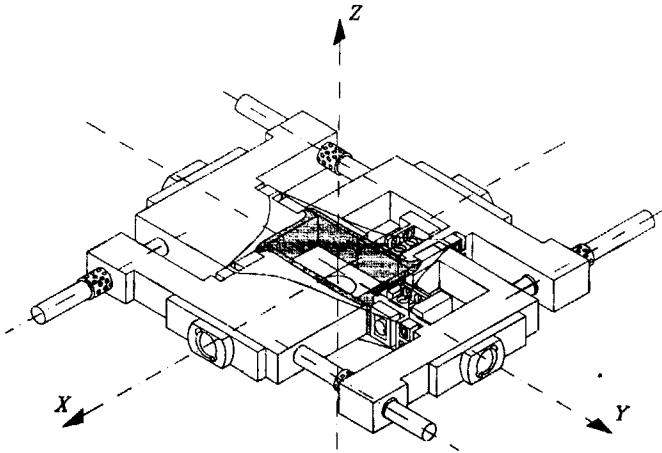


Figure 2.11: Braunschweig Biaxial Tester (BBT) (Nowak 1993).

In the Braunschweig Biaxial Tester (BBT) the square shaped sample holder has a maximum size of  $130 \times 130 \times 35 \text{ mm}^3$  and minimum size of  $60 \times 60 \times 35 \text{ mm}^3$ . The center of the sample holder cannot change its position. The tester is in principle a strain controlled device, but a stress controlled operation can be performed in a feedback loop. The stresses on two side walls (one in x direction and one in y direction) and on top of the sample are recorded. The BBT has been developed by Harder (1986) and underwent changes by Nowak (1993). The tester is used extensively by Feise (1996), who used it for the modeling of powder, and Zetzener (1998, 2001), who investigates relaxation and creep of powder.

### 2.6.3 Directional Shear Cell

The directional shear cell (DSC) has mainly been used for the investigation of sand samples at the University College London (Arthur et al. 1977, Arthur et al. 1981). It is, however, a unique tester that is stress controlled and can apply not only normal stresses but also shear stresses on four side walls (figure 2.12). The top and bottom of the sample are constrained by two transparent plates. The initial sample size is  $100 \times 100 \times 100 \text{ mm}^3$  and up to 15 % strain can be applied. The alignment of the normal pressure bags and the shear sheets is done after each stress path. Strains are measured by analyzing radiographs of embedded metal particles.



In the DSC it is possible to apply rotations of the principal axes of stress and measure the resulting principal axes of strain. Arthur carried out an extensive program on inherent and induced anisotropy of sand with the DSC (Wong et al. 1985).

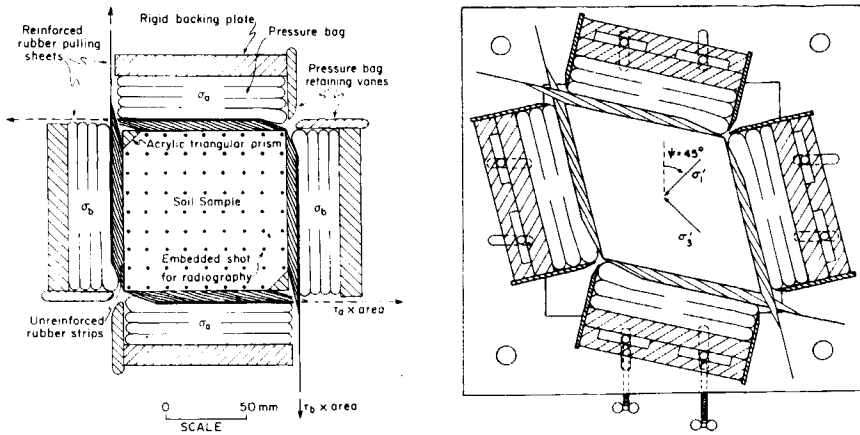


Figure 2.12: Directional Shear Cell (Arthur et al., 1977).



## Visualization of the shear region in a direct shear tester

Testers for the measurement of powder flow behavior apply one or more shear regions in a powder sample. In literature not much is known about the size of such a shear region. An often mentioned rule of thumb for a shear zone is that the thickness is approximately 10 times the particle size. For standard BCR-limestone with an average diameter of  $4.2\ \mu\text{m}$  that would mean a thickness of  $0.04\ \text{mm}$ . When the shear zone in the Jenike tester is observed after a shear experiment it is difficult to come to the same conclusion.

In this chapter the shear region that occurs in a small especially built direct shear tester has been investigated with the Neutron Depolarization (ND) technique. This gives information about the local bulk density, the width and shape of the shear region. Also the rotation of magnetic particles in the shear region will be monitored while consolidation loads up to  $23\ \text{kPa}$  are applied. The effect of consolidation on the powder sample is investigated as well. This is done in two manners: consolidation due to time with a constant load and consolidation with an increasing load.

### 3.1 Observations on shear regions

In powder technology direct shear testers are often used to characterize the flow behavior of a powder. These testers are designed to create a shear region in the powder. The normal and shear stress on this plane are measured, assuming that a flat horizontal shear plane occurs. In figure 3.1 the shear plane in a Jenike tester is shown for a cohesive powder. This shear plane is not flat and is quite irregular.



Figure 3.1: Shear plane in the Jenike Tester.

Schwedes (1971) remarked that the shear plane of a cohesive powder in the Jenike Tester has a toothed structure. According to Schwedes, this indicates that the actual shear takes place in planes or zones on the teeth with a certain angle to the horizontal. He observed that the shear zones mainly go down - that means the teeth are positioned below the applied shear horizontal. Schwedes has proven that it is not caused by less shear resistance because of a lower bulk density in the bottom of the tester which is due to the filling procedure. Schwedes tried to measure the orientation of the principal stresses in the shear region but found a wide range in these orientations which indicated that there is no preferred angle of the planes of the teeth.

One now accepts an idealized lens shaped shearing region (Schwedes, 1971, 1999). The size of this region has been investigated a number of times. Scarlett and Todd (1968) used three ways to determine the size of the shear region of sand samples ( $d_p = 0.18 - 1.2$  mm) in a split ring annular shear cell. Firstly, by means of a band of dyed sand in which the disturbance is measured manually. Secondly by a gamma attenuation technique and last by measurement of the vertical expansion of the bed. They concluded that flow will occur in a region of definite depth which is a function of the properties of the material. The depth of shear tends to increase as the size of the particles increases or the normal load increases.

In soil mechanics the width of the shear region is investigated more intensively. From table 3.1 it can be seen that the investigated materials were mostly incohesive and they had large particle sizes with respect to powder (micrometer range). All of the measurement techniques used, measure in one way or another the density change at the position of the shear region. The rotation of the particles cannot be measured.

Table 3.1: Overview of shear zone width given in literature

	Sample	Method	Size shear zone [particle sizes]
Scarlett, Todd (1968)	sand (0.18-1.2 mm)	manually gamma radiation vertical expansion	4 - 10
Roscoe (1970)	L. Buzzard sand (0.6-0.85 mm)	radiography	10
Scarpelli, Wood (1982)	L. Buzzard sand (0.4 mm)	X-ray	8 - 10
Mühlhaus, Vardoulakis (1987)	sand (0.2-0.3 mm)	X-ray	8 - 10
Bardet, Proubet (1991)	discs	numerical simulation	15 - 18
Oda, Kazama, Konishi (1998)	Toyoura sand (0.2 mm) Ticino sand (0.5 mm)	microscope	7 - 8
Mandl, Josselin de Jong, Maltha (1977)	glass spheres ( $\pm 1$ mm) pyrex splinters ( $\pm 1$ mm) sand ( $\pm 1$ mm) ground walnut shells ( $\pm 1$ mm)	microscope	8 - 20

In the experiments of Mühlhaus and Vardoulakis (1987) the shear region existed of multiple shear zones which were about 10 particle diameters wide. The regions between the shear zones were relatively stagnant. It is unknown whether this also occurs in cohesive powder. In this thesis, the term 'shear region' is used without the microscopic behavior inside this region being defined.

Schwedes (1971) saw in his experiments with limestone ( $d_p = 3 \mu\text{m}$ ) that a critically consolidated sample formed a wider shear region than an overconsolidated sample.

He concluded therefore that the width of the region depends on the consolidation state of the material. This hypothesis has been validated by measuring the displacement of 1.4 mm lead balls in the sample with X-ray photography (figure 3.2).

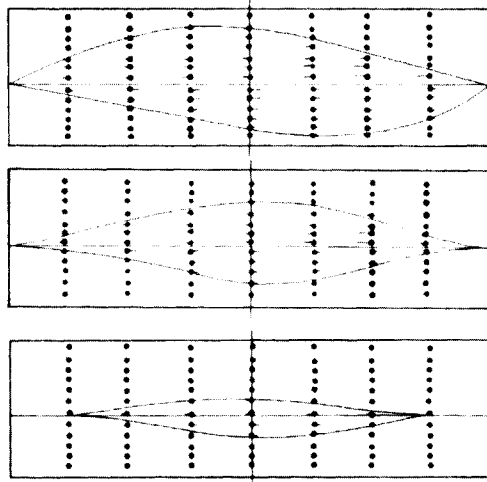


Figure 3.2: Shear region in the Jenike Tester by means of the displacement of 1.4 mm lead balls in an underconsolidated (top) critically consolidated (middle) and overconsolidated (bottom) limestone sample (figure 53 from Schwedes, 1971).

This experiment proved that the shear region is lens shaped and that the width of the region depends on the consolidation state of the sample. No actual size is mentioned by Schwedes but from the figures 3.2 it can be seen that the region forms a substantial part of the tester.

The explanation for the dependence on the consolidation was presented as the principle of least resistance. Shear will occur at the position where the resistance is minimal. In an underconsolidated sample the region will increase because the porosity in the shear region will decrease. An overconsolidated sample dilates and the dilated region has less resistance than the regions with a lower porosity around it: the shear region will not grow.

The shape and the size of the growing shear region depends on the configuration of the tester which is an explanation why different shear testers give different results. If for example a shear tester has a limited height the growing shear region in an underconsolidated sample is limited as well. This can be seen in Schwedes experiments (figure 3.2 top): the sample is in steady-state shear and the shear region has almost reached the top and bottom of the tester.

As shown above, no single discrete shear zone exists in the powder in a direct shear tester. As Scarlett (1968) states: one cannot draw one unique line through the failing contacts between the particles. The idea of failing contacts is wrong in case one only thinks of sliding contacts. A very large part of the failing contact is rolling, which happens at much lower friction values. The question is which portion of the failing

contacts is of the sliding type and which portion is of the rolling type. The answer to this question depends on the material, the position and the orientation of the particles relatively to each other. The history of the powder determines the position and orientation of the particles as Schwedes (1971) has shown by proving that the size of the shear region depends on the state of consolidation. The idea of Scarlett (1968) leads to a shear region in which all particles rotate and which does not exist of multiple small shear zones separated by stagnant zones.

The goal of this chapter is to measure the width of the shear region and the rotation of the particles in the shear region for a cohesive powder. Therefore, the shear region that occurs in a simple direct shear tester has been investigated with Neutron Depolarization (ND). With this technique the movement of magnetic particles in the shear region is monitored by analyzing the polarization of the neutron beam after transmission through the powder sample. The scan gives information about the bulk density, the rotation of the magnetic particles and the size of the magnetic domains. From this information the size of the shear region is extracted.

### 3.2 Shear region models

Observations and measurements on shear regions have led to a number of models. A short description of these will be given in this section. A shear region can be thought to be more or less homogeneous or can be thought to exist of one or more shear zones.

The simplest representation of a shear zone is the Coulomb model (figure 3.3 top). In this case, the shear zone is a perfectly horizontal plane along which two parts of the powder move along each other. This movement only occurs if the applied shear stress reaches a certain critical value. A model that allows the shear to be more homogeneous over the whole sample (figure 3.3 bottom) is known as the "toppling bookrow" model.

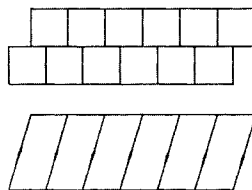


Figure 3.3: Shear deformation of a powder sample: Coulomb friction (top), homogeneous shear throughout sample (bottom).

A well known powder flow model in soil mechanics, based on the "toppling bookrow" model, is the double sliding model (Spencer 1964, De Josselin de Jong 1971, Teunissen et al. 1988). The model supposes that deformation occurs by a superposition of two simple shearing motions along shear zones on which failure occurs according to Coulomb's criterion. This model has not been applied in powder technology.

Once shear regions have formed in a powder sample, they have a strong directional influence on the flow behavior of powder. This is experimentally shown by

Wong and Arthur (1985) and will be further discussed in chapter 5. A microscopic view on the formation of shear regions is given by Oda et al. (1998 and 2000). In their work a reasonable accordance between simulation and laboratory tests is reached. It is based on biaxial compression tests with two dimensional assemblies of oval particles and with real biaxial tests on two natural sands (200  $\mu\text{m}$  and 500  $\mu\text{m}$ ). In the consolidation step of the experiment column-like structures are reported that grow parallel to the major principal stress direction. During failure a high gradient of particle rolling instead of sliding is generated.

A microscopic investigation of the shear region of cohesive powder is not performed until now. In this chapter, the ND technique is used to follow the translation, rolling and bulk density of particles in a shear region.

### 3.3 Theory of Neutron Depolarization

The Neutron Depolarization (ND) technique is based on the loss of polarization of a polarized neutron beam after transmission through ferromagnetic substances. Ferromagnetism occurs in materials that can be permanently magnetized upon application of an external magnetic field. The magnetization can be reversed by applying a field in the opposite direction larger than the so called coercive field. Materials with large coercive fields are called permanent magnets. These are used in magnetic recording devices such as tape recorders (Por 1995). Much of the theory in this paragraph is taken from Rosman (1991), Por (1995), Rekveldt (1989) and Velthuis (1999).

The microscopic investigation of the shear region is possible because a special sample is used. A small fraction of this sample consists of ferromagnetic powder that is magnetized in the z direction by a magnetic field (0.5 T) of an electromagnet. The individual vectors of the ferromagnetic particles can only have a limited number of orientations with positive z component after the external pulse of the electromagnet. In the next step of the experiment particles are translating and rotating due to different actions applied on the sample, e.g. consolidation and shear. If a ferromagnetic particle rotates, its magnetic vector will rotate with it. This results in a rotation of the average magnetization of the sample. This rotation of the magnetization can be measured with the ND technique (figure 3.4).

In the ND technique a neutron beam is polarized in x, y or z-direction. This beam is sent through the sample which has a certain average magnetization. This magnetization causes the neutron beam to depolarize. The polarization of the outgoing beam ( $\underline{P}$ ) is analyzed in x, y and z-direction. The loss of polarization of the incoming neutron beam can be expressed in the so-called (3\*3) depolarization or rotation matrix  $\underline{D}$  (equation 3.1).

$$\underline{P} = \underline{D} \underline{P}_0 \quad (3.1)$$

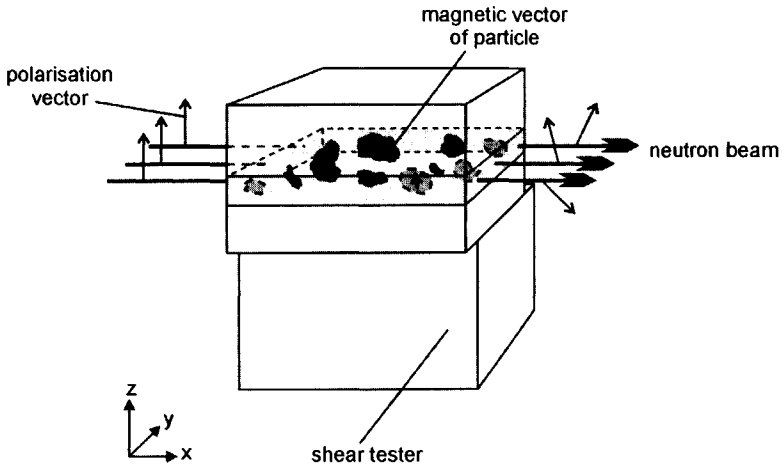


Figure 3.4: Principle of the Neutron Depolarization technique.

In the Larmor approach of neutron depolarization the polarization vector of the incoming neutron beam rotates over a certain angle around the magnetic vector of the sample (figure 3.5). This is called Larmor precession.

The precession angle is given by:

$$\varphi = c_2 \lambda B_s d_{\text{eff}} \quad (3.2)$$

with  $c_2 = 4.6368 \cdot 10^{14} \text{ T}^{-1}\text{m}^{-2}$ , and with the effective magnetic thickness of the sample,  $d_{\text{eff}}$ , being:

$$d_{\text{eff}} = c_{\text{ferrox}} d_{\text{tester}} \quad (3.3)$$

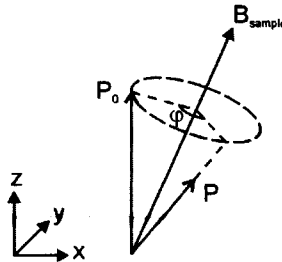


Figure 3.5: Rotation of a polarization vector over an angle  $\varphi$ .  $P_0$  is the average orientation of the spin of the neutrons before they enter the sample.  $P$  is the orientation after the sample. Because of averaging of the different orientations the size of this vector is smaller.  $B_{\text{sample}}$  is the average magnetic field of the sample (Schrauwers, 1998).

The effective thickness is a measure for the concentration of magnetic particles. The matrix elements  $D_{ij}$  of equation 3.1 are formed from the neutron detector intensities  $I_{\text{sh}}$  and  $I_{ij}$  by:

$$D_{ij} = \frac{I_{\text{sh}} - I_{ij}}{I_{\text{sh}}} \quad i, j = \{x, y, z\} \quad (3.4)$$



Here "j" refers to the initial polarization direction of the neutron beam and "i" represents the direction that is analyzed. The shim intensity  $I_{sh}$  is the intensity of the fully depolarized beam.  $I_{sh}$  can be determined from the measured intensities  $I_{zz}$  and  $I_{z\bar{z}}$ , where "Z" indicates the negative "z" direction.

$$I_{sh} = \frac{I_{zz} + I_{z\bar{z}}}{2} \quad (3.5)$$

In the experiments  $I_{sh}$  is corrected for the background intensity and for the monitor intensity. The monitor intensity is the intensity of the neutron beam coming directly from the nuclear reactor. This intensity fluctuates over time and causes  $I_{sh}$  to fluctuate as well. The background intensity is the measured intensity at the detector when the incoming neutron beam is closed. It is measured in each experiment by placing a piece of Cadmium in the neutron beam which absorbs all neutrons of the incoming beam. The complete correction on the measured  $I_{sh}$  is given as:

$$I_{sh} = \frac{I_{sh,measured} - I_{background}}{I_{monitor}} \cdot I_{average,monitor} \quad (3.6)$$

During the experiments the monitor device failed now and then. This can be seen as large fluctuations in the intensity of the incoming neutron beam, while the reactor was operating at normal conditions and with normal fluctuations. For these experiments  $I_{sh}$  could not or just partially be corrected for the monitor intensity. In these cases the normalization with the monitor is skipped, assuming that the intensity of the incoming neutron beam was constant.

The intensity of the fully depolarized beam only depends on the number density of particles in the beam. This relation is given by:

$$I_{sh} = I_0 \exp(-\Sigma \rho_{bulk}) \quad (3.7)$$

in which  $\rho_{bulk}$  is the bulk density of the sample and  $\Sigma$  is a constant that is proportional to the total scattering cross section depending on the material used.  $I_0$  is the intensity when there is no powder in the sample holder. It follows from this equation that  $\ln(I_{sh})$  is proportional to the number of magnetic clusters if it is assumed that the magnetic clusters are distributed homogeneously in the powder.

From the elements of the depolarization matrix  $\underline{D}$  the mean magnetization in the x, y and z direction ( $\phi_x$ ,  $\phi_y$  and  $\phi_z$ ) of the sample can be calculated.

$$\phi_z = \arctan\left(\frac{D_{xy} - D_{yx}}{D_{xx} + D_{yy}}\right) \quad (3.8)$$

$$\phi_y = \arctan\left(\frac{D_{xz} - D_{zx}}{D_{xx} + D_{zz}}\right) \quad (3.9)$$

$$\phi_x = \arctan\left(\frac{D_{yz} - D_{zy}}{D_{yy} + D_{zz}}\right) \quad (3.10)$$

The measured values of  $\phi_z$ ,  $\phi_y$  and  $\phi_x$  are dependent on the number of particles in the neutron beam. Therefore, these values are corrected by dividing them by the effective thickness ( $d_{\text{eff}}$ ), which is a measure for the concentration of magnetic particles (equation 3.3). The concentration is determined from the shim intensity (equation 3.7). The orientation of the particles is calculated from the corrected mean magnetizations and defined by the angles  $\theta$  and  $\psi$  (figure 3.6).

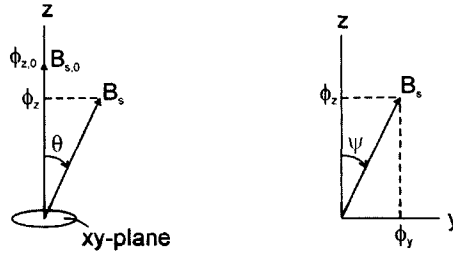


Figure 3.6: Change of the orientation angles of the particles. Left: rotation away from the z axis; right rotation around the x axis. In this picture it is assumed that no calibration errors exist.

The initial magnetization of the sample is always in the z-direction. The average rotation of the particles away from the z axis is expressed by the angle  $\theta$ . The average rotation from the z axis to the y axis is expressed by  $\psi$ . The angles are calculated from the mean magnetizations in y and z direction with equations 3.11 to 3.12. These equations take into account calibration errors in the mean magnetizations. For the angle  $\psi$  this means that only changes in the rotation relative to a starting position ( $\phi_{y,0}$ ) can be measured.

$$\theta = \frac{2}{\pi} \left( 1 - \frac{\phi_z}{\phi_{z,0}} \right) \quad (3.11)$$

$$\psi = \arctan \frac{\phi_y - \phi_{y,0}}{\phi_z} \quad (3.12)$$

The determinant of the depolarization matrix gives information about the size of the magnetic clusters ( $\delta$ ) and also depends on the density of magnetic particles.

$$\text{Det} = \exp(-cB_s^2\delta d_{\text{eff}}) \quad (3.13)$$

$$c = \frac{(c_2\lambda)^2}{2} \quad (3.14)$$

The effective thickness is defined in equation 3.3. The effective thickness and the magnetic cluster size are both proportional to  $\ln(\text{Det})$ .

### 3.4 Instruments and experimental setup

#### 3.4.1 Polyaxis neutron depolarization analyzer (PANDA)

The nine elements of the depolarization matrix  $\underline{D}$  are measured directly by adjusting the polarization of the incoming and outgoing neutron beam along one of the three orthogonal  $x$ ,  $y$  or  $z$  axes. This is done by two polarization rotators (D1 and D2). The principal setup of the ND technique is sketched in figure 3.7. It consists of a polarizer (P) and an analyzer (A) with the already mentioned polarization rotators D1 and D2. The sample S is placed on a  $z$ -translation table in a magnetically shielded box. After reflection at the analyzer the neutrons are detected by a  $^3\text{He}$ -gas counter (Det).

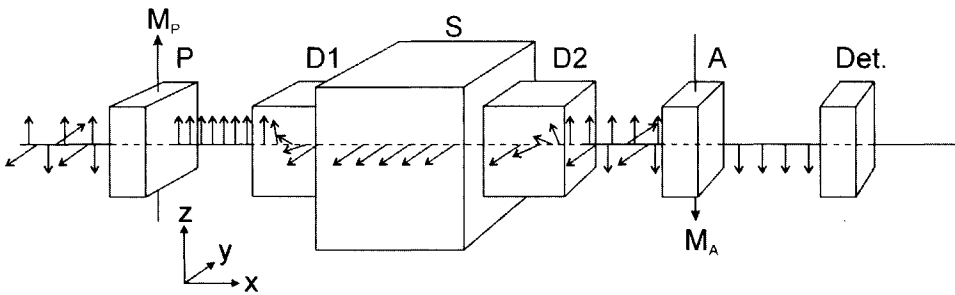


Figure 3.7: The Polyaxis Neutron Depolarization Analyzer (PANDA).  
See text for abbreviations.

The height of the neutron beam in all the experiments is 0.5 mm ( $z$  direction) and the width 10 mm ( $y$  direction). The velocity of the neutrons is characterized by their wavelength  $\lambda = 0.16$  nm. The sample is monitored perpendicular to the  $yz$ -plane over a distance of 10 mm by lifting it through the beam (in  $z$  direction) with the translation table. The unique setup is operated at the 2 MW swimming pool nuclear reactor Hoger Onderwijs Reactor HOR of the Interfaculty Reactor Institute of the Delft University of Technology.

#### 3.4.2 Small shear tester

The transmission of neutrons through the sample powder, BCR-limestone (paragraph 3.4.3), has been tested and a thickness of 25 mm is the optimum transmission length for an ideal measurement. Existing shear testers, like the Jenike Tester or the Peschl Cell, contain too large samples and, therefore, a small shear tester had to be built. This tester is made from aluminum, which is nearly transparent for neutrons, and plastic. The plastic components of the tester are not placed in the region that will be scanned by the neutron beam. This is because neutrons lose their energy very effectively in collisions with hydrogen atoms which results in a decrease of the intensity of the beam. Figure 3.8 shows a sketch of the small powder shear tester. The height of the

first version has been reduced later to create a filling tube. Figure 3.9 shows a picture of the tester.

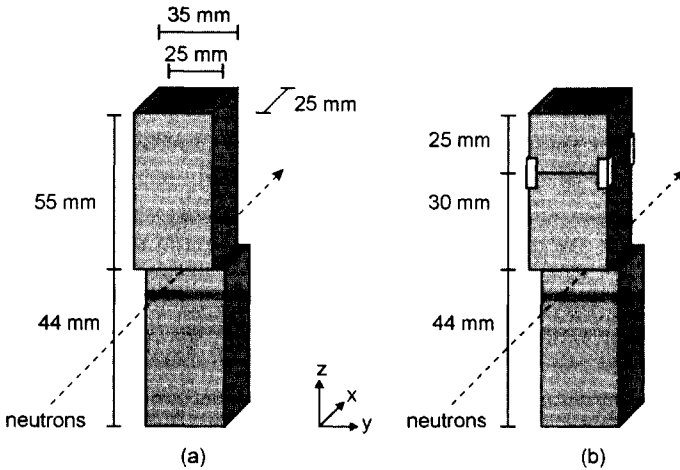


Figure 3.8: The large (a) and the adapted small (b) version of the small shear tester. The top part of version (b) is only used for filling and guidance for the consolidation weight.

The background intensity in each experiment is measured by covering a small piece of the tester with cadmium which absorbs neutrons and therefore blocks the neutrons coming from the reactor. Behind the cadmium shield the detector measures the background intensity. The scanning window of the tester is 0.5 cm both above and below the shear region.

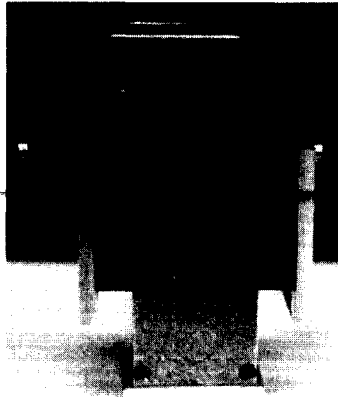


Figure 3.9: The small shear tester.

### 3.4.3 Sample powder

The ND technique only works with ferromagnetic materials. However, the standard material in powder flow behavior testing is BCR-limestone powder (Akers, 1991)

which doesn't have ferromagnetic properties. Therefore the BCR-limestone was mixed with 3.0 weight % ferroxdure particles ( $\text{Fe}_{3-x}\text{Ba}_x\text{O}_4$ ). The particle size distribution of the certified BCR-limestone is given in figure 3.10.

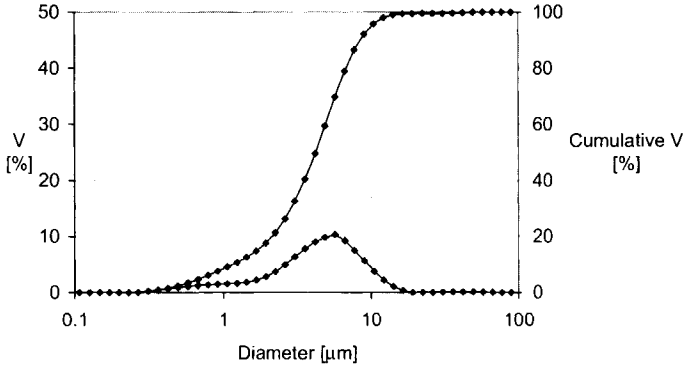


Figure 3.10: Particle size distribution of BCR-limestone (mean  $d_p = 4.2 \mu\text{m}$ ) measured by Malvern Mastersizer.

It is very difficult to measure the size distribution of ferroxdure because of its magnetic properties, but SEM measurements have shown that they have a diameter of approximately  $6 \mu\text{m}$  (figure 3.11). The measurement of the cluster size of the magnetic particles with the ND technique (figure 3.18) have shown that this estimation is correct.

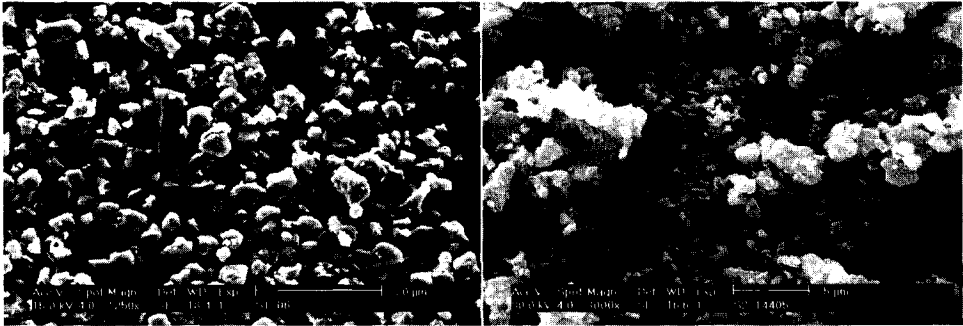


Figure 3.11: BCR-limestone (left; line indicates  $20 \mu\text{m}$ ) and ferroxdure (right; line indicates  $5 \mu\text{m}$ ).

In these experiments it is assumed that the ferroxdure particles behave exactly like the limestone particles. The validity of this assumption is difficult to estimate, but both powders are relatively small and cohesive forces will play an important role in their behavior. The influence of the magnetic particles on each other is negligible because the small magnetic field of a particle reduces with the third power of the reciprocal distance.

In the next figures the shim intensity and the magnetizations are given for the mixture of BCR-limestone and ferroxdure, which has not been magnetized. The error due to the number statistics of the counted neutrons is very low ( $< 0.1\%$ )

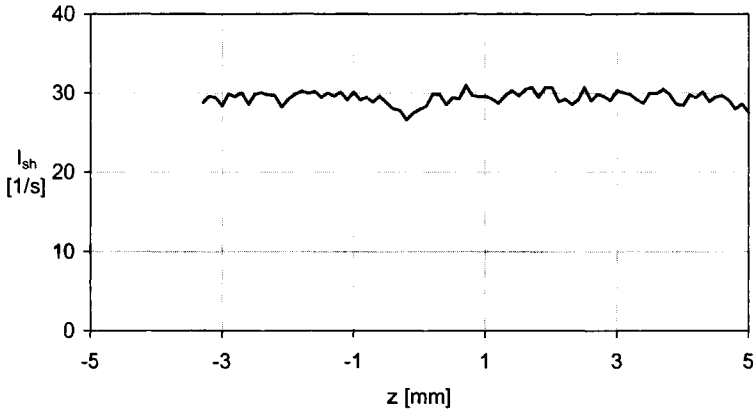


Figure 3.12: Shim intensity for a mixture of BCR limestone and ferroxdure (3 w%) which is not magnetized with an external magnetic field.

The variations in the measured intensity are due to the inhomogeneous bulk density in the sample. These fluctuations are caused by the sample, because exactly the same dependence is reproduced when the sample is scanned again.

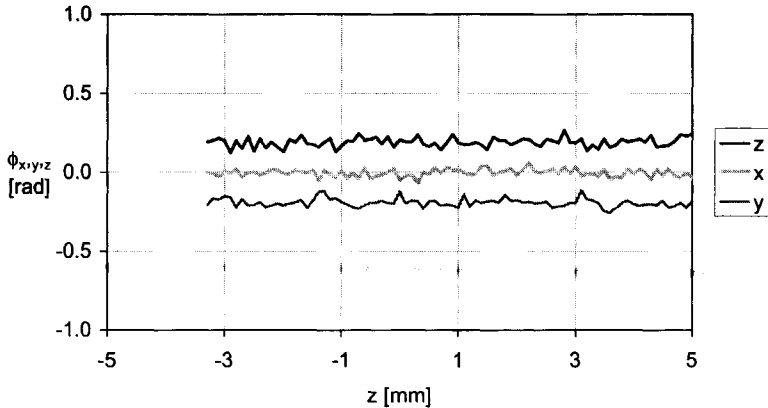


Figure 3.13: Neutron depolarization parameters, that are a measure of the magnetization in x, y and z direction for a mixture of BCR limestone and ferroxdure (3 w%) in the unmagnetized state. Differences between the curves are caused by systematic errors.

The fluctuations in the mean magnetization of the particles (figure 3.13) are because of the same reason real variations in the rotations of the particles as a function of z.

The values of  $\phi_x$ ,  $\phi_y$  and  $\phi_z$  should be around zero because there is no magnetization in any direction. For  $\phi_y$  and  $\phi_z$  in figure 3.13 this is not true, which is caused by systematic calibration errors in the setup. Because of this offset in  $\phi_y$  and  $\phi_z$ , the magnetization vector should be corrected. Therefore, the changes in the rotation are investigated in the following experiments and not the initial orientation.

This mixture is magnetized with a field of 0.5 T. After the sample preparation and magnetization the experiment is ready to start.

## 3.5 Consolidation experiment

In this experiment the bulk density and the rotation of the particles is investigated in a sample that is consolidated. Two types of consolidation are possible: firstly consolidation with increasing load, and secondly, consolidation with constant load as a function of time. The latter is called time consolidation.

### 3.5.1 Procedure

The consolidation experiment with increasing load is performed in the following way:

1. The tester is filled carefully and then gently preconsolidated with a small weight to prevent large cavities to exist. The initial volume of the sample is  $25 \times 25 \times 74 \text{ mm}^3$ .
2. The sample is weighted and the bulk density is calculated.
3. The sample is magnetized in the z-direction with 0.5 T.
4. The tester is placed in the PANDA.
5. The consolidation weight is placed and one hour of waiting should bring the sample height through the largest changes.
6. The sample is scanned. The longer the measuring time the more accurate the results are from a statistical point of view (the precision is equal to the square root of the total counts). However, the powder mixture is consolidating during the measurement and therefore the measuring time should be kept short. In practice one scan over the height took about 8 hours.
7. The sample height is measured.
8. Step 5 to 7 are repeated with higher consolidation weights.

### 3.5.2 Effect of increasing load

The experiment is performed stepwise with a sample of 35.4 g. In figure 3.14 the bulk density as a function of time is given. The height of the sample is measured after the scanning operation and is assumed to give the bulk density of the sample during the ND measurement.

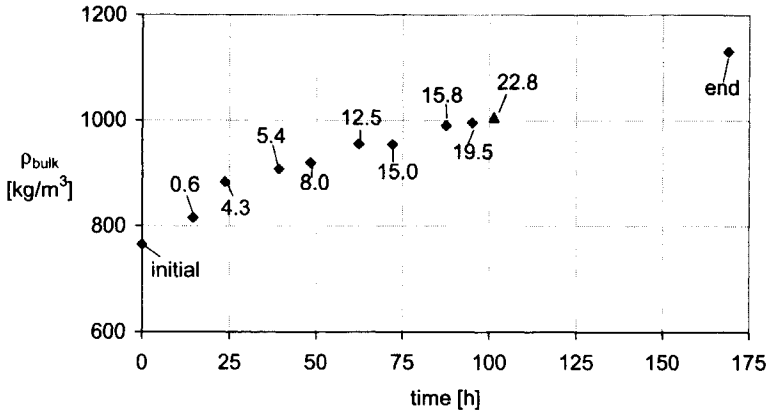


Figure 3.14: Change of the bulk density during the experiment. The numbers denote which consolidation (in kPa) corresponds with which average bulk density of the sample. The triangular point is interpolated.

According to equation (3.7)  $I_{\text{sh}}$  should decrease with increasing bulk density. Figure 3.15 shows indeed that  $I_{\text{sh}}$  decreases with the applied consolidation load.

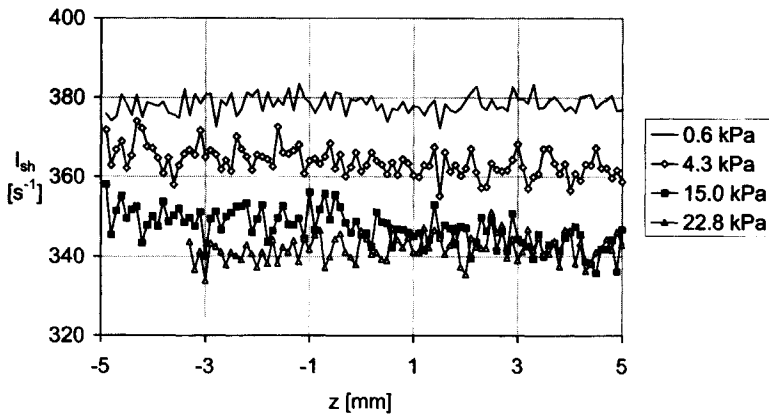


Figure 3.15: Decrease in  $I_{\text{sh}}$  for the different consolidation steps (values given). In between steps are left out for clarity reasons.  $I_{\text{sh}}$  is corrected for the monitor and background readings.

The relation between the bulk density and the intensity of the fully depolarized beam can be written as:

$$\ln(I_{\text{sh}}) = \ln(I_0) - \Sigma \rho_{\text{bulk}} \quad (3.15)$$

This means that  $\ln(I_{\text{sh}})$  is proportional to the bulk density and more precise to the concentration of particles. The change in  $\ln(I_{\text{sh}})$  should be proportional to the change of the bulk density. In order to see if the change of  $I_{\text{sh}}$  also depends on the position in



the tester, figure 3.16 presents  $I_{sh}$  versus the overall bulk density at three different positions: at the top, in the middle and at the bottom of measuring window of the tester. The  $I_{sh}$  values start at approximately the same value for all positions, but when more consolidation pressure is applied, a difference occurs over the height. The decrease in  $I_{sh}$  at the bottom is much less than that in the top of the tester. This means that the bulk density of the top part of the sample is higher than in the bottom of the sample. This gradient of the bulk density can be explained by the wall friction in the tester that prohibits the normal force to be transmitted.

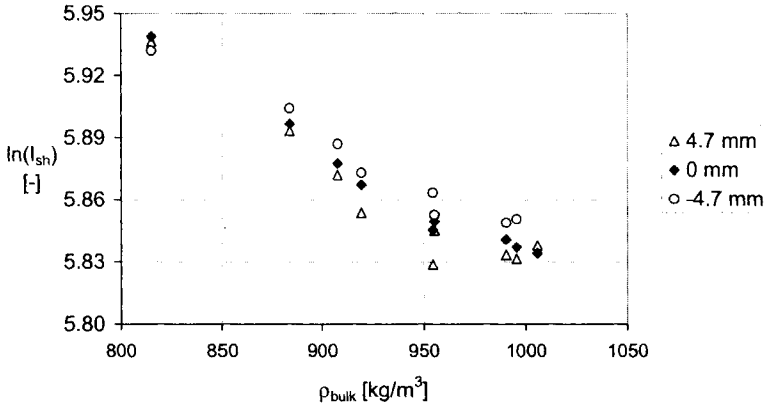


Figure 3.16: Decrease of  $I_{sh}$  for different heights in the sample versus the overall bulk density.

The results in figure 3.16 are fitted with equation 3.15 and  $I_0$  and  $\Sigma$  are determined. The bulk density used for the regression is the average bulk density of the whole sample. Therefore,  $I_{sh}$  is also averaged over the whole sample. The result of the linear fit is given in table 3.2 and figure 3.17.

Table 3.2: Results from regression.

$I_0 =$	584.6	$\pm$	19.1	[counts/s]
$\Sigma =$	$5.4 \cdot 10^{-4}$	$\pm$	$3.4 \cdot 10^{-5}$	[m <sup>3</sup> /kg]

The magnetic ferroxdure particles that are mixed in the limestone powder form clusters if they would come in contact with each other. Magnetic forces will keep them together. The clustering of the magnetic particles change the behavior of the particles in the shear zone and should be kept at a minimum level. The determinant of the depolarization matrix gives information about the size of the magnetic clusters. The determinant also depends on the density of magnetic particles (Rekveldt, 1989) which is determined from the shim intensity. The cluster size can be calculated from equation 3.13:

$$\delta = \frac{\ln(\text{Det})}{-cB_s^2 d_{eff}} \tag{3.16}$$

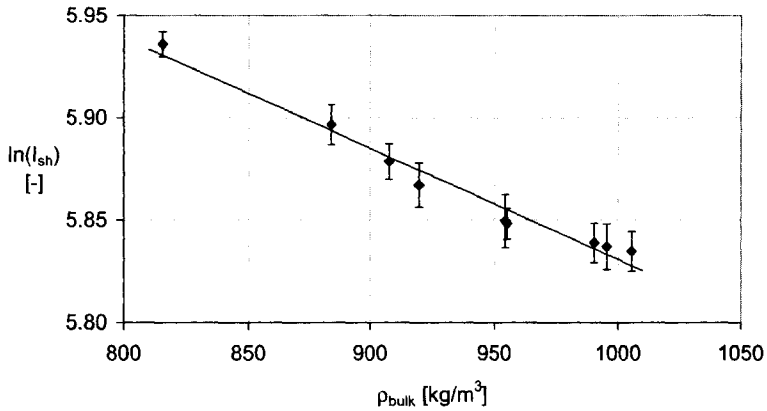


Figure 3.17: The measured relation between the bulk density and the natural logarithm of  $I_{\text{sh}}$  according to equation 3.15. The error bars indicate two standard deviations.

The cluster size as a function of the overall bulk density is given in figure 3.18. The average cluster size is  $6.6 \mu\text{m}$  ( $\pm 0.6 \mu\text{m}$ ). From figure 3.18 it can be concluded that the cluster size does not change significantly with increasing consolidation.

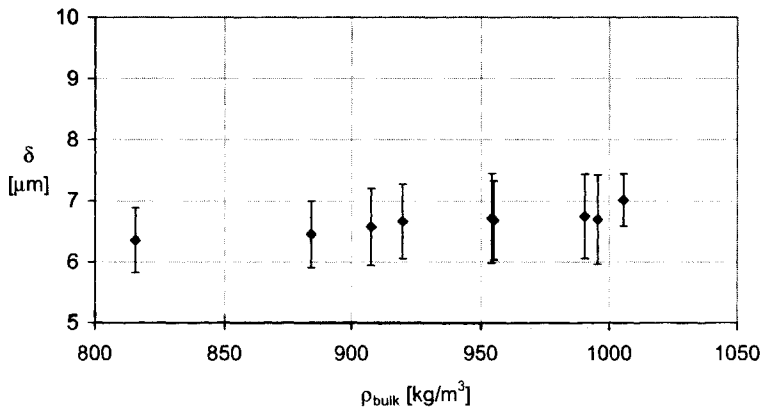


Figure 3.18: The size of the magnetic clusters versus the bulk density.

In this consolidation experiment the concentration of particles and the bulk density will increase with time and with the applied consolidation load. This happens because particles translate and rotate. The rotation of the particles during the consolidation, is expected to mainly take place around the x-axis or the y-axis. Neither of these two rotations is preferred when it is assumed that the sample is isotropic.

Information about the rotation is derived from the measured values of  $\phi_z$ ,  $\phi_y$  and  $\phi_x$ . These parameters are dependent on the number of magnetic particles in the

neutron beam. Therefore,  $\phi_z$ ,  $\phi_y$  and  $\phi_x$  are corrected by dividing them by the effective thickness ( $d_{eff}$ ) - which is a measure for the concentration of magnetic particles. For this correction equation 3.3 and 3.15 and the values in table 3.2 have been used. The results of this calculation - in the form of  $\phi_z/d_{eff}$  etc.- are presented in figures 3A.1 in the appendix of this chapter. Figures 3A.1 shows that no preferred rotation in the x direction exists, but in the y direction there is a change in the magnetization. It is believed that this is due to a small ridge in the tester that occurs because the two halves of the tester are not perfectly aligned. The magnetization in the z direction changes very clearly as is expected. The actual rotation of the particles, as defined by  $\theta$  in figure 3.6 is presented in figure 3.19.

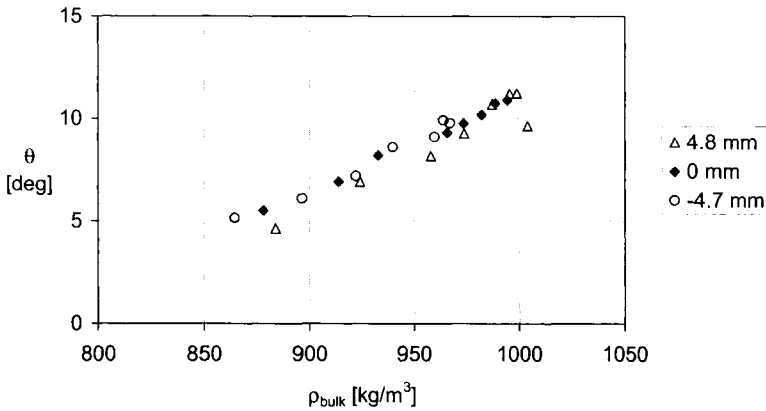


Figure 3.19: Rotation of particles as defined in figure 3.6 with increasing bulk density.

As expected, the  $\theta$  rotation increases with each step in which a higher consolidation load is applied. The question raises how the rotational movement of the particles relates to the translational movement. A measure for the translation can be calculated from the relative increase of the bulk density at each position in the tester (equation 3.15 and table 3.2). It should be remarked that the height of the whole sample decreases and that different slices of the sample pass at a certain z value. Therefore, the changes in the bulk density are not only due to the change of a specific slice but also due to the inhomogeneity of the bulk density over the height. This effect is neglected in this calculation. The ratio of the rotation versus the translation is given in figure 3.20. It appears that the change of the rotation is small after an initial effect with respect to the translation for increasing bulk density. The increase of the consolidation load does increase the number of particles per volume element, but this has no visible effect on the rotation.

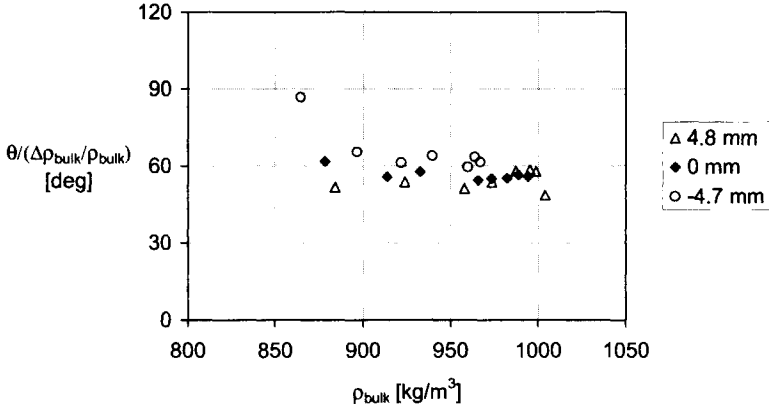


Figure 3.20: Ratio between the rotation and the translational movement of the particles at different heights in the tester.

### 3.5.3 Effect of time

The procedure for this experiment differs slightly from the procedure for the experiment with increasing consolidation. The tester has been filled with 34.5 g of the powder mixture of limestone and ferroxdure. A consolidation load of 4.3 kPa has been placed on top. After a scan from top to bottom of the sample the sample is moved automatically to the starting position ( $z = 5$  mm), which took about 5 minutes, and the scan restarts without increase of the normal weight. This is done for a period of 68 hours. The height of the sample has not been recorded during the experiment. Only the overall bulk density at the begin and at the end of the experiment are known.

The bulk density can, however, be calculated from the shim intensity. The shim intensity in this experiment is only corrected for the background intensity (as in equation 3.17) and is not corrected for the monitor as described in equation 3.6, because the monitor device failed.

$$I_{\text{sh}} = I_{\text{sh,measured}} - I_{\text{background}} \quad (3.17)$$

The overall bulk density at the end of the experiment was 872 kg/m<sup>3</sup>. By using equation 3.15 and  $\Sigma$  from table 3.2, the bulk density in the sample at each height can be calculated. The calculated bulk densities (figure 3.21) show an increase of approximately 75 kg/m<sup>3</sup> over a time period of 68 hours.

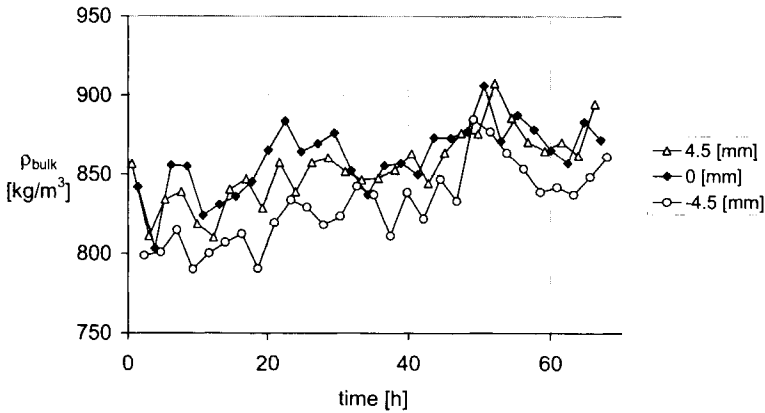


Figure 3.21: Increase of the bulk density in the sample at three different heights as a function of time for a consolidation load of 4.3 kPa.

The magnetizations of the particles are presented in figure 3A.2 in the appendix of this chapter. They are corrected for the concentration of magnetic particles. This concentration,  $d_{eff}$ , is calculated by means of equation 3.3 and 3.15, and table 3.2. They show clearly that the time consolidation only has an effect on the magnetization in the  $z$  direction and that no preferred orientation in the  $x$  and  $y$  direction occurs. The  $\theta$  rotation as defined by equation 3.11 is presented in figure 3.22.

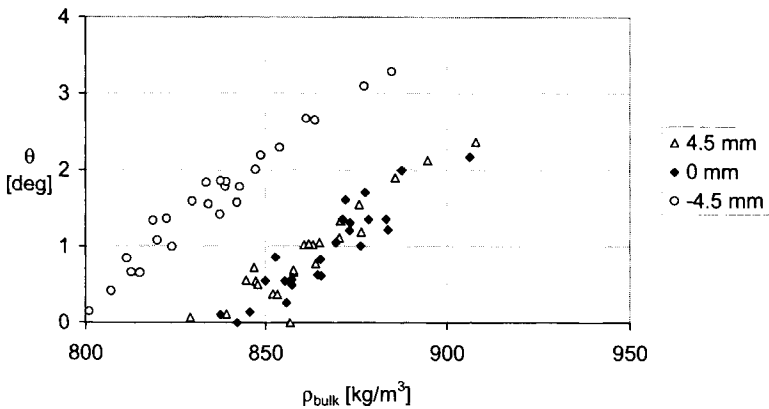


Figure 3.22: Rotation of the particles as a function of the bulk density with a consolidation load of 4.3 kPa.

The rotation increases steadily in time and is proportional to the bulk density. It is remarkable that the rotation is quite different at the bottom of the scanned sample compared to the rotation in the middle or in the top of the sample. This could be due to inhomogeneity of the sample.

Again the ratio between the translational movement and the rotational movement is calculated as described in paragraph 3.5.2. Figure 3.23 shows the result. The time consolidation shows a different effect as the consolidation experiment with increasing load (figure 3.20): the rotation initially increases relative to the translation for increasing bulk density, but seems to become constant at higher bulk densities.

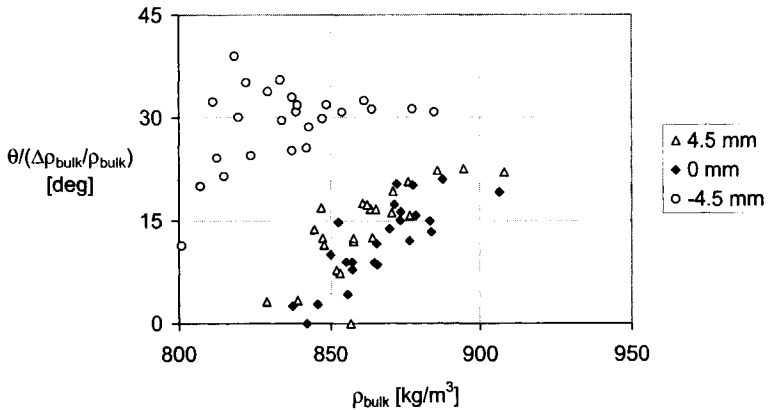


Figure 3.23: Ratio between the rotation and the translational movement of the particles as a function of bulk density with a consolidation load of 4.3 kPa.

The consolidation experiment in this paragraph has been performed in approximately three quarters of the time in which the experiment with increasing load as described in paragraph 3.5.2 has been performed. Therefore, time consolidation will also have had an effect on the results of the increasing load experiment. It is, however, expected that the contribution to the rotation is relatively small (compare figure 3.19 and 3.22).

It is concluded that time consolidation does not influence the shear experiments that follow, because these only take about 10 hours to perform. The change in the bulk density is very low in this time frame and the contribution to the rotation of the particles is relatively low as will be seen in the next paragraph.

## 3.6 Shear region experiment

In this paragraph shear regions are investigated in the small shear tester (section 3.4.2). The goal is to gather information about the shape and size of the shear regions and to estimate how much the particles rotate and translate in the shear region.

### 3.6.1 Procedure

A sequence of shear deformations is applied to a sample on which a certain consolidation load works. The sample is monitored after each shear step during which no shear deformation occurs. The exact procedure of an experiment is as follows:

1. The tester is filled carefully and then gently preconsolidated with a small weight to prevent large cavities. This is done during the filling under and over the place

where later the shear zone will be. The initial volume of the sample is  $25 \times 25 \times 74$  mm<sup>3</sup>.

2. The sample is weighted and the bulk density is calculated.
3. The sample is magnetized in the z-direction with 0.5 T.
4. The tester is placed in the PANDA.
5. The consolidation weight is placed. The sample is given time to consolidate. If no further visual change occurs in the height the procedure is continued.
6. The sample is scanned during a period of minimal 8 hours. How longer the measuring time the more precise the results are from a statistical point of view (the error is equal to the square root of the total counts). The sample height is measured.
7. The sample is sheared by moving the upper half relative to the bottom half in small steps of 0.7 mm. The consolidation weight works on the sample during the shear.
8. The sample is scanned again.
9. Step 7. and 8. are repeated until the maximum possible deformation was reached (3.5 mm).

An overview of the consolidations used in the shear zone experiments is given in the table 3.3 below. In each experiment the complete depolarization matrix has been measured over a height of 1 cm. An example of a depolarization matrix is given in figure 3A.3 in the appendix of this chapter.

Table 3.3: Overview of shear zone experiments.

Consolidation [kPa]	Mass [g]	Shear deformation [mm]
4.3	39.6	0; 0.3; 0.7; 1.0; 1.4; 1.7; 2.1; 3.5
8.0	32.7	0; 0.7; 1.4; 2.8
15.8	38.0	0; 0.7; 1.4; 2.8
22.8	36.7	0; 0.7; 2.8

### 3.6.2 Bulk density

In principle the procedure of the experiments equals that of a shear experiment in the Jenike Tester. After filling the sample is underconsolidated and the bulk density will increase up to a constant value when the normal load is placed and shear deformation is applied. However, in the procedure used here the shear deformation is applied in steps and in between the powder sample is scanned. Therefore, the bulk density is not measured at steady-state shear.

The bulk density in the sample is calculated from the shim intensity by equation 3.15 and it is constant over the height of the sample. However, the bulk density did change as a function of applied shear deformations (figure 3.24). The bulk density of the experiment with a load of 4.3 kPa is only partially given due to practical problems in the measurement of the shim intensity (figure 3A.4).

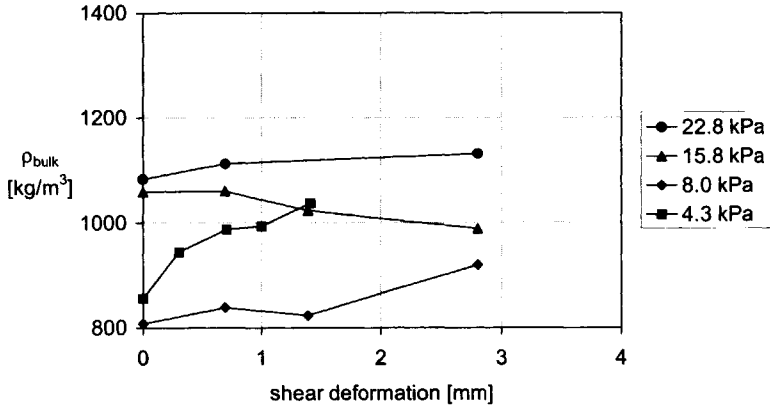


Figure 3.24: The bulk density in the shear zone ( $z = 0$  mm) as a function of the applied shear deformation.

The experiments with a consolidation load of 4.3 kPa, 8.0 kPa and 22.8 kPa show an increase in the bulk density. The experiment performed with a load of 15.8 kPa shows a decrease. The latter could be due to dilatancy. That would mean that this sample is overconsolidated. The height measurements of the whole sample do not confirm this conclusion, but these only indicate the overall bulk density. The other experiments are underconsolidated according to these results.

In the case of overconsolidated samples, it is questionable whether dilatancy can be measured with this procedure. The experiment should be adapted so that the shim intensity can be measured during the application of the shear. In such a setup the critical porosity could be measured directly. When the scanning is performed after the deformation, it could be that the volume change of the powder at the position of the shear zone is canceled out because the powder collapses again at the moment the shear deformation stops.

Thus, the bulk density does not give a consistent view. Both volume increase and decrease have been monitored for the different samples indicating overconsolidated and underconsolidated samples. None of the experiments show a steady-state bulk density that would indicate the existence of a critical porosity.

### 3.6.3 Rotation of particles in the shear zone

The magnetizations in the  $x$ ,  $y$  and  $z$  direction for the different shear deformations and consolidations are presented in the appendix of this chapter (figures 3A.5 to 3A.8). These magnetizations are corrected for the concentration of magnetic particles by the effective thickness ( $d_{\text{eff}}$ ). The magnetization in the  $y$  direction changes as a function both of the shear deformation and of the position  $z$  while no change occurs in the  $x$  magnetization. This indicates that the particles prefer to rotate from the  $z$  direction to the  $y$  direction. In the initial powder sample the magnetic vector points in the  $z$ -direction. The shear is applied in the  $y$ -direction and particles are expected to rotate in the  $yz$ -plane around the  $x$ -axis (see figure 3.8). The experiments confirm this idea. The absolute values of the magnetization in the  $z$  direction decreases, but these



take place over the whole height of the scanned sample. This decrease shows the total rotation of the particles.

The mean magnetizations are used to calculate the  $\psi$  rotation of the particles as defined in figure 3.6. The results are given in figure 3.25. The  $\psi$  rotation does show significant changes and is the highest at the position where the shear region is forced upon the powder ( $z = 0$  mm). The  $\psi$  rotation increases when more shear deformation is applied. In some of the experiments (figure 3.25 b and c) the peak in the  $\psi$  rotation has a inclined base line. The slope of this baseline doesn't change with the applied deformation. Therefore, it is assumed that it is caused by a deviation in the alignment from the  $z$  axis during the initial magnetization of the sample.

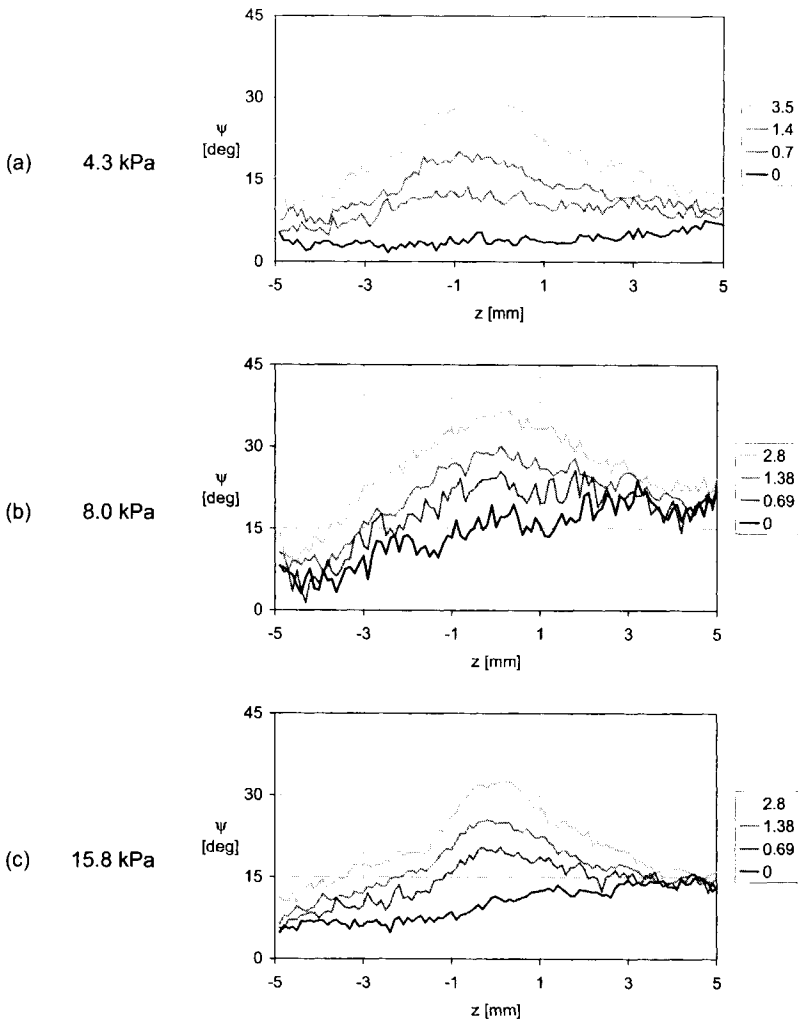


Figure 3.25a-c:  $\psi$  rotation during shear deformation for different consolidations (on the left) and for different shear deformations (on the right in mm). The figure continues on the next page.

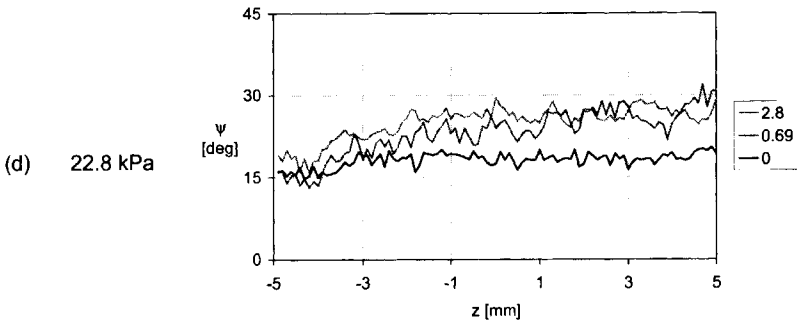


Figure 3.25d:  $\psi$  rotation during shear deformation for different consolidations (on the left) and for different shear deformations (on the right in mm). Continuation from figure on previous page.

It is also noticed that the initial  $\psi$  orientation of the particles changes with higher consolidation loads. This is in line with the experiment described in paragraph 3.5.2.

The relation between the applied shear and the  $\psi$  rotation is given in figure 3.26 for the particles positioned at the shear zone. The  $\psi$  rotation is proportional to the applied shear over a range of 3 mm. The shear deformation can also be seen as the translation the particles in the shear zone have to undergo.

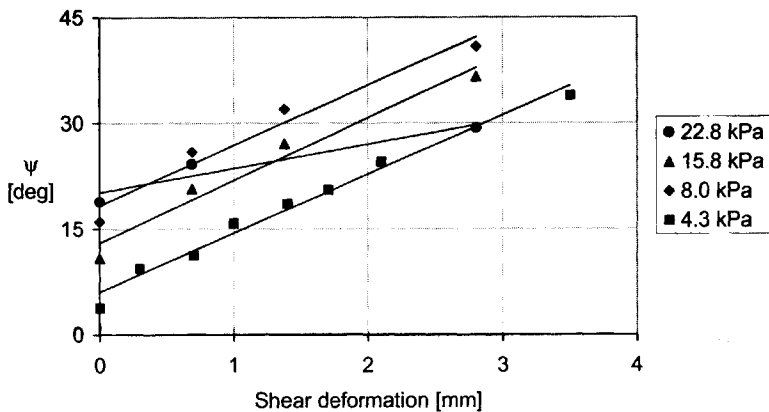


Figure 3.26:  $\psi$  rotation in the shear zone ( $z = 0$  mm) for different consolidations as a function of the applied shear deformation.

The slopes of the fitted lines in figure 3.26 are given in table 3.4. This slope is the same for the three lowest consolidation loads. The consolidation load of 22.8 kPa prohibits rotation more than the other three loads. The investigation did not make clear if the rotation versus translation ratio decreases with increasing load as figure 3.26 suggests. However, it would be expected that with increasing bulk density the rotation of the particles becomes more difficult.

Table 3.4:  $\psi$  rotation per applied deformation.

load [kPa]	$\psi$ rotation / translation [deg/mm]
4.3	8.4
8.0	8.5
15.8	8.9
22.8	3.4

The rotations in these shear experiments are much larger than those obtained in the consolidation experiments in figures 3.19 and 3.22 which leads to the conclusion that the application of a shear deformation causes much more rotation of the particles than pure consolidation. In both the shear experiments and in the consolidation experiments the rotation occurs in a fixed ratio to the translation. However, in the consolidation experiments this happens after an initial increase in this ratio.

### 3.6.4 Width of the shear zone

The position of the peak in the  $\psi$  rotation is the calibrated  $z = 0$  mm position but sometimes it shifts slightly downwards. The maximum measured shift is less than 1 mm for the experiment with the 4.3 kPa load. This shift is thought to be due to time consolidation. Most of the shifts are within 0.3 mm and this is within the precision of the calibration of the  $z = 0$  mm position.

In figure 3.27 the width of the peaks is given at half height of the peak. This width is determined by fitting the  $\psi$  rotation peaks with a Lorentzian curve. It should be remarked here that the  $\psi$  rotation of the experiments with zero shear deformation have no peak and the values at zero deformation are therefore not given in the figure.

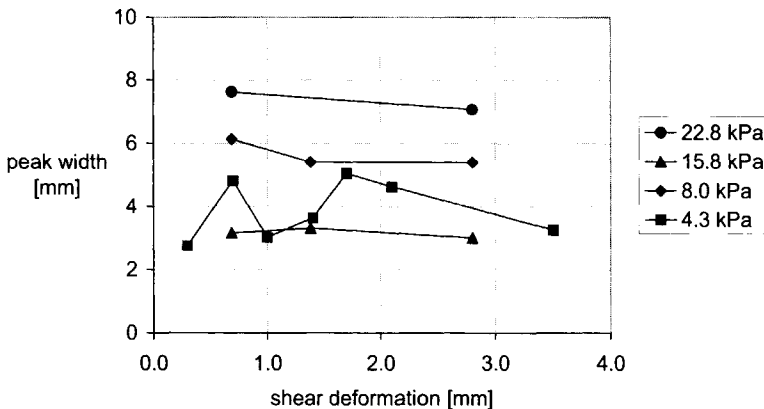


Figure 3.27: Width of the  $\psi$  rotation peak at half height as calculated from a Lorentzian fit for different consolidations (on the right).

The peak width remained approximately constant for increasing shear deformation. Schwedes (1971) observed an increase of the shear zone for an underconsolidated sample. Because the applied shear deformations are comparable with those in the

Jenike Tester it is assumed that the shear zone in this small shear tester has reached a certain equilibrium size. If there was an increase in size, it will have taken place within the first deformation.

The peak width increases with higher consolidation loads. The exception to this statement is the experiment with a load of 15.8 kPa, which has a small region. According to Schwedes (1971), overconsolidated samples have a relatively smaller shear region. The only experiment that showed an increase in the bulk density and was therefore overconsolidated is the one with a load of 15.8 kPa (figure 3.24), the other three experiments are underconsolidated. This observations confirms the conclusion of Schwedes. In the underconsolidated experiments, a higher consolidation load increases the width of the shear region, probably because particles are in closer contact with each other and cannot move freely without disturbing others.

Literature states that the width of a shear zone is about 10 particle diameters for non-cohesive particles, as mentioned in paragraph 3.1. This is too small to detect with the neutron beam which is 0.5 mm in size. In these experiments the  $\psi$  rotation of the particles extents a width of the shear region of 1000 to 2000 particle diameters. In this shear region particles can rotate more or less homogeneously or regions of stagnant particles are separated by a network of shear zones which are much smaller than the shear region width. Nevertheless, the rotation increases with increasing shear deformation throughout the whole shear region with a maximum rotation in the center and a minimum rotation at the sides.

The width of the shear zone given by literature is always measured in samples of fairly large particles (often sand): 100  $\mu\text{m}$  and more. The particles in the powder sample of the experiments presented here are much smaller and are cohesive. The cohesion probably makes the existence of shear zones with in between stagnant zones in the shear region less likely, because particles are more strongly bounded to each other.

### 3.6.5 Shape of the shear region

The measurement of the rotation of the particles as a function of the height (figure 3.25) does not give direct information about the exact shape of the shear region. Particles in the middle of the shear region rotate more than particles at the outer sides. **This brings the idea of a lens shaped shear zone** in which the particles move and rotate over each other. This shape is shown by Schwedes (1971) in figure 3.2.

The shear experiments have been repeated in order to photograph the shear plane. The two halves of the small shear tester were carefully taken apart, which resulted in two mirrored patterns in the powder. Two series of photos have been made: one series with increasing shear deformation keeping the consolidating weight at 15.4 kPa (figure 3.28) and one series with increasing consolidating weight for a shear deformation of 0.7 mm (figure 3.30). The left picture is always the top half of the tester and the right picture the bottom half. Positioned in the tester, the top half was moved to the right while the bottom half stood still. The arrows in the pictures (both on the top and the bottom part) indicate the direction of movement of the top half.

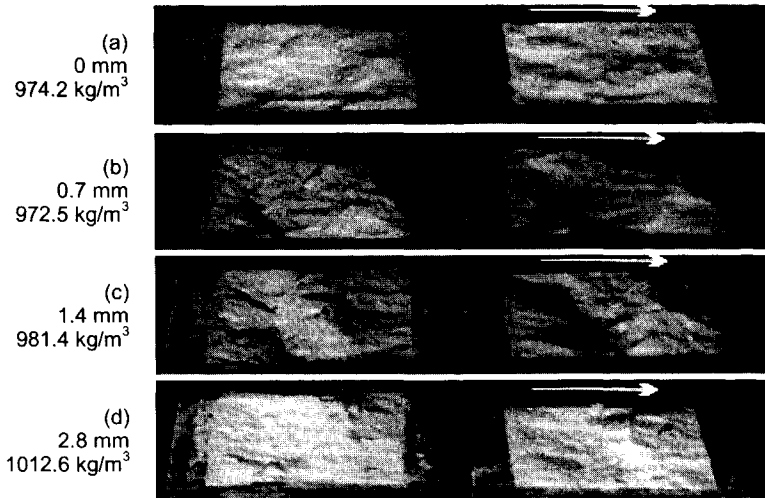


Figure 3.28: Shear planes (left: top part; right: bottom part; arrow indicates movement of top part) photographed with increasing shear (right column) with a consolidation of 15.4 kPa.

Without shear deformation the rupture plane between the top and bottom half of the tester looked as in figure 3.28a. When shear was applied a typical pattern occurred in the powder. This pattern has a wave form: from left to right the plane first moves down and then up. Two pits are formed: one on the left side into the bottom part of the sample and one on the right side into the top part of the sample (figure 3.29). In figure 3.28 this is most clearly seen in experiments (b) and (c), but it is also present in (d). From the figures it could not be distinguished how the size or position of the wave changed with increasing shear deformation.

The same wave is seen in the series of experiments in which the consolidating load changed (figure 3.30). In both series, some of the pictures showed horizontal cracks which indicates that the shear zone could be lens shaped (figure 3.29). The ND technique can be used to investigate the shape of the shear region in more detail by narrowing the neutron beam in both x and z direction.

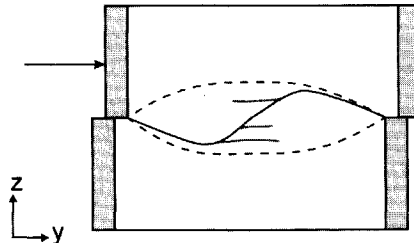


Figure 3.29: Sketch of shear zone observations; dotted line: lens shaped shear zone; solid line: wave shaped shear zone; gray line: cracks.

The size and shape of the shear region is influenced by the geometry of the tester, especially because it is relatively small. It is believed that the width of the shear region

is reduced compared to the shear region in a larger tester. There is not enough room for the shear region to grow in the vertical direction.

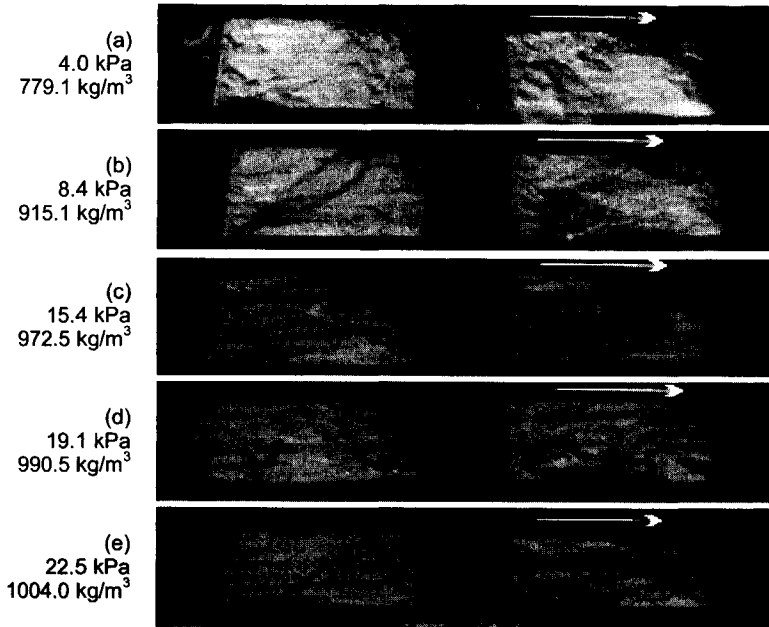


Figure 3.30: Shear planes (left: top part; right: bottom part; arrow indicates movement of top part) photographed at a shear deformation of 0.7 mm and different consolidation weights (right column).

### 3.7 Conclusion

In this chapter the shear region in a mixture of cohesive BCR-limestone ( $d_p = 4.2 \mu\text{m}$ ) and 3 weight percentage ferroxdure ( $d_p = 6 \mu\text{m}$ ) has been visualized by using the Neutron Depolarization technique. Especially for use with this technique, a small shear tester has been developed with which a shear region can be forced upon the sample. Shear deformation has been applied in a number of steps. After each step the sample has been scanned, leading to information about the bulk density, the size of magnetic clusters, the rotation of the particles and the width of the shear region. ND proved to be a very suitable and precise technique and, as far as known, the measurement of the rotation of particles in a shear region is unique.

In the first set of experiments, this setup has been used to investigate the effect of consolidation on the powder mixture. The consolidation experiment has been performed with increasing load and as a function of time with a constant load. In both types rotation occurred throughout the sample. The amount of rotation reached a constant value compared to the translational movement of the particles with increasing bulk density.

The second type of experiments dealt with shear deformation. It has been shown that the shear plane in a direct shear tester is not horizontal, but occurs in region. This means that results of this type of tester are inaccurate because they are based on the

assumption of a flat shear plane. The particles in the shear region have a preferred rotation in the direction in which the shear is applied. This rotation is proportional to the applied shear up to a deformation of 3 mm. The width of the shear region did not change after the first deformation step (0.7 mm) and it is 1000 to 2000 times the diameter of the particles. It is not clear whether in this shear region all particles rotate or smaller shear zones exist. Literature predicts a width of a shear zone for cohesionless sand particles ( $d_p = 500 \mu\text{m}$ ) of 10 particle diameters. It is expected that a shear zone in powder is different because of cohesion.

The ND technique indicated that the shear region is lens-shaped. Direct observation of the shear plane after taking the two halves of the tester apart showed a typical wave pattern in the powder that first moves down and then upwards in the direction of the shear deformation. By restricting the neutron beam not only in height but also in width, more detailed information can be obtained about the shape of the shear region in the powder with the ND technique.





## Appendix

## 3A.1 Data increasing consolidation experiment

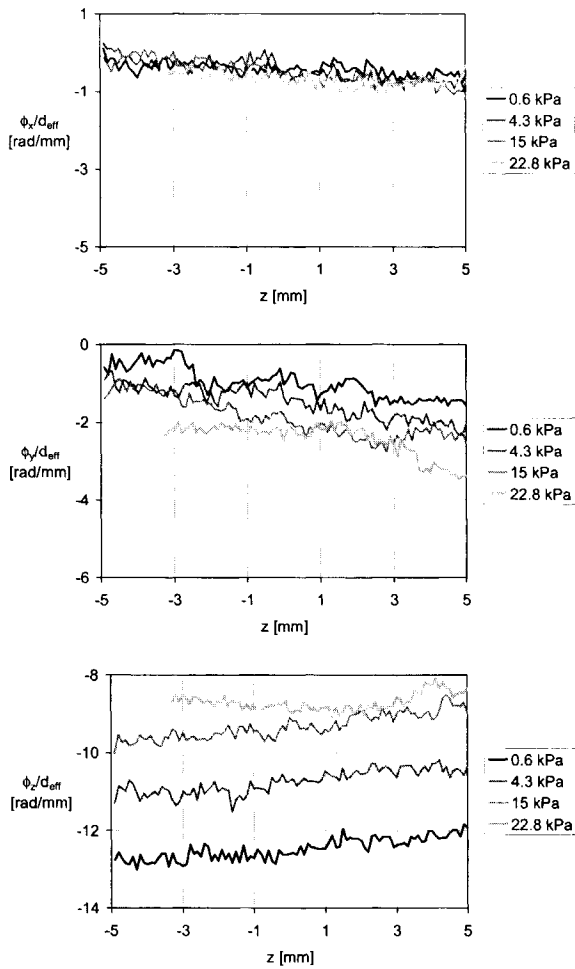


Figure 3A.1:  $\phi_x$ ,  $\phi_y$  and  $\phi_z$  corrected for the concentration of magnetic particles in three directions for increasing consolidation load.

### 3A.2 Data time consolidation experiment

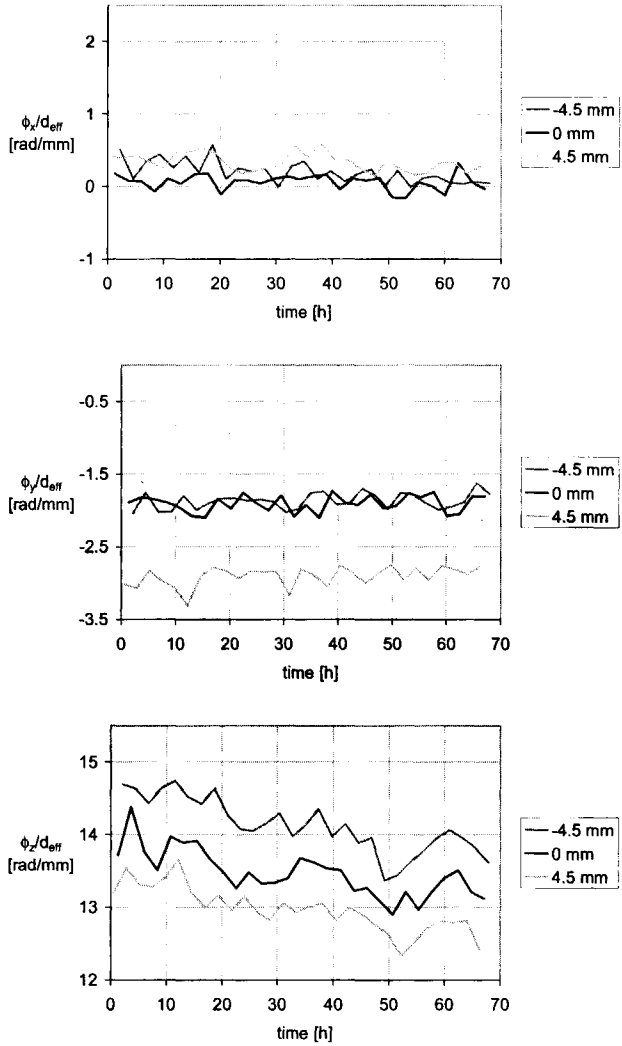


Figure 3A.2:  $\phi_x$ ,  $\phi_y$  and  $\phi_z$  corrected for the concentration of magnetic particles in three directions for time consolidation.

### 3A.3 Data shear plane experiment

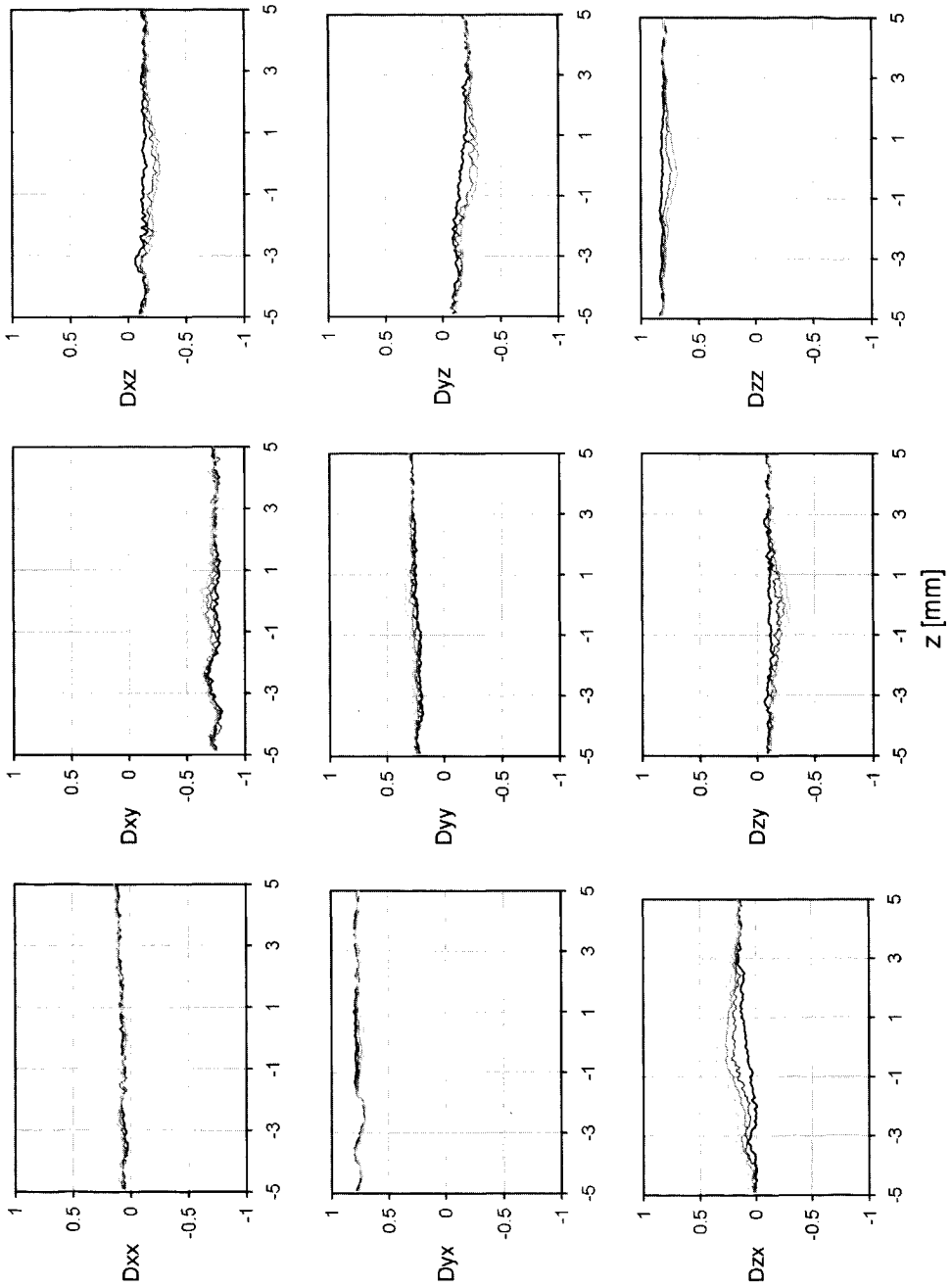


Figure 3A.3: Example of the depolarization matrix of a shear experiment with a consolidation of 15.8 kPa.

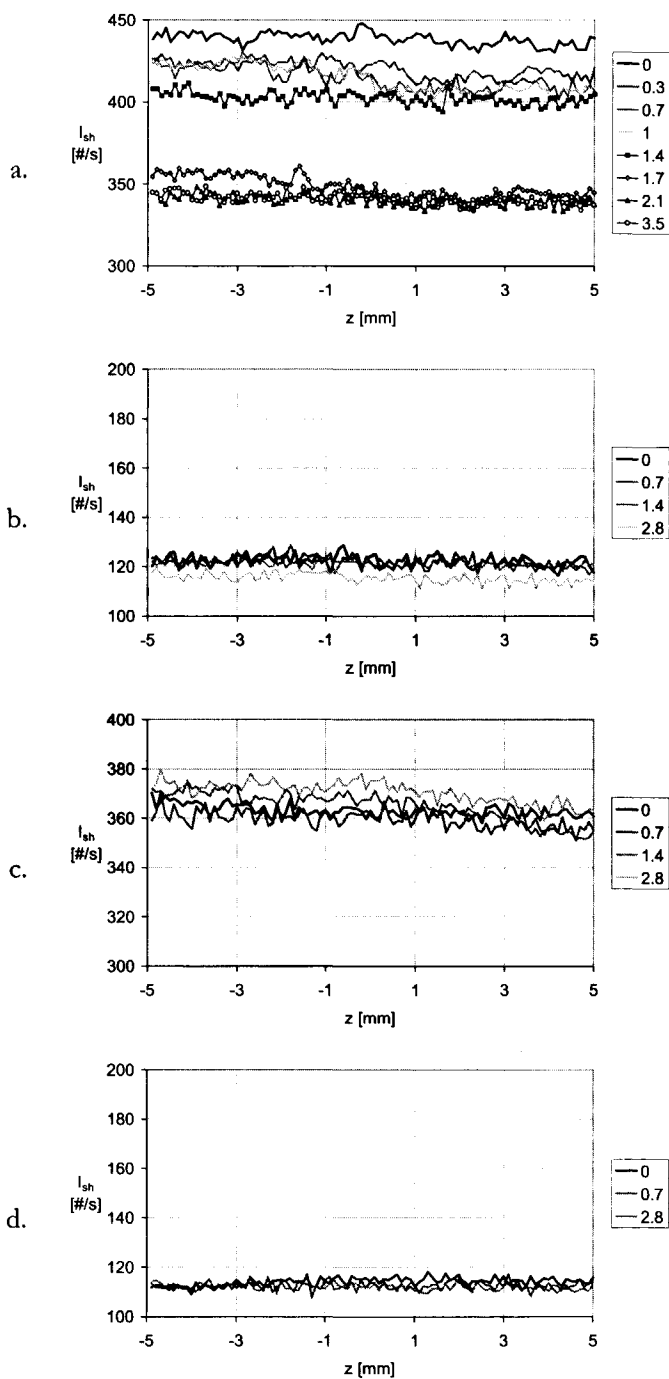


Figure 3A.4:  $I_{sh}$  as function of the height in the tester for the shear experiments (a 4.3 kPa; b. 8.0 kPa; c. 15.8 kPa; d. 22.8 kPa).

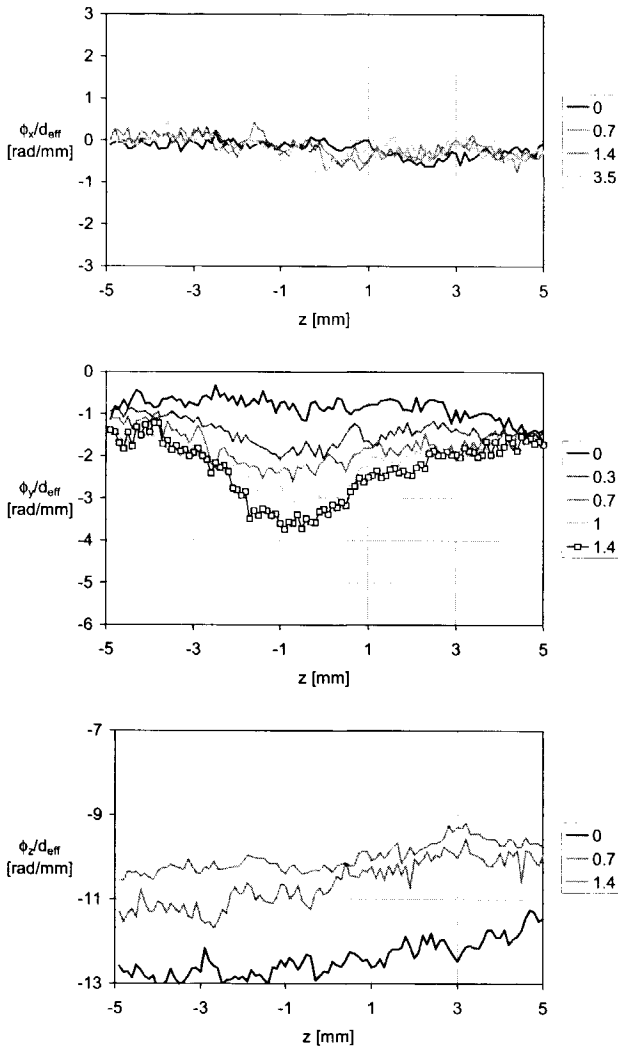


Figure 3A.5: Magnetization in the x, y and z direction in the shear experiment with a consolidation of 4.3 kPa. The shear deformation is given on the right in mm.

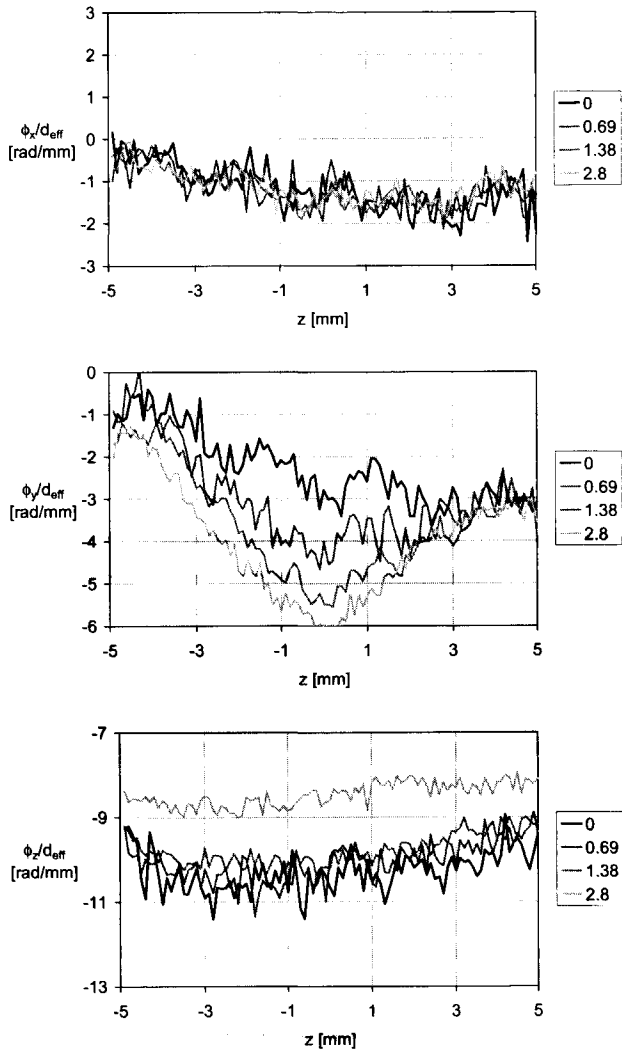


Figure 3A.6: Magnetization in the x, y and z direction in the shear experiment with a consolidation of 8.0 kPa.

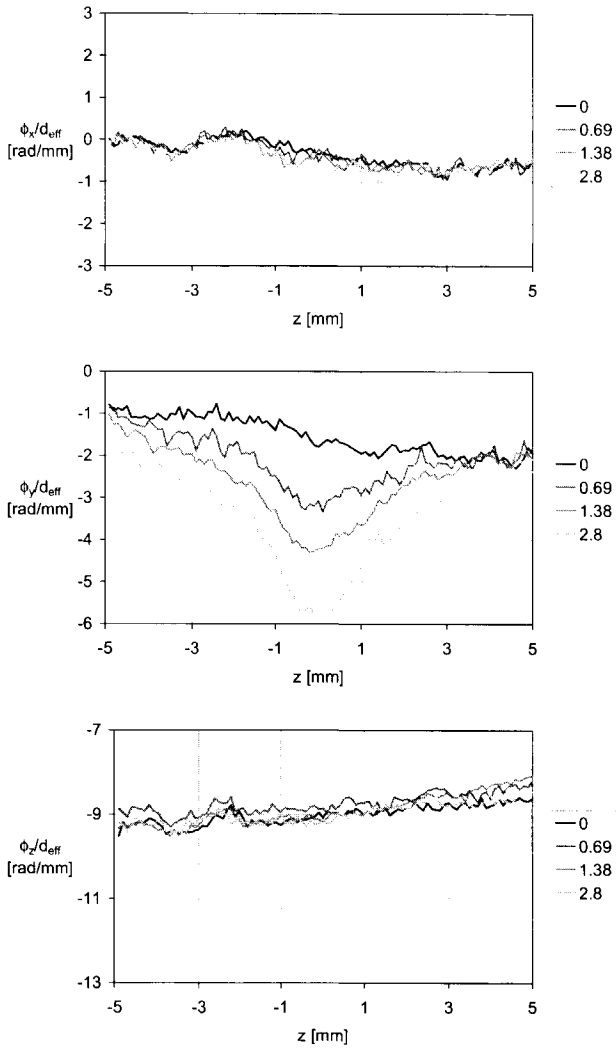


Figure 3A.7: Magnetization in the x, y and z direction in the shear experiment with a consolidation of 15.8 kPa.

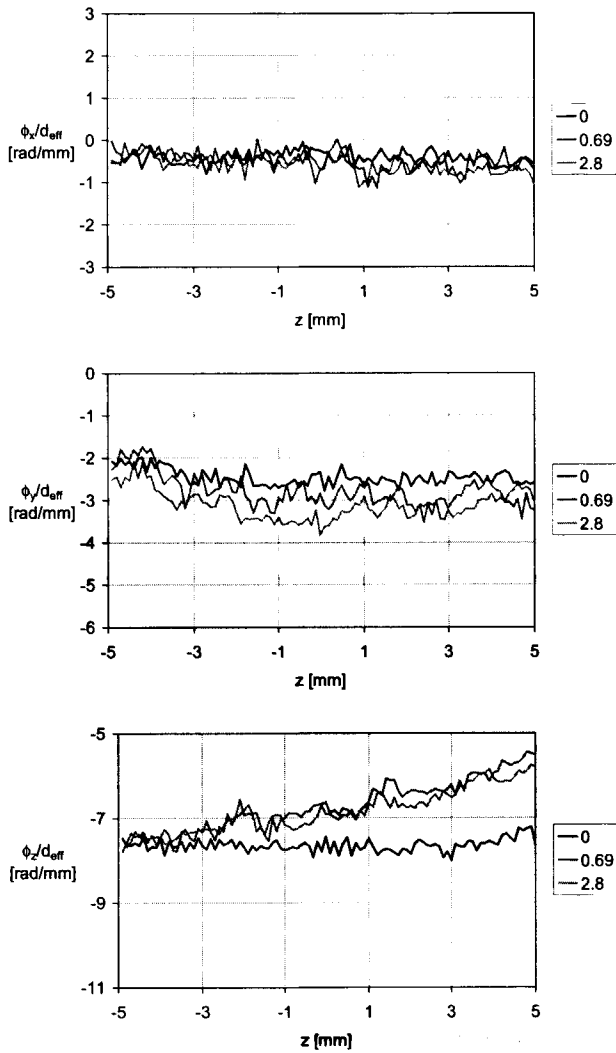


Figure 3A.8: Magnetization in the x, y and z direction in the shear experiment with a consolidation of 22.8 kPa.



# Evaluation of the Flexible Wall Biaxial Tester

The Flexible Wall Biaxial Tester is an advanced powder flow tester, that was built by Kraan (1996). In this chapter the Flexible Wall Biaxial Tester will be evaluated and changes to the setup will be introduced. A number of experiments has been performed on standard BCR-limestone to investigate the behavior of powder for different types of consolidation and for steady-state shear. In cooperation with the Institut für Mechanische Verfahrenstechnik of the Technical University of Braunschweig, a comparison is made between the Braunschweig Biaxial Tester and the Flexible Wall Biaxial Tester. Finally, the flow function of BCR-limestone is measured and the influence of the intermediate stress on the flow function will be examined.

## 4.1 Introduction

Since the development of the Jenike Tester many other powder flow testers have been designed. Most of them were made to overcome problems of the Jenike Tester, some were built with the idea of improving the whole Jenike powder flow characterization method and some were needed to be able to measure more specific properties of a powder. In a number of projects it has been tried to compare the results of different testers with each other (Ose et al. 2000, Verlinden 2000 among others) without much success however. Even comparison of the same tester in different laboratories failed in bringing the results closer to each other than 10-15% (Akers, 1991). The reason is always thought to be found in the operator or the test procedure, although there exists a standard procedure for performing Jenike tests (EFCE Working Party on the Mechanics of Particulate Solids, 1989). The existence of all these different testers illustrates the poor knowledge that exists about powder flow behavior.

In the constitutive approach to powder flow a more sophisticated tester is needed. Arthur et al. (1977) were the first to build such a tester specifically for powder flow testing. At the Delft University of Technology the Flexible Wall Biaxial Tester (FWBT) has been built by Kraan (1996). Next to the Postec Biaxial Tester (Maltby, 1993) and the Braunschweig Biaxial Tester (Harder 1986, Nowak 1993), the FWBT is part of a generation of true biaxial powder flow testers. In this chapter the FWBT is evaluated and modifications to the original setup are presented. The flow function of BCR-limestone is measured in order to compare the FWBT with existing testers. A

more specific comparison is made between the FWBT and the true biaxial tester of the Technical University of Braunschweig.

## 4.2 BCR-limestone

In 1992 a number of powders (quartz, alumina, silicon carbide, titanium dioxide, barium sulfate) has been investigated to find a reference powder for shear testing (Akers, 1992). This project produced certified BCR-limestone (CRM 116) and its flow function. The flow properties of this cohesive grinded limestone proved to be the less dependent on temperature and humidity (figure 4.1) than other powders that were tested.

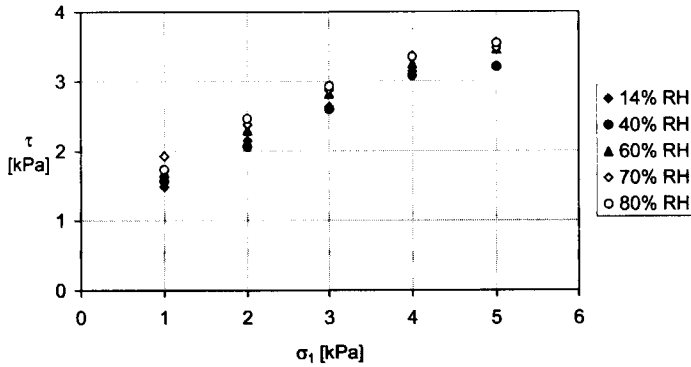


Figure 4.1: Humidity sensitivity of BCR-limestone (Akers, 1992).

Also the time dependent behavior of the BCR-limestone has been tested by measuring the time consolidation effect on the flow function (figure 4.2).

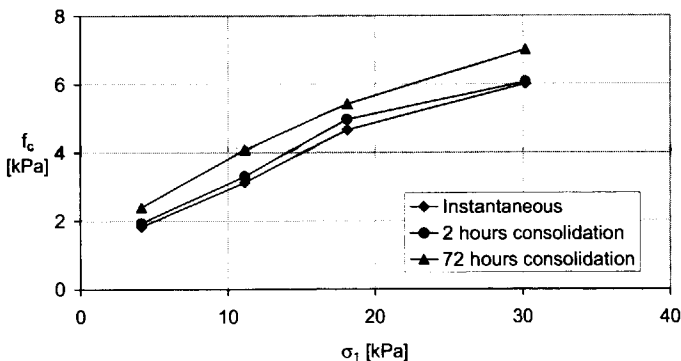


Figure 4.2: Time consolidation of BCR-limestone (Akers, 1992).

The mean particle diameter of BCR-limestone is  $4.0 \mu\text{m}$  (Akers, 1992) which has been verified in chapter 3. This powder will be used as the standard powder in this thesis unless mentioned otherwise.

### 4.3 The Flexible Wall Biaxial Tester

In this paragraph the FWBT will be introduced and its principles and assumptions will be explained. A detailed description of this tester is given by Kraan (1996).

#### 4.3.1 Setup

The Flexible Wall Biaxial Tester has been developed by Kraan (1996) with the main idea being that the axes of the tester are the principal axes. This means that normal stresses or normal strains can be applied without shear components. Stress can be applied by four stress controllers that pressurize four balloons that form the side walls of the sample holder. The resolution of the stress controllers is 0.0244 kPa and the accuracy 0.1 kPa. Strains are applied by moving the side walls with stepper motors (figure 4.3). The resolution of the stepper motors is 0.16  $\mu\text{m}$ , the accuracy is in the same order. The top and bottom of the sample are covered by membranes as well, but these are backed by metal plates. The stress in the vertical direction is measured on the top lid by means of a force transducer.

The height of the sample holder is fixed at 80 mm, the minimum size of the sample volume is 75·75·80 mm<sup>3</sup> and the maximum size is 135·135·80 mm<sup>3</sup>. The control and the data acquisition of the system are completely automated.

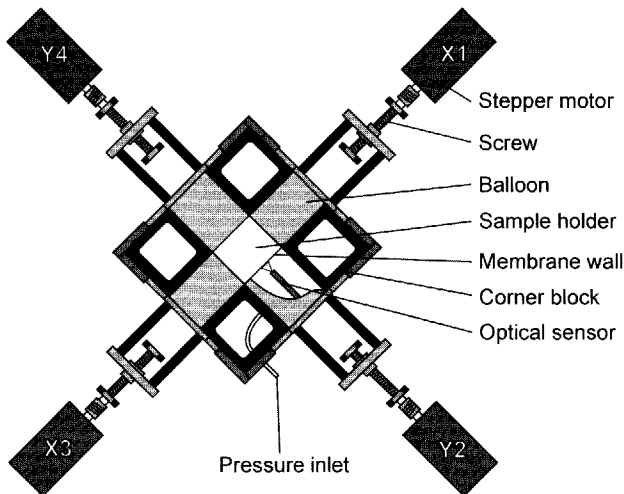


Figure 4.3: Schematic view of the Flexible Wall Biaxial Tester (without top lid).

Flexible membrane walls are used in the FWBT to make both a stress and a strain controlled mode possible. Therefore, these walls are specially constructed as cubical balloons of which all sides are constrained except the side that forms a wall of the sample holder (figure 4.4). Because the membrane wall is not backed by a rigid plate, the membrane can bow inwards and outwards. The membrane face has to be flat, otherwise shear stresses or strains are applied to the sample. Therefore, the membrane deformation has to be monitored. This is done by optical sensors inside the balloons

(figure 4.4). They measure the distance between the membrane face and the sensor itself. This distance is calibrated before each experiment with flat membranes. The deviation of the position of the membrane from the flat position is called the membrane deformation ( $\Delta$ ). The resolution of the optical sensors is  $1.2 \mu\text{m}$ , the accuracy is of the same order.

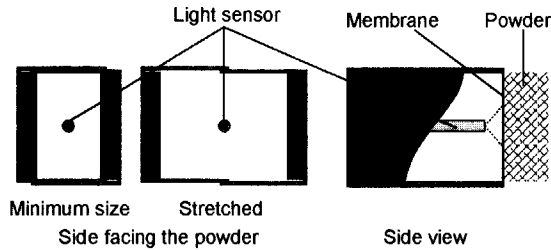


Figure 4.4: Schematic view of the membrane configuration.

The top and bottom of the sample are covered with membranes as well. These flat membranes are fixed on the outer corners of the body of the tester. They are constructed with fibers inside the parts that should not deform so that only the part covering the sample deforms together with the sample (figure 4.5). Because these membranes are difficult to make, the top and bottom membranes have later been reduced in size so that they only cover the powder sample and no internal fibers are needed. They are fixed on the inner edges of the rigid corner blocks. Behind these top and bottom membranes there is a rigid metal plate: the table on the bottom and a removable lid on the top. The friction between the membrane and the metal wall is reduced to a minimum by using a dry teflon lubricant. The wall friction in the FWBT will be discussed in paragraph 4.3.7.

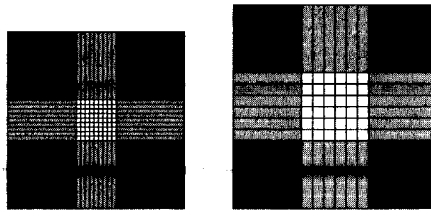


Figure 4.5: Configuration and stretching of the top and bottom membrane. Only the square in the middle covers the sample.

The membranes are manufactured from liquid latex. The procedure to do this is described by Kraan (1996) and more details on the making of rubber membranes are given by Menzies et al. (1972). The membranes that are produced according to this procedure are transparent which is troublesome with respect to the reference value for the membrane deformations. Small amounts of titanium dioxide have been added to the liquid latex in order to produce opaque membranes.

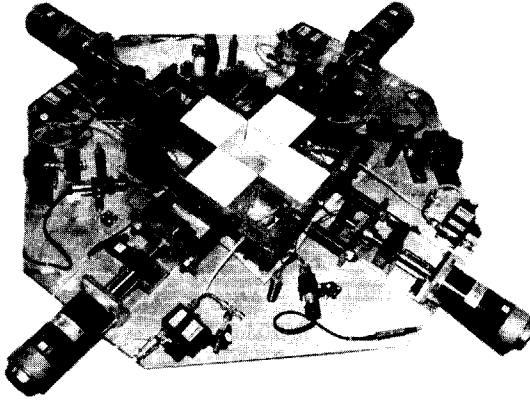


Figure 4.6: Flexible Wall Biaxial Tester (without top membrane and lid).

### 4.3.2 Definitions for the FWBT

The positions of the walls in the FWBT are defined relative to the center point of the largest possible volume (figure 4.7). In the FWBT this initial center point does not have to stay the middle of the sample volume because the walls can move individually. In the strain controlled mode the setpoint positions for the motors in each step are calculated from the input strains for each wall.

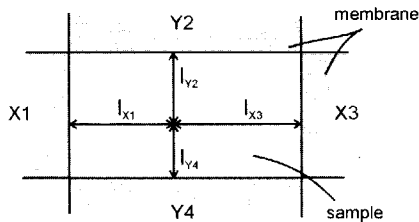


Figure 4.7: Definition of motor positions in the Flexible Wall Biaxial Tester.

The relative strain for a wall in the FWBT is defined as follows:

$$\varepsilon_i = \frac{l_{i,0} - l_i}{l_{i,0}} \quad (4.1)$$

for  $i = X1, Y2, X3$  and  $Y4$ . For the reference value of the length the begin position of the wall of the strain step is chosen. Since the motor positions are known, the total strain for the  $x$  and  $y$  direction can be calculated. The height of the sample is fixed. In some experiments the volume is kept constant in a certain step of the total strain path. This is done by controlling the strain path for one direction and calculate the strain path in the other direction at each moment from the constant volume restraint. An additional requirement in the application of a part of the strain path may be that one or two walls do not take part in the application of strain, while the volume of the

sample remains constant. In this case one wall is chosen to apply the input strain step while the remaining walls adapt to keep the volume constant.

The input strain rate is always the maximum rate with which the strain is applied by the motors. Delays occur when the membrane deformations are not within the allowed limit. In that case, the membrane deformations are corrected before any further strain is applied. The strain rate is applied to all four walls and is defined by:

$$\dot{\epsilon} = \frac{\epsilon_i}{\Delta t} \quad (4.2)$$

The walls have been moved with very small steps ( $0.16 \mu\text{m}$ ) and for each step the timestep ( $\Delta t$ ) is calculated with equation 4.2. The control program waits until time  $\Delta t$  is passed before the next small step is taken.

### 4.3.3 Stress and strain control

The FWBT can function in a strain or a stress controlled mode due to its flexible walls. By pressurizing the balloons in the tester a stress can be applied to the sample. The corresponding membrane deformation is then corrected by moving the membrane wall with the stepper motor. This is the stress controlled operation (left side in figure 4.8). In a strain controlled operation strain is applied by moving the membrane wall with the stepper motor. The resulting membrane deformation is corrected by pressurizing or depressurizing the balloon (right side in figure 4.8). The membranes are defined to be flat when the absolute deformation is smaller than  $10 \mu\text{m}$  for all experiments.

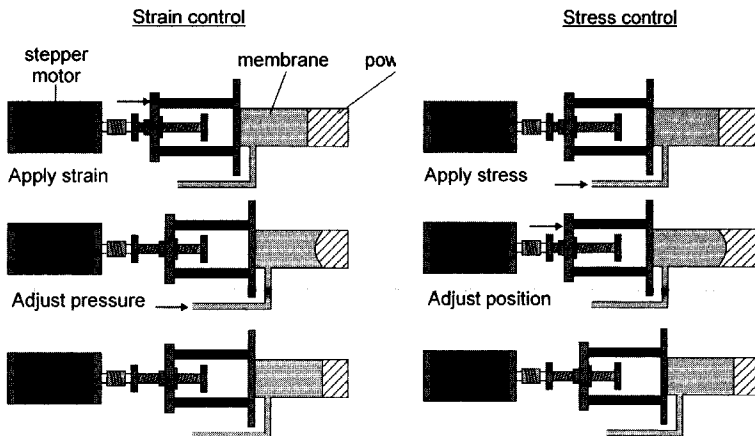


Figure 4.8: Example of the principle of stress and strain control operation in the Flexible Wall Biaxial Tester.

In principle there is no difference between a stress or strain controlled operation for a powder. An applied stress path leads to a strain path that, when it is exactly copied and is applied to the same original sample reproduces the same stress path. However, some operations are typically stress or strain controlled, like the determination of the unconfined yield strength for which one stress should be kept zero. In a true biaxial

tester with rigid walls one can only operate in a stress controlled mode by use of a feedback loop.

#### **4.3.4 Control program and preparation of an experiment**

A detailed report on the hardware components and on the programming software Cyrano can be found in Kraan (1996). Here a brief description of the control program and the preparation of an experiment is given.

The software control program is split into a two parts: one for the stress controlled operation and one for the strain controlled operation. Before one of these modes is chosen, a number of steps has to be taken to prepare the tester and the sample. Firstly, the position of the membrane walls is calibrated by moving them to the maximum position and measuring the x and y length of the sample volume. These are the reference values for the wall positions and they are fed in the computer. Then the walls are moved to the starting position forming the initial volume of the sample. In this position the reference values for the membranes deformations are determined. When transparent membranes were used, the reference has been determined by using white paper to cover the membranes. Without this paper, the reference values would be too low after the tester is filled with white powder. For the opaque membranes the reference value could be determined without the paper.

The next step in the setup of the tester is the calibration of the membranes with respect to the control and monitor pressure values. The pressure controller hardware functioned with two values for the pressure. One as an input (control variable) to the controller and another as output (monitor variable). Both variables have an offset value that is calibrated before each experiment. Now the tester is ready to be filled (paragraph 4.3.5).

When the tester is filled and the top membrane and the lid have been placed, the choice between a stress or strain controlled operation has to be made. The control path is given into the computer and the experiment starts. No user intervention is needed during the experiment.

The strain control program moves the walls to positions that are defined by the user. A special option exists for the steps in which the volume has to be kept constant (e.g. for steady-state shear). The control program uses only the strain path of one direction and calculates the positions of the other two walls at each time step. Another option makes it possible to keep the volume of the sample constant while one or two walls do not take part in the strain path. In this case only the strain path of one wall is used, and the positions of the other walls are calculated for each time step from the constant volume constraint.

Next to the strain path, the strain rate is an input to the control program. This value is the maximum rate with which the walls can move. The movement can be slower if the membrane deformations are not within the allowed limit. The deformations will be corrected before another strain step is taken. For strain controlled experiments this correction is relatively fast because the stress controllers can change the pressure in the membranes very quickly.

The stress control program increases the pressure in the balloons stepwise to the desired value. After each step the deformation of the membranes is corrected by moving the membrane walls in the correct direction. Only after these deformations are within limit, the next step will be taken. In the stress controlled operation, the strain rate is also used as input instead of the stress rate. In principle the correction of the membrane deformation could be quick if the walls could move fast. However, it appeared a difficult task to keep the powder in control with fast moving walls. Therefore, it was chosen to define a strain rate in the stress controlled operation. This makes a stress controlled experiment slower than a strain controlled experiment.

#### 4.3.5 Filling procedure

Two filling procedures have been used for the experiments in this thesis. The first method is equal to the procedure of Kraan (1996) and consists of filling in layers. After each layer the powder was pushed on mildly to remove large cavities. This caused hardly any compaction of the powder but made the bulk density homogeneous over the height. The second method consisted of filling the whole sample volume with loose powder after which a consolidation weight of 0.74 kPa has been applied for exactly 1 minute. This also made the bulk density homogeneous over  $z$  as shown in figure 4.9. In both filling procedures the powder is tapped through a sieve to destroy lumps.

The powder height after filling is 80 mm, but did not always touch the stress transducer in the lid. Therefore, the stress in the  $z$  direction sometimes starts to increase a little later than the stresses in  $x$  and  $y$ -direction.

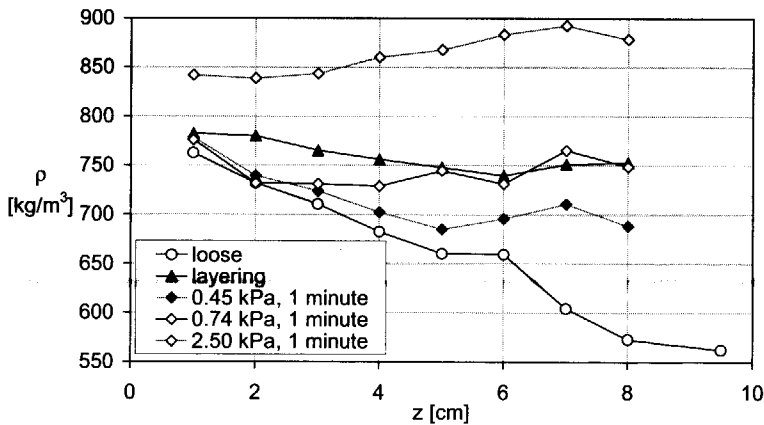


Figure 4.9: Bulk density profile over the height of the sample for different filling methods: loose filling; filling with layers which are mildly compacted and filling with a subsequent consolidation in  $z$  direction.

#### 4.3.6 Calibration of the membranes

The membranes make stress and strain control possible, because the application of stress and strain is uncoupled. However, the membrane deformations are restricted



within a chosen limit. The light sensor inside the membrane makes the monitoring of the deformation possible by measuring the distance between the sensor and the membrane face. The light sensor measures only at one spot on the membrane. Two actions could influence the distance that is measured: the stretching of the membrane and the movement of the sensor relative to the membrane.

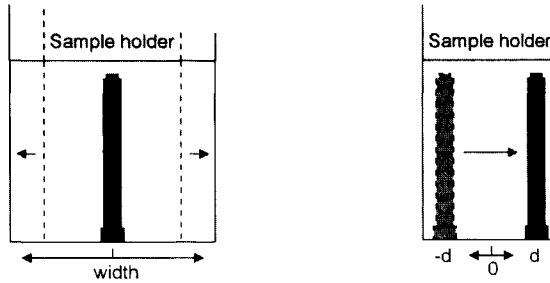


Figure 4.10: Stretching of a membrane (left) and movement of the light sensor relative to the membrane face (right).

The stretching of the membranes is pictured in figure 4.10 (left side). The thickness of the membrane wall is changing by the stretching and this could influence the amount of reflected light. In figure 4.11 the apparent deformation of the membrane is given when the membranes are stretched from their smallest size to their largest size. The reference value for the deformation is determined at a membrane width of 115 mm.

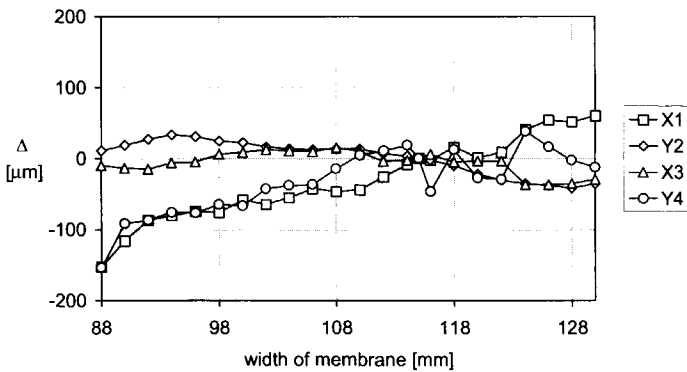


Figure 4.11: Signal of the light sensors during the stretching of the membranes.

The membrane reference values could also be influenced by the relative movement of the light sensor to the membrane face (figure 4.10 right side). The apparent deformation of this action is shown in figure 4.12.

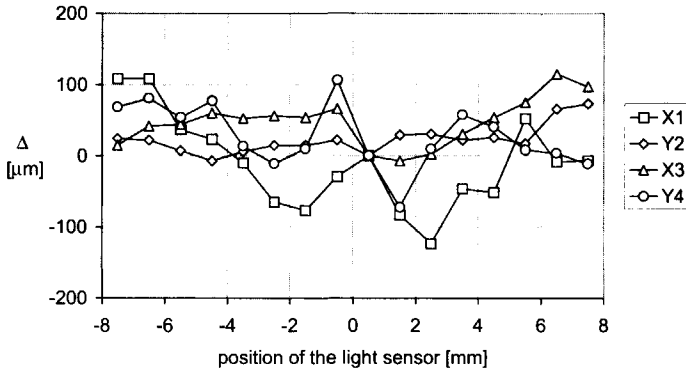


Figure 4.12: The apparent deformation when the position of the light sensor changes relative to the membrane face.

The apparent deformation as measured in figures 4.11 and 4.12 is maximally  $100 \mu\text{m}$  per effect. However, these measurements have been performed without powder in the tester. It is believed that white powder, as BCR-limestone is, decreases the apparent deformation for transparent membranes, because the signal depends more on the powder than on the membrane.

To evaluate the influence of these membrane deformations, an experiment has been performed with a deliberate membrane deformation of  $200 \mu\text{m}$  in all membranes. The results of this experiment do not deviate from the same experiment without the deliberate membrane deformation. It is therefore expected that the registered apparent deformations in figures 4.11 and 4.12 do not influence the results of the FWBT.

### 4.3.7 Wall friction

In paragraph 4.3.1 the special configuration of the membranes has been introduced, which makes it possible to operate the FWBT in a stress and a strain controlled mode. The second reason for the use of the membranes is to avoid shear stresses between the powder sample and the wall. The principle of this construction is illustrated in figure 4.13.

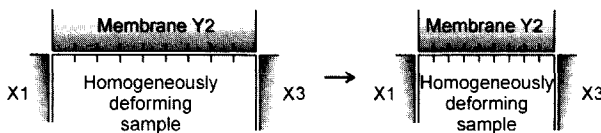


Figure 4.13: Principle of membrane walls to avoid wall friction: no slip occurs between the powder and the prestretched membrane wall when the powder sample deforms homogeneously.

The membranes are prestretched and will deform homogeneously. If the sample deforms homogeneously as well, a point on the membrane will not change its position

relative to a neighboring point in the powder. For that reason no slip or shear stress or strain can occur between the membrane and the sample. This idea is used in many true biaxial testers.

The principle of figure 4.13 also holds for the top and bottom membrane. However, a lubricant is needed between the membranes and the metal backing plates. In figure 4.14 the influence of the lubricant on the wall friction is shown by a strain controlled experiment in which one wall moves inwards while all other walls do not move. This is a uniaxial consolidation. The experiment is performed without lubricant (figure 4.14 left) and with the dry teflon lubricant (figure 4.14 right). The difference that occurs between the normal stress on wall X1 and X3 depends on the lubricant. However, even with the lubricant a small stress difference occurs. It is concluded that the configuration of the membranes in the FWBT is such that when the sample deforms homogeneously no shear stresses or strains appear.

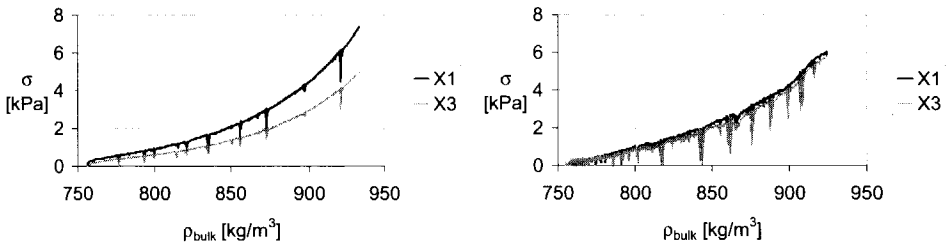


Figure 4.14: Uniaxial consolidation with one wall: without lubricant (left); with dry teflon lubricant (right).

## 4.4 Consolidation experiments

The consolidation of powder is defined as the reduction of the volume of the sample. Consolidation of a sample brings the individual particles closer to each other, increases the number of contacts and increases the cohesion in the sample by pressing particles together. The state of compactness that a powder reaches, has a major influence on the flow property of the sample. Therefore, a consolidation is often the first step in investigation of powder flow. In this paragraph three types of consolidation experiments will be investigated.

### 4.4.1 Introduction

If the bulk density of a granular material is gradually increased by reducing the volume, the resulting stresses will increase. The relation for a perfect isotropic consolidation between the bulk density (or porosity) and the stresses is given in the Hvorslev diagram (figure 2.6) by the normal consolidation line (Roscoe et al. 1958):

$$\sigma = \exp\left(\frac{\epsilon_a - \epsilon}{\kappa}\right) \quad (4.3)$$

where  $\varepsilon_a$  and  $\kappa$  are constants. The surface between the normal consolidation line and the critical state line defines consolidation with a deviatoric stress. According to this diagram no consolidation line ( $\sigma_m$  versus  $\rho_{\text{bulk}}$ ) can be higher than the line for isotropic consolidation i.e. isotropic triaxial volume reduction. Fedá (1982) and Hicher (1998) have shown in soil mechanics that the position of a consolidation line depends on the type of consolidation and therefore on the deviatoric stress. The higher the deviatoric stress, the lower the consolidation line is situated. A deviatoric stress helps to densify the powder, as also Hicher (1998) remarked, probably because the re-arrangement of the particles is facilitated. At equal mean stresses, the volumetric strain of the sample is therefore larger for uniaxial compression than for hydrostatic loading.

For cohesive powder Nowak (1993) measured that the position of the consolidation line, which he defines as the mean stress ( $\sigma_m$ ) versus the bulk density, also depends on the consolidation type. A biaxial consolidation resulted in a higher consolidation line than a uniaxial consolidation.

The consolidation of particulate materials is largely a consequence of the irreversible displacements of their particles. Hence the structure of particulate materials varies and the resulting stress characterizes the structural changes. This induced structure has a large effect on the behavior of the powder and therefore, it is important to know what type of consolidation the powder has undergone. In direct shear testers like the Jenike Tester, Peschl Cell or the Schulze Ring Shear Tester the applied consolidation load is uniaxial. A biaxial consolidation, as often used in the flow function procedure (see paragraph 4.7.1), can be applied with biaxial testers. The difference between biaxial and uniaxial consolidation is subject of the following sections.

#### 4.4.2 Biaxial consolidation

The biaxial consolidation experiment is performed in both the strain controlled and the stress controlled mode. In the strain controlled mode, the sample size is decreased in x and y direction with the same strain and strain rate, resulting in normal stresses on the walls as shown in figure 4.15.

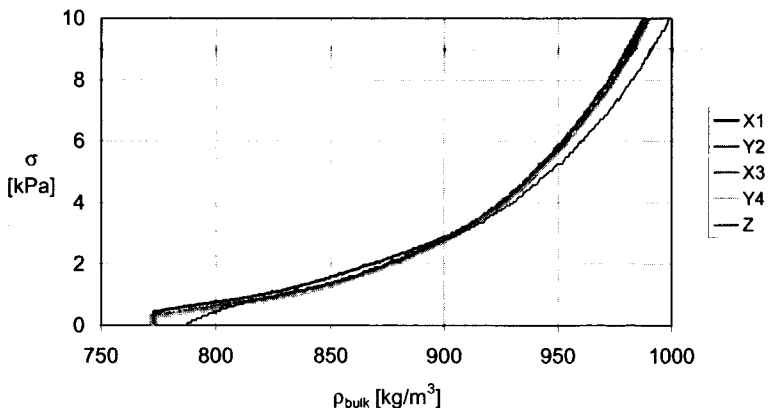


Figure 4.15: Biaxial consolidation experiment in strain controlled mode .

Because the applied strain is isotropic with respect to the x and y direction, the stresses in these directions are equal. The stress at the top of the sample (z-direction) is normally lower. This result is shown by other researchers (Nowak 1993, Maltby 1993 and Kraan 1996) and is due to the fact that it is difficult to fill the tester precisely up to the top lid.

In the stress controlled consolidation experiments, the normal stress on the sample is slowly increased to a predefined value. The resulting strain is recorded and the stress path as a function of the bulk density is similar to the strain controlled experiment in figure 4.15.

Quite a number of consolidations has been performed for both control types (figures 4.16 and 4.17).

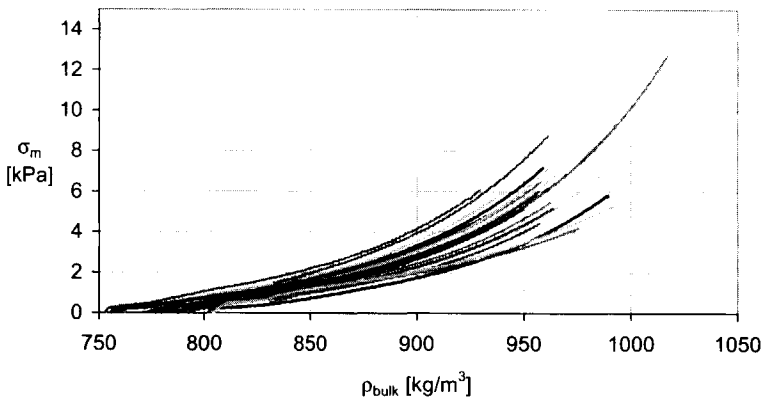


Figure 4.16: Biaxial consolidation experiments in strain controlled mode.

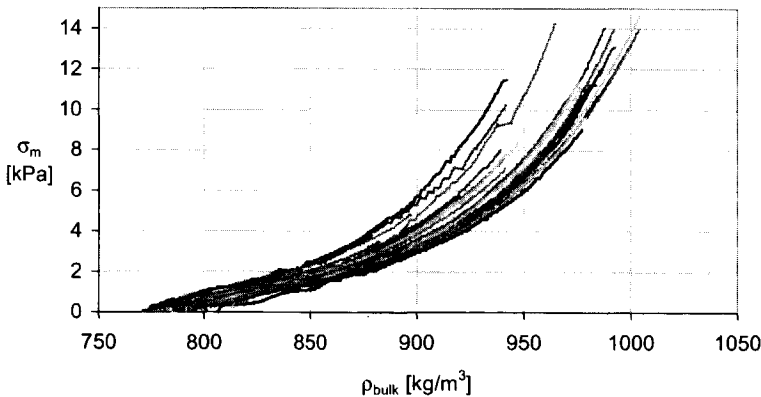


Figure 4.17: Biaxial consolidation experiments in stress controlled mode.

It is remarkable that the stress controlled operation produces stronger increasing consolidation curves than the strain controlled operation. The stress controlled

experiments are performed with a resulting strain rate that is three to four times lower than for the strain controlled experiments. This is caused by the way the control program works (see paragraph 4.3.4). The influence of the rate of consolidation will be investigated in paragraph 4.4.5.

The spread of the consolidation curves of figures 4.16 and 4.17 is quite large. This can be explained by the precision of the measurements. The error introduced by the stress controller will be equal for all experiments, but the error in the measurement of the bulk density changes per experiment and depends on two factors: the measurement of the sample mass after each experiment and the calibration of the motor positions. The error in the sample mass determination is estimated to be  $\pm 0.5\%$  of the total mass. The calibration of the motor positions is done by hand and the introduced error is estimated at 500 to 1000  $\mu\text{m}$  of the measured  $x$ ,  $y$  and  $z$  length. In figure 4.18 the total inaccuracy in the bulk density is given for a typical consolidation experiment. The consolidation curves shift on the horizontal axis causing large deviations in the stresses measured at a certain bulk density.

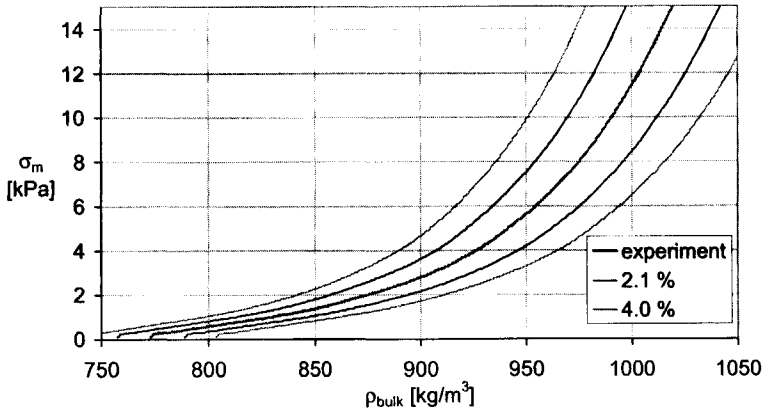


Figure 4.18: Influence of measurement errors in the bulk density on the consolidation line:  $\rho_{\text{bulk}} \pm 2.1\%$  (mass  $\pm 3.7$  g and  $l_x, l_y, l_z \pm 500$   $\mu\text{m}$ ) and  $\rho_{\text{bulk}} \pm 4.0\%$  (mass  $\pm 6.0$  g and  $l_x, l_y, l_z \pm 1000$   $\mu\text{m}$ ).

Comparison of figures 4.16 and 4.17 with figure 4.18 shows that the wide spread of the biaxial consolidation lines can be explained by the measurement error in the bulk density.

In order to see if the consolidation curves have the same shape, the logarithmic mean stress is presented versus the bulk density according to the equation 4.3 proposed by Roscoe et al. (1958) in figure 4.19. The Roscoe relation seems to hold: after an initial curvature, the consolidation lines are straight. The lines are mostly parallel to each other with a few exceptions. This proves that the shape of the consolidation curves is the same for most of the experiments and therefore the mechanism for the consolidation is the same as well.

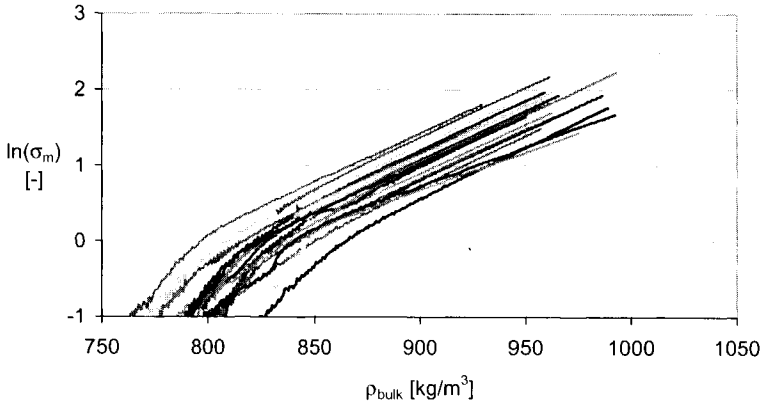


Figure 4.19: Biaxial consolidation experiments in strain controlled mode presented according to equation 4.3.

From figure 4.19 it also appears that a higher initial bulk density produces a lower consolidation curve. However, as stated before, the precision in the measurement of the bulk density is the reason for this effect.

The relation between the vertical normal stress and the major consolidation stress reaches a certain constant value (figure 4.20). It takes large strain deformations (> 15%) before this value is reached.

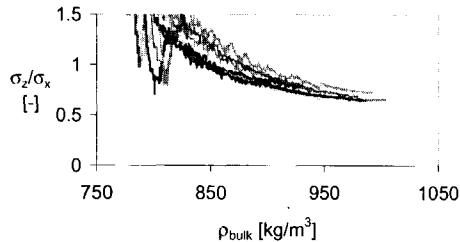


Figure 4.20: Relation between  $\sigma_z$  and  $\sigma_x$  for biaxial experiments.

#### 4.4.3 Uniaxial consolidation with two moving walls

The second type of consolidation experiment that is performed with the FWBT, is a uniaxial consolidation. This type of consolidation was operated only in a strain controlled mode. In the FWBT there are two possibilities to apply uniaxial strain: by moving one wall or by moving two opposite walls. The former is treated in the next paragraph. The result of a typical consolidation experiment with two moving walls is given in figure 4.21.

The stresses on the X1 and X3 wall are the highest, since these are the walls that apply the strain. The stresses on the Y and Z walls are lower because no direct strain is applied on the powder by these walls. The Z stress shows again a delayed reaction because of the too low filling height.

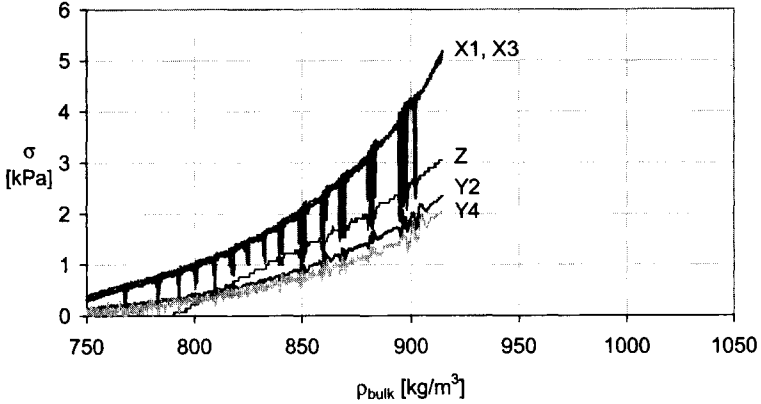


Figure 4.21: Uniaxial experiment with strain applied by the X1 and X3 walls.

The spread in a number of uniaxial consolidations in figure 4.22 is due to the precision in the measurement of the bulk density as was shown for the biaxial consolidation (figure 4.18). Some of the uniaxial experiments (figure 4.22) show strong stress fluctuations. These are absent in the biaxial consolidation experiments. It is remarkable that all stresses decrease during a fluctuation and not only the stresses in the direction that is being deformed. This means that the powder collapses probably due to the deviatoric strain.

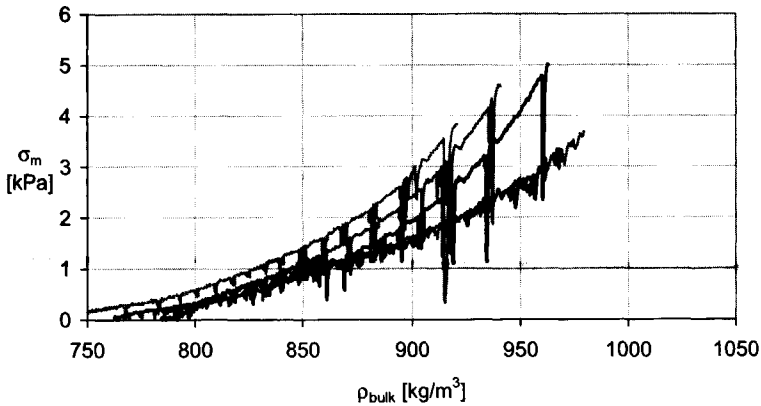


Figure 4.22: Uniaxial experiments with two walls moving inwards.

In figure 4.23 the uniaxial experiments are presented according to relation 4.3. The consolidation lines also form a straight line after an initial stronger increase of the stresses. This curvature takes place over a longer strain than for the biaxial consolidation experiments. This initial effect is probably caused by the change of the initial arrangement of the particles in the powder to the arrangement that forms due to



the applied strain path. This rearrangement is quicker for the biaxial consolidation because the strain is applied from both the  $x$  and  $y$  direction. In the uniaxial consolidation one direction ( $x$ ) applies the strain and the rearrangement of the particles is directed from that side. The perpendicular direction ( $y$ ) is passive and is only influenced by the rearrangement of the straining direction ( $x$ ).

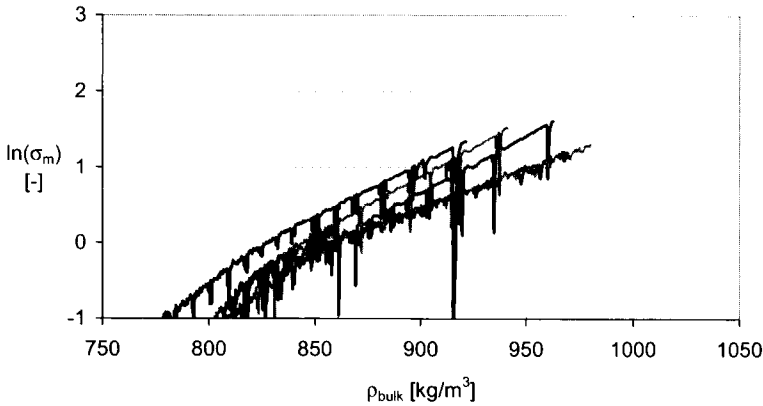


Figure 4.23: Uniaxial experiments with two walls moving inwards presented according to equation 4.3.

In order to compare the uniaxial and the biaxial consolidation, the curves are corrected for their initial bulk density (figure 4.24). The results are evident: the uniaxial volume decrease produces lower stresses for the same bulk density increase. This outcome is conform the results of Nowak (1993) and the Roscoe consolidation surface (figure 2.7).

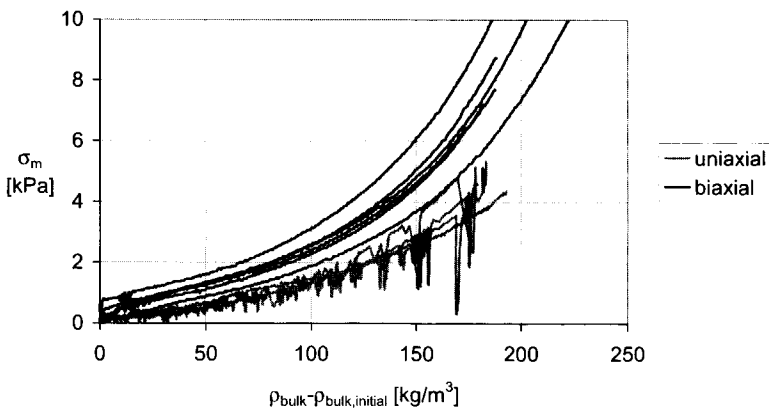


Figure 4.24: Biaxial and uniaxial consolidation curves corrected for the initial bulk density.

The reason for the lower consolidation curves for the uniaxial consolidation is probably the easier rearrangement of the particles due to the deviatoric stress and strain. These cause larger shear components which give rise to more rotation of the particles, as seen in chapter 3, with respect to the rotation of particles due to a biaxial consolidation.

However, when the consolidation lines are presented as the major principal stress versus the bulk density, the difference between the uniaxial and biaxial consolidation is less pronounced (figure 4.25).

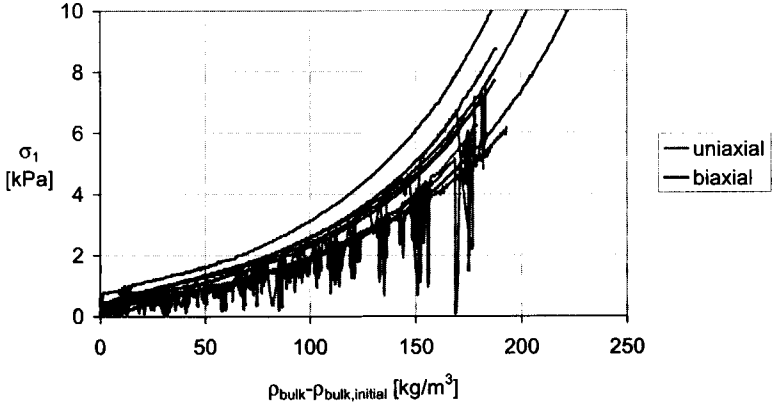


Figure 4.25: Biaxial and uniaxial consolidation curves: major principal stress versus corrected bulk density.

This difference in the presentation of the consolidation curves has been found by Feise (1996) as well. The major principal consolidation stress seems independent of the type of consolidation. However, the experiments of figure 4.25 are not precise enough to show that. It is expected that the major principal consolidation stress differs, because the strain applied in the direction of the major principal stress is different for each type of consolidation.

The relation between the major and minor principal stress and between the major and intermediate principal stress is given in figure 4.26.

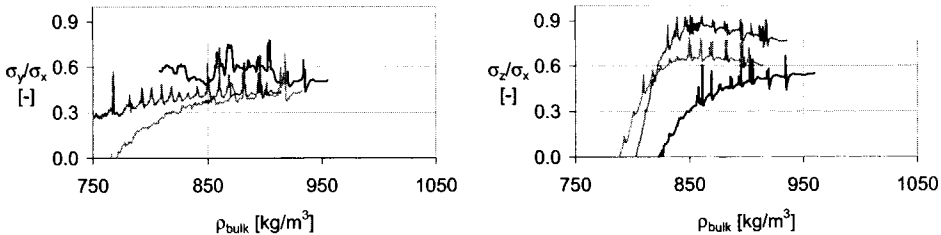


Figure 4.26: Relation between  $\sigma_y$  and  $\sigma_x$ , and between  $\sigma_z$  and  $\sigma_x$  for three uniaxial experiments with two walls moving inwards (moving average is applied to smooth the curves).

The factor  $\sigma_y/\sigma_x$  for BCR-limestone reaches a constant value of 0.43 - 0.51. It takes quite some strain before the constant value is reached and some of the experiments in figure 4.26 did not reach a constant relation between the stresses after a volumetric strain of 19 %. The factor  $\sigma_z/\sigma_x$  reached a value of 0.55-0.60. Table 4.1 on page 79 contains an overview of these factors for all consolidation experiments.

#### 4.4.4 Uniaxial consolidation with one moving wall

The last type of consolidation is uniaxial from only one side, resembling the consolidation in for example an oedometer. In the FWBT this is done by moving just one wall (X1). If the powder would behave as a perfect continuum, one would expect the stresses on the X1 and X3 wall to be equal. Figure 4.27 shows a typical uniaxial consolidation experiment with one straining wall.

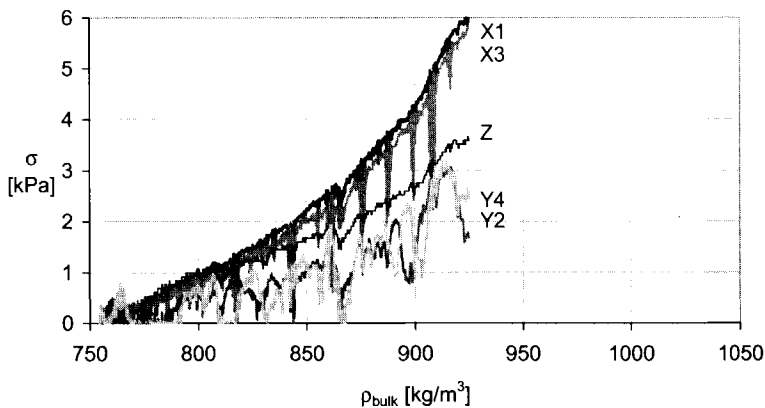


Figure 4.27: Uniaxial experiment with one wall moving inwards.

The stress on the X1 wall is slightly higher than the stress on the X3 wall. In section 4.3.7 it was shown that the side walls in the FWBT cause no shear components on a homogeneously deforming sample. The top and bottom membranes can cause shear components, but these components can be reduced to a minimum by using a lubricant. It is strange that the difference in stress between X1 and X3 remains more or less constant. If the difference was caused by the membranes, it would be expected that the shear stress increases with increasing normal stress (see for example 4.14). Therefore, the difference between the normal stress on the opposite X1 and X3 wall is probably caused by the inhomogeneous behavior of the sample. The bulk density increases differently at different locations in the sample which gives rise to shear stresses between the powder and the membrane walls.

In figure 4.28 the mean stress for three typical uniaxial experiments with one wall are given. The pressure drops in these experiments are less deep compared to the uniaxial experiments with two walls. The reason for this is unknown.

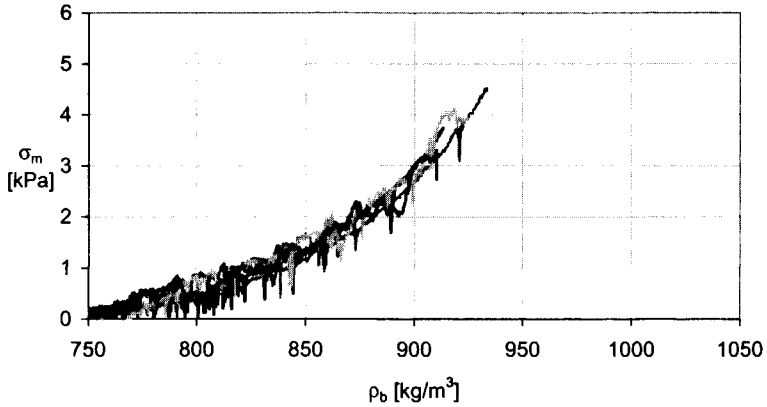


Figure 4.28: A number of uniaxial experiments with one wall moving inwards.

The consolidation curves of the uniaxial consolidation with one wall compare to the biaxial consolidation in the same way as the consolidation lines of the uniaxial consolidation in figure 4.24. Again, the major consolidation stress versus the bulk density does not show the difference in the consolidation curves.

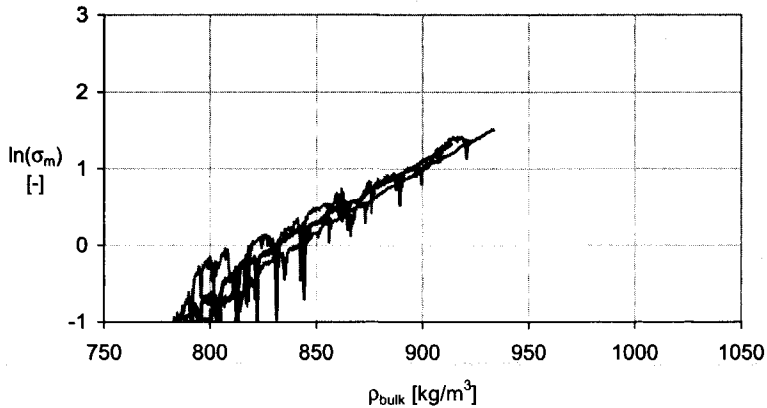


Figure 4.29: Uniaxial experiments with one wall moving inwards according to equation 4.3.

In figure 4.29 the consolidation curves are pictured according to Roscoe's relation (equation 4.3) also showing a stronger initial increase of the stresses after which they form a straight line. These representations (figures 4.19, 4.23, 4.29) show parallel lines with the same inclination for all types of consolidations. This indicates that the mechanism of the rearrangement of the particles is the same in every consolidation.

The relations between the major consolidation stress ( $\sigma_{X1}$  in this case) and the other stresses are presented in figures 4.30. Again it takes quite a large deformation

before the factors  $\sigma_y/\sigma_{x1}$ ,  $\sigma_z/\sigma_{x1}$  and  $\sigma_{x3}/\sigma_{x1}$  approach a certain constant value. This indicates that it takes a large deformation to rearrange the particles from the initial structure caused by the filling to the structure ideal for the type of consolidation.

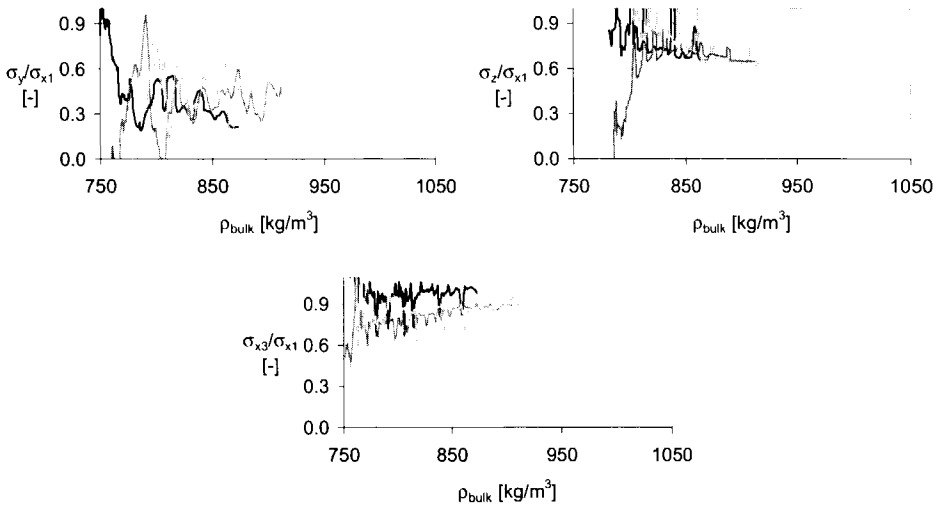


Figure 4.30: The factors  $\sigma_y/\sigma_{x1}$ ,  $\sigma_z/\sigma_{x1}$  and  $\sigma_{x3}/\sigma_{x1}$  for the uniaxial consolidation experiments with one wall moving inwards.

In table 4.1 the constant values of the relations between the principal stresses and the major principal consolidation stress for all types of consolidation experiments are given. It should be remarked that some of these relations did not reach a constant value. The ratios between the major principal stress ( $\sigma_x$ ) and the other two normal stresses ( $\sigma_y$  and  $\sigma_z$ ) are not equal for the uniaxial experiments. For the biaxial consolidation Kraan (1996) found a value of 0.71 for the  $\sigma_z/\sigma_x$  ratio. Nowak (1993) reports a value of 0.58 for the same ratio (table 4.2) in a sample with a height of 35 mm. This difference is probably caused by the height of the sample which is 35 mm in Nowak's experiments and 80 mm in the FWBT experiments. The ratio  $\sigma_y/\sigma_x$  agrees quite well with the results of Nowak.

Table 4.1: Results of the consolidation experiments.

	$\sigma_y/\sigma_x^*$	$\sigma_z/\sigma_x^*$	$\sigma_{x3}/\sigma_{x1}$
biaxial cons.	1.0	0.66 - 0.80	-
uniaxial cons. (2 walls)	0.43 - 0.51	0.55 - 0.60	-
uniaxial cons. (1 wall)	0.30 - 0.55	0.60 - 0.69	0.92-1.00

\* for the uniaxial consolidation with one wall  $\sigma_{x1}$  is used as the denominator

Table 4.2: Literature results for consolidation experiments (Nowak, 1993).

	$\sigma_y/\sigma_x$	$\sigma_z/\sigma_x$
biaxial cons.	1.0	0.58
uniaxial cons. (2 walls)	0.48	0.45

### 4.4.5 Strain rate experiments

The consolidation experiments discussed in the paragraphs above are performed at a constant strain rate of  $1 \cdot 10^{-5} \text{ s}^{-1}$ . In this paragraph the influence of the resulting strain rate ranging from  $7 \cdot 10^{-7} \text{ s}^{-1}$  to  $2 \cdot 10^{-5} \text{ s}^{-1}$  on the biaxial consolidation is investigated. The consolidations are performed in stress controlled mode.

Figure 4.31 shows different consolidation curves of the powder as a function of the strain rate. It can be seen that the stresses increase more quickly with the bulk density when the experiment is performed slower. The consolidation experiments of figures 4.16 and 4.17 confirm this conclusion: the stress controlled consolidation is performed with a three to four times lower strain rate which results in steeper consolidation curves. The influence of the strain rate is bigger than the precision with which the bulk density is measured (figure 4.18).

In contrast to this result, experiments performed with the Braunschweig Biaxial Tester (Zetzener et al., 1998) on limestone ( $4.8 \mu\text{m}$ ) did not show a dependency of the consolidation curve on the strain rate. The stresses reached the same value for all strain rates (varying from  $8.3 \cdot 10^{-6} \text{ s}^{-1}$  to  $6.7 \cdot 10^{-5} \text{ s}^{-1}$ ). However, the relaxation that followed on the consolidation step did depend on the strain rate of the consolidation path. A higher strain rate resulted in a faster relaxation.

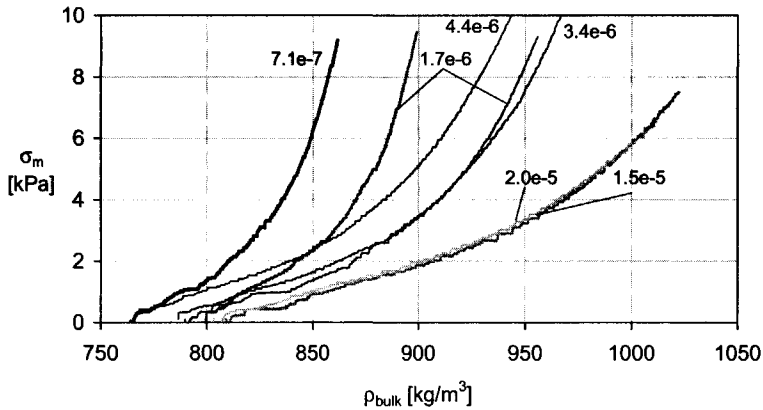


Figure 4.31: Biaxial consolidation in a stress controlled experiment for different strain rates.

Maltby (1993) reports a clear decrease of the unconfined yield strength of limestone with an increase in the strain rate indicating the same trend as in figure 4.31. On a larger scale of the strain rate, Cristescu (1988) also showed the same trend.

### 4.4.6 Shear planes after consolidation

After the consolidation experiments were finished, the top lid and top membrane have been removed and the side walls have been moved outwards. The bottom membrane stretches because of the increase of the volume of the tester and this causes the powder sample to break. It is assumed that the sample will break at the weakest spots,

which pick up the positions of the shear planes at the end of the experiment (figure 4.32). This assumption is strengthened by the fact that the cracks go down to the bottom of the sample.

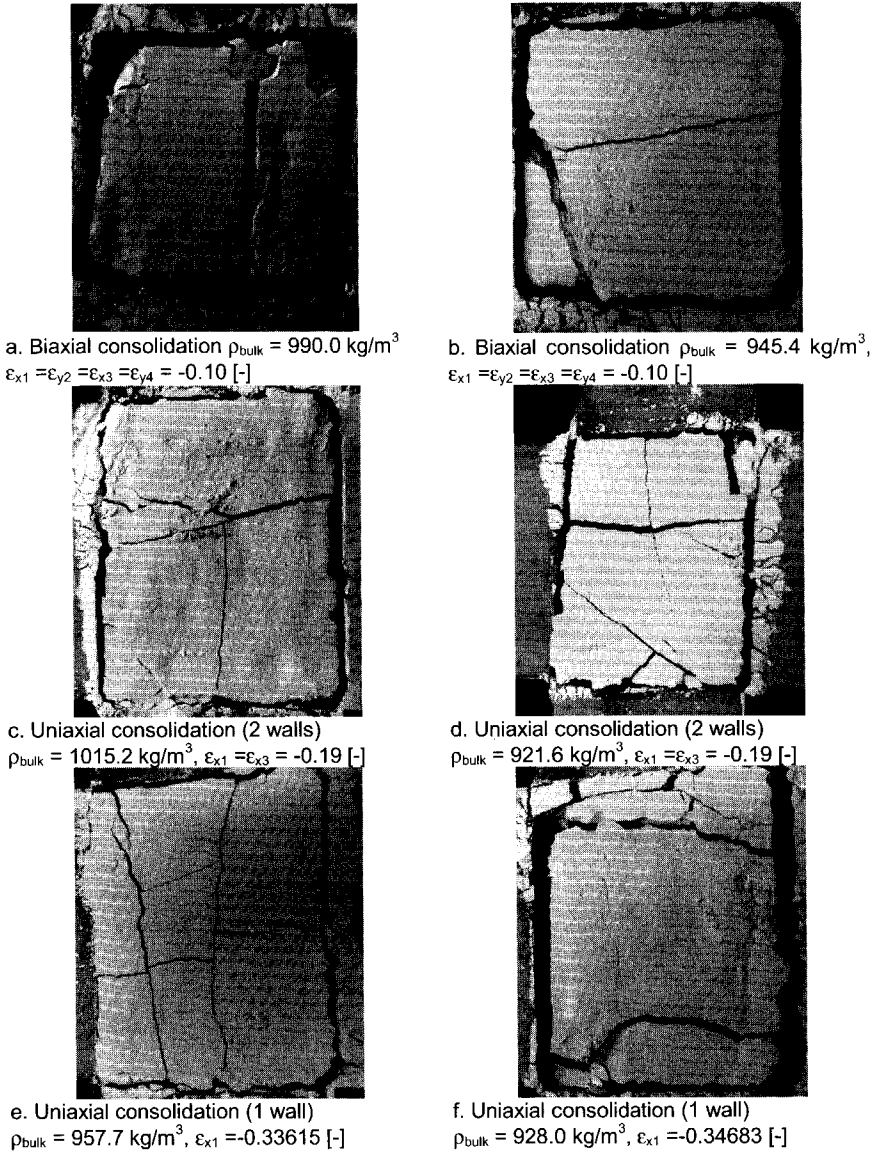


Figure 4.32: Photographs of consolidated samples ( $\epsilon_v = 0.19$ ) after the experiment (wall X1 is on the right; wall Y2 is on the bottom). The top lid has been removed and the X and Y confining walls have been retracted. The photos show the cracks for the different types of consolidation.

The cracks are given in figure 4.32 for the biaxial consolidation, the uniaxial consolidation with two moving walls and the uniaxial consolidation with one moving wall. The pictures given in figure 4.32 are representative for about 30 experiments.

The cracks for all three types of consolidation are more or less parallel to the axes of the FWBT. This indicates that there are no real shear planes in the powder. The cracks in the powder will occur in line with the stretching of the bottom membrane.

## 4.5 Steady-state shear of BCR-limestone

The application of a steady-state shear step, also called the second step of consolidation by Molerus (1975) or preshear step according to Jenike (1961), creates a denser packing in the powder as just a single consolidation with the same normal load.

In the Jenike Tester and similar direct shear testers only one shear plane exists. In the FWBT a number of shear planes is thought to exist, which can freely grow or change direction. However, some kind of steady-state does still exist in the sample as will be shown in the following experiments.

In the Flexible Wall Biaxial Tester the procedure as presented in figure 4.33 is used when the tester is operated in a stress controlled mode. First the sample is biaxially consolidated up to a chosen point ( $A_1, B_1, C_1$ ). From there on, the normal stress in one direction increases and the normal stress in the other direction decreases in such a way that the sum of two remains constant. One can picture this as a growing Mohr circle with a fixed center. At a certain moment the powder cannot withstand the applied stress and will start to yield. For the FWBT this means that the deviatoric stress cannot be increased any further because the powder yields

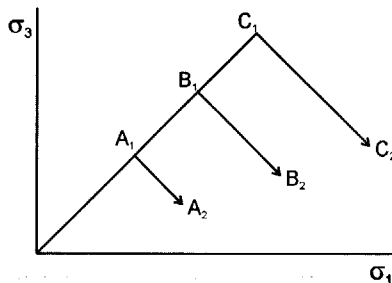


Figure 4.33: Stress path for consolidation up to a chosen point ( $A_1, B_1, C_1$ ) and stress path to reach steady-state shear. The endpoint of the shear path is determined by the powder ( $A_2, B_2, C_2$ ).

Figure 4.34 shows a typical stress controlled consolidation and shear experiment. The volume of the sample becomes constant when steady-state is reached. The positive deformation of the membranes is relatively high in the beginning of the consolidation step. This is allowed because the deformation of the opposite membranes was negative. Correction of the positive deformations by moving these walls inwards will lead to a translation of the whole sample in that direction because the opposite walls are moving in the same direction because of the negative membrane deformation.



Therefore, it was chosen to deny the positive deformations because they are corrected automatically when the stresses increase.

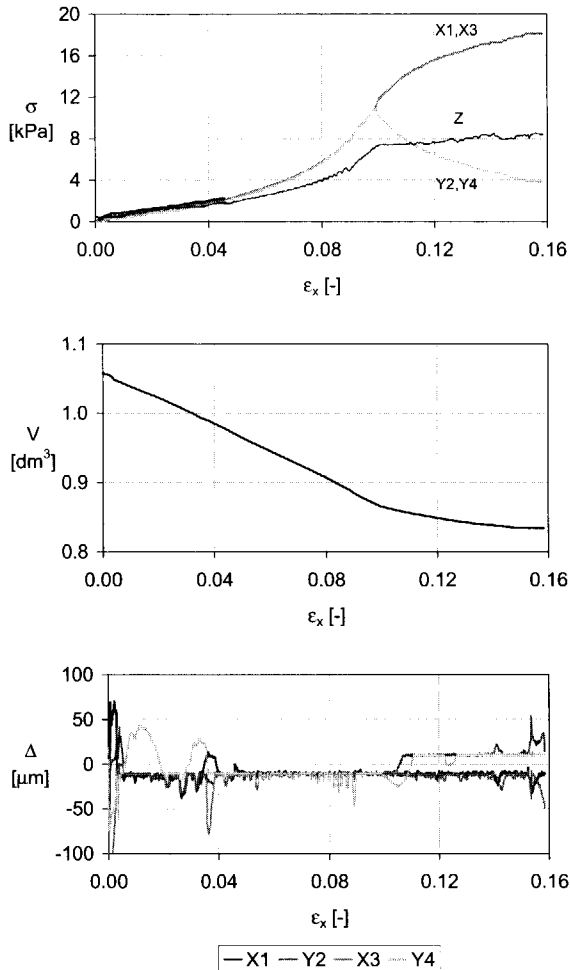


Figure 4.34: Typical stress controlled consolidation and preshear experiment with a consolidation of 11 kPa: stress path (top); volume (middle); membrane deformations (bottom).

Steady-state shear of the BCR-limestone sample can also be reached in a strain controlled mode. The strain path is given in figure 4.35 and is very similar to the stress path of figure 4.33. There is, however, an important difference: the endpoint of the shear path ( $A_2$ ,  $B_2$ ,  $C_2$ ) is not determined by the powder, but is defined by the user. Therefore, the shear is applied for a longer strain than in the stress controlled experiment.

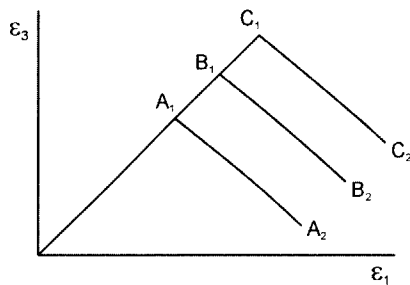


Figure 4.35: Strain path for consolidation up to a chosen point ( $A_1, B_1, C_1$ ) and strain path in which steady-state shear will be reached. The endpoint of the shear path is determined by the user ( $A_2, B_2, C_2$ ).

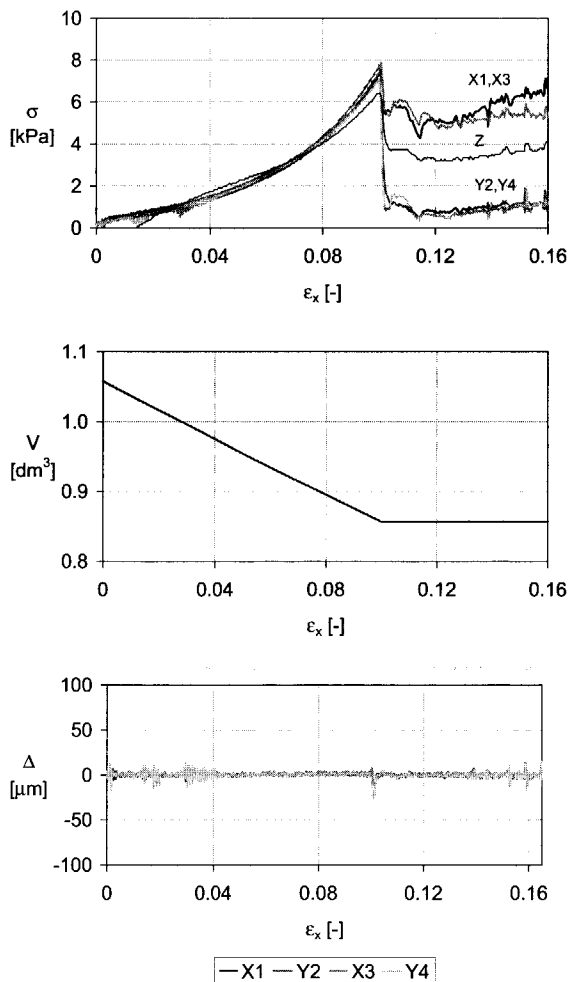


Figure 4.36: Typical strain controlled consolidation and preshear experiment with  $\epsilon_{v,cons} = 10.0\%$  and  $\epsilon_{x,shear} = 7.2\%$ : stress path (top); volume (middle); membrane deformations (bottom).

A typical strain controlled consolidation and shear experiment is given in figure 4.36. The volume is defined by the strain path. The deformations of the membranes are small and within  $10 \mu\text{m}$ , which is the allowed limit. The steady-state stresses in the shear step are determined by the chosen endpoint of the consolidation step. The volume that is reached at that point is the steady-state volume that the powder has to adapt to. The normal stresses do not reach a clear steady-state. They keep fluctuating and in some cases increasing or decreasing. This is typical for all steady-state steps in experiments in the FWBT. The explanation for the fluctuations could be a stick-slip like behavior of the powder during shear. The fact that the powder does not reach a clear steady-state could be caused by a changing pattern of shear planes. The form of the sample can play an important role in this.

The stress in the third direction (the  $z$  direction in the FWBT) is assumed to be intermediate. The results in figures 4.34 and 4.36 show that this is mostly true. In figure 4.37 the steady-state values for the principal stresses are shown. Both the relation between the intermediate and the major principal stress and the relation between the minor and the major principal stress are proportional.

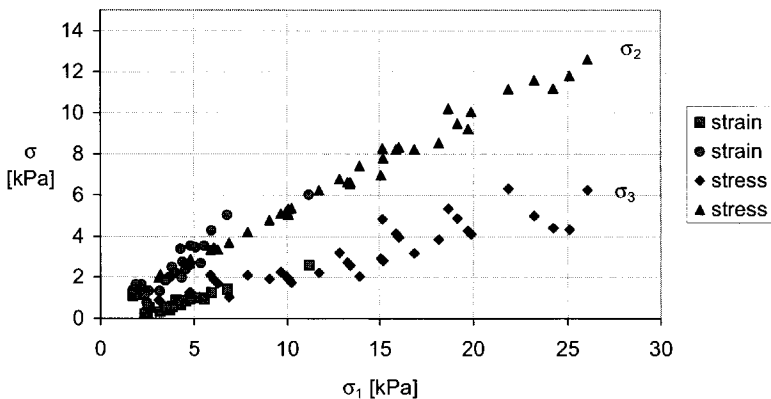


Figure 4.37: Measured minor ( $\sigma_3$ ) and intermediate ( $\sigma_2$ ) principal stress at steady-state preshear in the FWBT. Experiments are performed in both stress and strain controlled mode.

From the above presented steady-state shear experiments, the critical state line can be constructed by using the mean stress (equation 2.7), the deviatoric stress (equation 2.8) and the bulk density (figures 4.38). The relation between the deviatoric and the mean stress is a straight line. The relations between the deviatoric stress and the mean stress with the bulk density is less obvious. This is partly explained by the inaccuracy of the measurement of the bulk density.

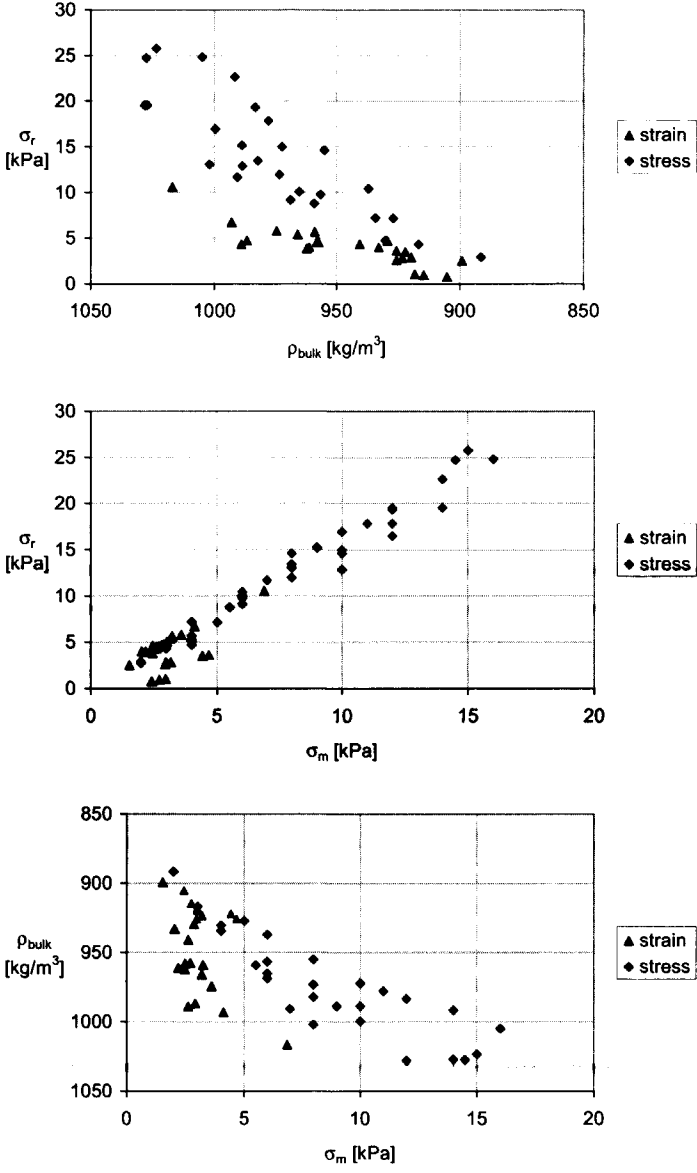


Figure 4.38: The critical state line presented as a function of  $\sigma_m$ ,  $\sigma_r$ , and the bulk density. Measured with stress and strain controlled experiments.

## 4.6 Comparison of the Braunschweig Biaxial Tester and the Delft Flexible Wall Biaxial Tester

A number of comparative studies has been performed on the results of different shear testers (Marjanovic et al. 1999, Ose et al. 2000, Verlinden 2000) and on the results from the same shear tester by different laboratories and operators (Akers, 1992). In general, these studies show large differences. The cause of these persistent differences is often sought in the test procedure or the skill of the operator. Next to these causes, different testers (and different procedures) let the powder undergo different stress and strain patterns and thus are in fact not measuring the same thing. A tester in which the powder undergoes consolidation, preshear and failure (e.g. Jenike Tester) will produce a different result as a tester which does not use preshear (e.g. Johanson Indicizer). This means on the other hand, that when the applied procedure (including pretreatment and filling) is exactly the same, tester should give similar results.

The Braunschweig Biaxial Tester (BBT) and the Flexible Wall Biaxial Tester (FWBT) are part of a new generation of advanced powder testers whose goal is to fundamentally investigate powder flow. Therefore, the BBT and the FWBT have been compared in a cooperation of the Institut für Mechanische Verfahrenstechnik of the Technical University of Braunschweig and the Particle Technology group of the Delft University of Technology.

A series of tests consisting of uniaxial and biaxial consolidations with subsequent shear have been performed. The applied strain paths are given in table 4.3.

Table 4.3: Applied strain paths in the BBT and FWBT comparison experiments.

	Uniaxial		Biaxial	
	length* [mm]	strain [-]	length* [mm]	strain [-]
start				
length X	100.00	-	115	-
length Y	100.00	-	115	-
after step 1				
length X	81.00	-0.19	103.5	-0.10
length Y	100.00	0.00	103.5	-0.10
time [s]	20000		10000	
after step 2				
length X	100.00	0.00	93.15	-0.19
length Y	81.00	-0.19	115.00	0.00
time [s]	20000		11100	

\* This length should be divided by 2 to give the positions of the motors of the FWBT.

Standard BCR-limestone (Akers, 1992) is used for all experiments. The filling procedure for the FWBT is described in paragraph 4.3.5, the filling procedure of the BBT is slightly different. The densification in the z-direction took place by applying a known strain to the sample: the original height of 42 mm is decreased to a height of 35 mm. This procedure homogenizes the bulk density over the height as in the

procedure for the FWBT (Harder, 1985). The biaxial and uniaxial consolidation experiments are given in figure 4.39 and 4.40.

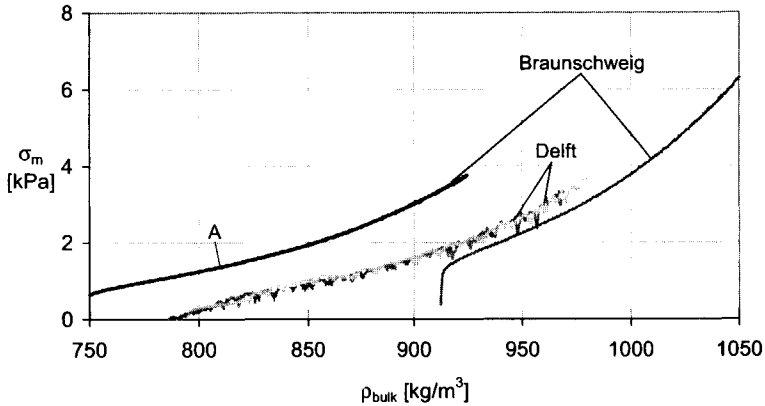


Figure 4.39: Uniaxial consolidation experiments in the Braunschweig Biaxial Tester and the Flexible Wall Biaxial Tester. No consolidation in  $z$  direction is applied during filling in experiment A.

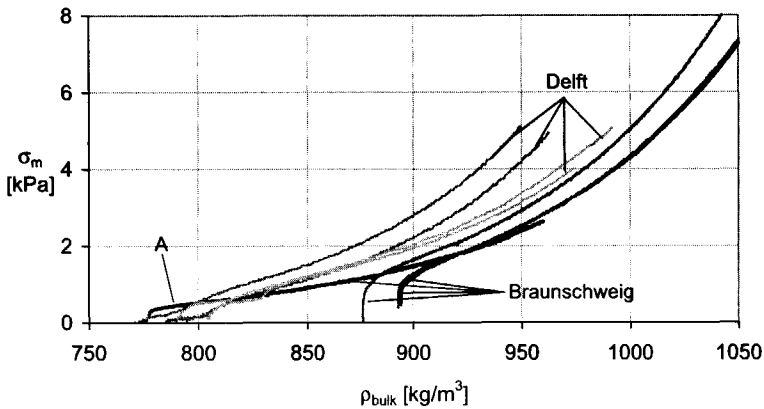


Figure 4.40: Biaxial consolidation experiments in the Braunschweig Biaxial Tester and the Flexible Wall Biaxial Tester. No consolidation in  $z$  direction is applied during filling in experiment A.

The biaxial experiments in the FWBT produce a higher consolidation curve than the same experiments in the BBT. The initial bulk density of the samples in the BBT is generally much higher than in the FWBT. This is probably due to the differences in the initial consolidation procedure in the  $z$  direction. The experiments labeled "A" in figures 4.39 and 4.40 have been performed with the BBT without an initial consolidation in the  $z$  direction. This gives an inhomogeneous density distribution over the height but also shifts the consolidation curve to the left. In the uniaxial consolidation the A experiment does not coincide with the other consolidation curves, but in the biaxial consolidation it does. The reason for this is unknown.

If the inaccuracy in the determination of the bulk density in the FWBT is taken into account (figure 4.18) the consolidation curves of the BBT and the FWBT do agree very well (figure 4.41).

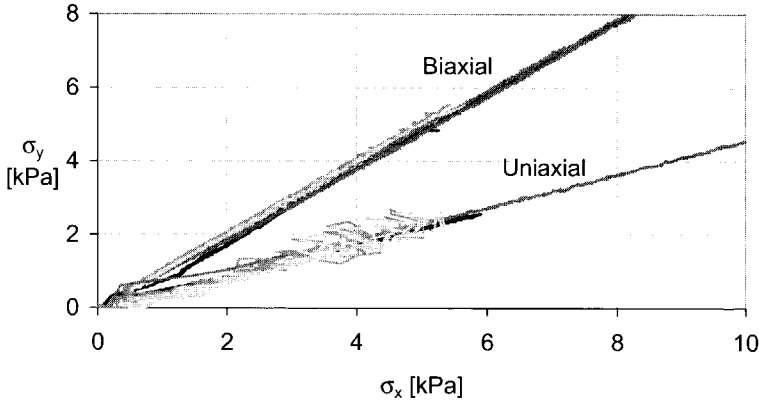


Figure 4.41: Biaxial and uniaxial consolidations in the Braunschweig Biaxial Tester and the Flexible Wall Biaxial Tester.

The steady state values for the major and minor principal stresses in the shear step after the uniaxial and biaxial consolidation are given in figures 4.42. It is concluded that the steady-state stresses lay on the same failure line, although not exactly the same values have been reached. This is not expected because of the already occurred differences in the consolidation step.

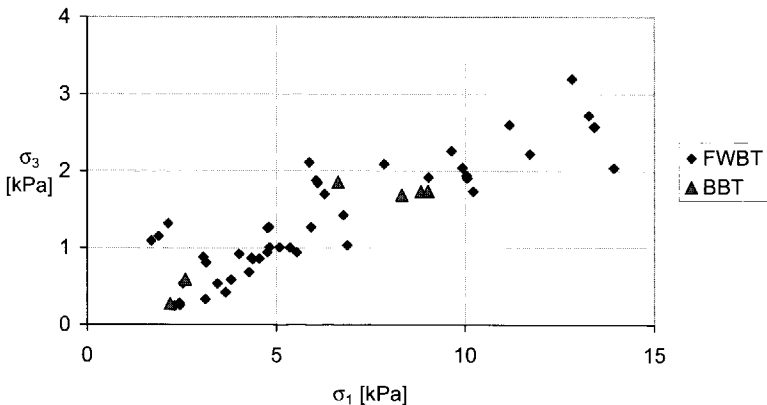


Figure 4.42: Shear after uniaxial and biaxial consolidation in the Braunschweig Biaxial Tester and the Flexible Wall Biaxial Tester.

From this cooperation between the BBT and the FWBT it is concluded that the BBT is a very precise tester, but has less possibilities to apply different stress or strain paths.

The FWBT is more flexible due to its membranes and due to its stress and strain control of four walls. However, the membranes also make the tester more inaccurate than the BBT. It is unclear what the influence of the difference in height between the BBT and the FWBT is on the results. The experimental comparison shows that the BBT and the FWBT qualitatively agree on their results.

## 4.7 Flow function of BCR-limestone

Jenike (1961) developed the procedure for the measurement of the flow function consisting of three steps. The first two are intended to bring the powder into a certain state. This state is called the history of the powder. These two steps, consolidation and preshear, have been described in the previous paragraphs. This paragraph covers the actual measurement of the unconfined yield strength and presents the resulting flow function.

### 4.7.1 Flexible Wall Biaxial Tester flow function

With the Jenike Tester a series of experiments are needed to determine one point of the flow function via extrapolation. With the FWBT the unconfined yield strength can be measured directly without extrapolation. The procedure for this measurement is described by Kraan (1996) and Maltby (1993) and is given in figure 4.43. The procedure is performed in a stress controlled manner and consists of four steps.

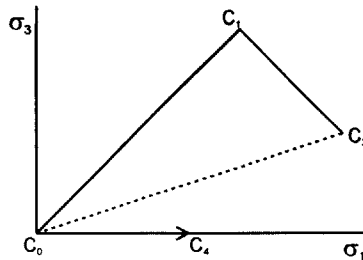


Figure 4.43: Stress controlled path for the measurement of the unconfined yield strength in the FWBT.

The first step is the application of a biaxial consolidation up to a certain chosen pressure ( $C_0$  to  $C_1$ ). The second step brings the powder in steady-state shear and because this is the first shear step, it is called the preshear step ( $C_1$  to  $C_2$ ). The endpoint of this line is determined by the powder and results in the major and minor preshear stress. In the third step the stresses are brought back to zero ( $C_2$  to  $C_0$ ). The powder is now in a certain state depending on the first two steps. In the final step the stresses in one direction increase while the stress in the perpendicular direction are kept zero ( $C_0$  to  $C_4$ ). The powder can withstand the increasing stress up to a certain point at which it will fail. No further increase of the stress is possible thereafter. The point that is reached in this step is the unconfined yield strength. In the FWBT the stress in the  $z$  direction cannot be controlled and is assumed to be the intermediate stress. This assumption has proven to be valid.



In order to perform this experiment automatically in the FWBT two requirements have been defined in order for the software to decide whether steady-state had been reached in the second step of the procedure (figure 4.43). The first requirement is that no stress change has taken place for half an hour. This requirement is defined for a strain rate of  $1 \cdot 10^{-5} \text{ s}^{-1}$  and was based on practical experience. The second requirement is that the sum of the absolute membrane deformations has to be larger than  $100 \mu\text{m}$ . This limit is also based on practical experience. It indicates that the powder is shearing and together with the first requirement defines steady-state shear. These requirements proved to be practical and accurate.

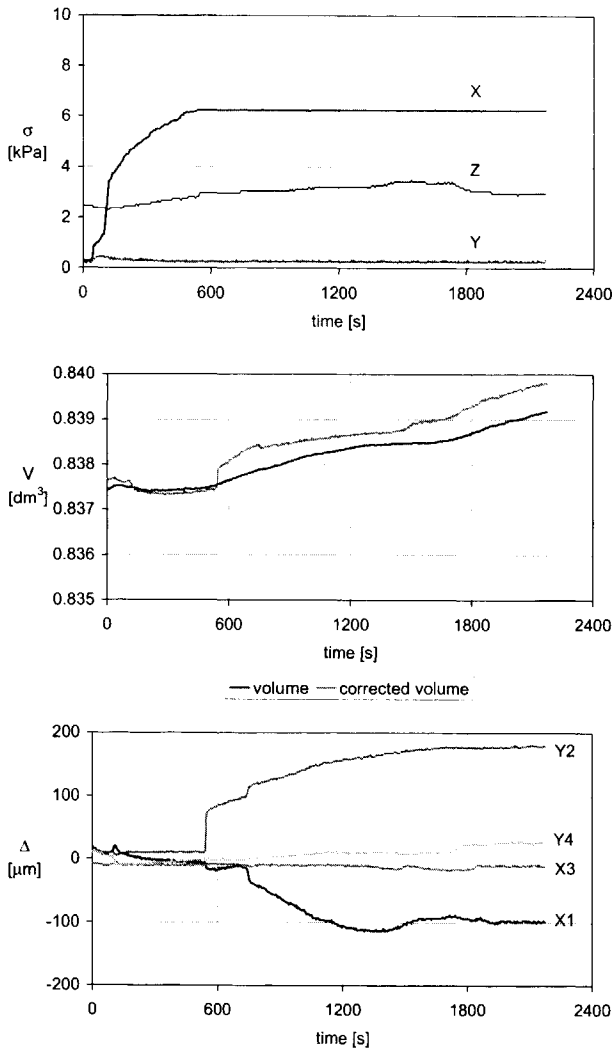


Figure 4.44: Typical result for the determination of the unconfined yield strength (step  $C_0$  to  $C_4$  in figure 4.43).

The third step of the procedure in figure 4.43 was performed such that the membrane deformations were brought back within the allowed limit of 10  $\mu\text{m}$ . In this step the stress in the z direction decreased much less than the X and Y stresses. For the experiments that were performed with a relatively low consolidation (lower than 5 kPa) this formed a problem because the z stress became the major principal stress during the determination of the unconfined yield strength in the fourth step. To overcome this problem, the volume of the tester, after the X and Y stresses reached their zero-level, has been increased with 20  $\mu\text{m}$  in x and y direction. This appeared to be enough for the Z stress to decrease to a near zero value. Comparison of experiments with and without this volume increase did not show an influence on the unconfined yield strength. Another problem in this step was that the stresses could not reach zero. This is due to imperfections in the calibrations of the monitor pressure and the control pressure. A value of 0.3 kPa has been taken as the setpoint value instead. The increase in the unconfined yield strength as a result of this is negligible. This has been tested in an experiment in which the pressure valves were opened during the last step assuring a minor principal stress equal to zero.

The stress increase in the fourth step is quite rapidly. The powder has a certain strength and the negative membrane deformations are very small. When the unconfined yield strength is reached, the powder breaks and the membrane deformations increase very rapidly. This is due to the dilation. The deformations are so extreme that they cannot be corrected because the powder keeps on yielding. A typical result for this last step is given in figure 4.44.

The unconfined yield strength as a function of the major principal stress during steady-state shear defines the flow function. The flow function for BCR-limestone as measured with the FWBT is presented in figure 4.45 and the data is given in table 4A.1 in the Appendix of this chapter.

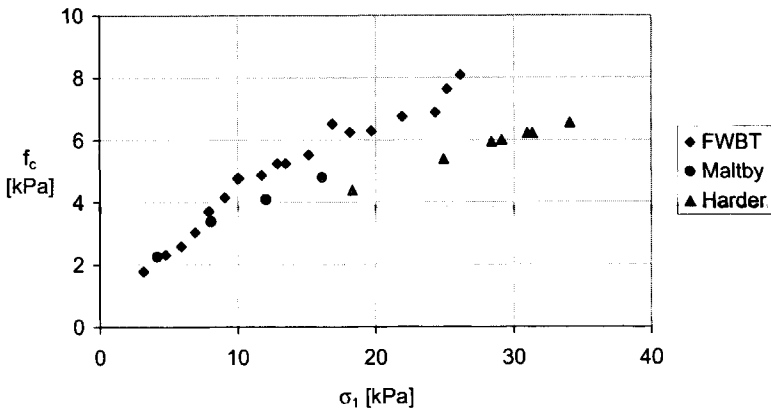


Figure 4.45: Flow function of BCR-limestone measured with the FWBT and compared with other true biaxial testers (Maltby 1993, Harder 1986).

In comparison with flow functions from other true biaxial testers (Maltby 1993, Harder 1986), the FWBT predicts higher values especially at larger major principal preshear stresses. In paragraph 4.7.3 the differences with the results of Maltby will be

discussed in detail. It should just be remarked here, that in the determination of the unconfined yield strength Maltby also keeps the intermediate stress at a zero level.

The results of the Braunschweig Biaxial Tester by Harder (1986) deviate extensively from the results of the FWBT. The powder Harder used was not BCR-limestone but a similar limestone with approximately the same mean particle size. The procedure Harder used was also slightly different from the procedure used here. In the preshear step, he applied the minor principal stress and then increased the stress in the other direction up to the major principal stress at steady-state shear. In the current theory this should not make a difference. It is uncertain what causes the difference between the flow function, also because it is unknown if the same samples are used.

In figure 4.46 the measured flow function of BCR-limestone is compared with results of the Jenike Tester. The flow function by Akers (1992) is produced by a number of laboratories and is often used as the standard for the certified BCR-limestone. Saraber (1991) only measured at low values of  $\sigma_1$ . These Jenike Tester flow functions coincide only with the FWBT measurements at low values of the major principal shear stress. Kraan (1996) suggests that the Jenike Tester does not apply a uniform deformation and in chapter 3 it was shown that the shear plane in a direct shear tester is not horizontal. This means that the normal and shear stress on the shear plane are measured incorrectly in the Jenike Tester. Kraan (1996) concluded that the shear stresses measured with the Jenike Tester are too low.

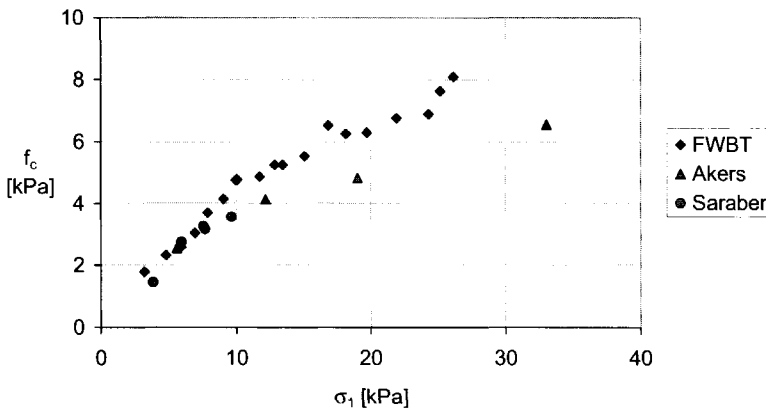


Figure 4.46: Flow function of BCR-limestone measured with the FWBT and compared with Jenike results (Akers 1992, Saraber et al. 1991).

Another contribution to the difference between the results of the FWBT and the Jenike Tester is caused by time consolidation. The strain rate for all FWBT experiments is  $1 \cdot 10^{-5} \text{ s}^{-1}$  and the time to perform the consolidation and the shear step ranges from 10 to 23 hours. From figure 4.2 the change in the flow function due to time consolidation is estimated at 10 %. This change almost completely explains the differences. The influence of time consolidation is larger at higher consolidation values, which could explain why the flow functions deviate more at higher major principal preshear stresses.

### 4.7.2 Correction of the flow function measured in the FWBT by Kraan (1996)

Kraan (1996), who built the FWBT, measured the flow function of BCR-limestone as well. This flow function is very high compared to literature and also compared to the flow function as measured in this thesis. It is believed that Kraan overrated the flow function because of a mistake in the control program. An estimation has been made to correct the data of Kraan. This estimation is based on the measured relation between the real applied stress on the powder and the setpoint pressure in the control program. This relation is:

$$\text{real stress} = 0.08 + 0.72 \cdot \text{setpoint stress} \quad [\text{kPa}] \quad (4.4)$$

The corrected flow function agrees very well with the results presented in this thesis (figure 4.47 and table 4A.2). It should be remarked that the calibration was only done for pressures up to 11 kPa. This means that the correction of the two largest points of the flow function of Kraan is done by extrapolation.

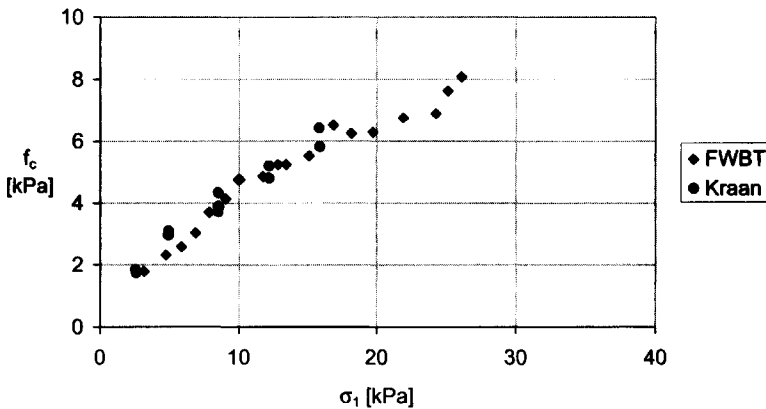


Figure 4.47: Flow function measured with the FWBT compared with the corrected flow function by Kraan (1996).

### 4.7.3 Influence of intermediate principal stress

The true biaxial tester of the Telemark Institute of Technology (Maltby, 1993) is very similar to the FWBT. They both work with flexible membrane walls that can be pressurized for the application of stress. However, the deformation of the membranes in the Norwegian Biaxial Tester is detected by "make and break" contacts. This mechanism makes it difficult to detect dilation of the sample and therefore the determination of the unconfined yield strength is inaccurate. To solve this problem, Maltby removed the top lid and the cover membrane in the last step of the unconfined yield strength procedure (figure 4.43 step  $C_0$  to  $C_3$ ). The operator could

now observe the top face of the sample and could visually determine the start of the dilation.

Maltby's method implies a different state of stress during the measurement of the unconfined yield strength (figure 4.48c). Both the minor and the intermediate principal stress are now equal to zero in contrast to the procedure applied in the FWBT (figure 4.48b) where the intermediate stress has a value between the major and minor principal stress. Maltby argued that the intermediate stress level is of minor importance when the sample dilates. This is not true because the value of the intermediate stress can influence the direction of the shear planes that form in the sample. In Maltby's case, the sample can expand in two directions. One of these directions has been used during the preshear and the structure inside the powder has been built custom to this shear direction. This structure is missing in the other direction. Therefore, as Kraan (1996) already concluded, the unconfined yield strength will be lower than in the procedure with a confining top lid.

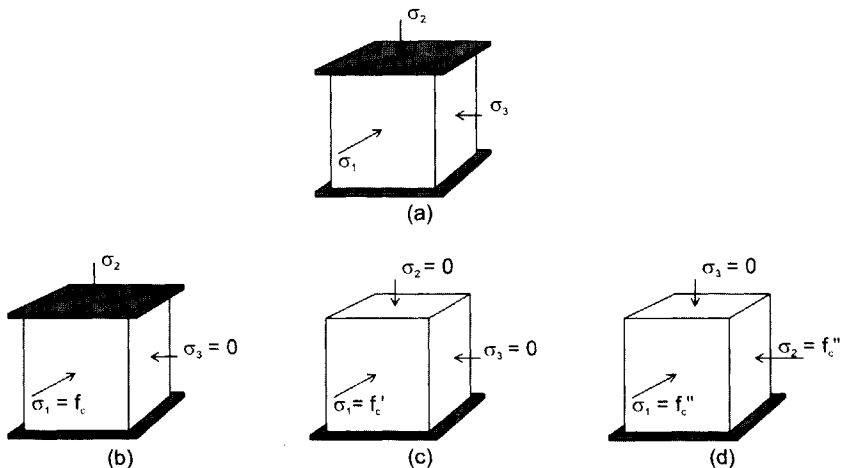


Figure 4.48: State of stress during steady-state shear (a), determination of the unconfined yield strength with sample confined in z direction (b), sample unconfined in z direction with  $\sigma_2 = \sigma_3$  (c) and sample unconfined in z direction with  $\sigma_2 = \sigma_1$ (d).

This conclusion is checked by using Maltby's experimental procedure in the FWBT. The results, presented in figure 4.49 and table 4A.3, show that Maltby's flow function can be duplicated and that this procedure leads to a lower unconfined yield strength.

Maltby's procedure can be seen as the determination of the unconfined yield strength with a minimum intermediate stress. The procedure can also be performed with a maximum intermediate stress (figure 4.48d). This experiment can in principle only be performed correctly by a true triaxial tester. However, by taking the lid off the FWBT and applying the major principal stress in the two other directions, it is also possible to apply an intermediate stress equal to the major consolidation stress. However, this intermediate stress is in a different direction than during the preshear

step (figure 4.48a). This means that the principal axes of stress rotate with respect to the preshear step.

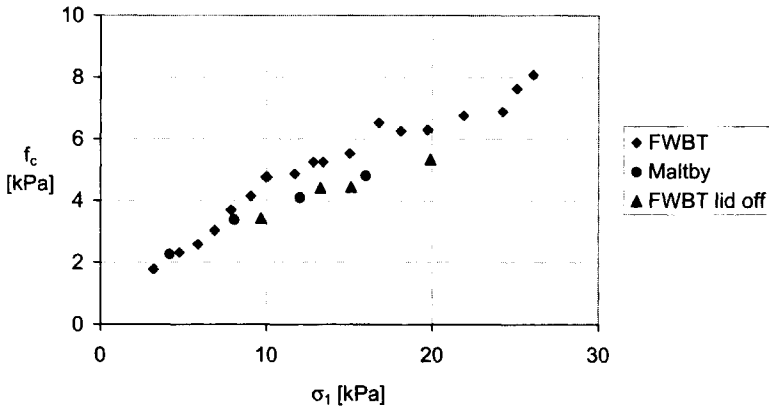


Figure 4.49: Flow function of BCR-limestone measured in the FWBT according to Maltby's procedure (1993).

Figure 4.50 shows the stress paths as a function of the volumetric strains for the determination of the unconfined yield strength according to figure 4.43 in which the last step varied according to figure 4.48 b, c and d. The volumetric strain is calculated on basis of the x and y positions of the walls. For the experiments in which the lid is taken off, the measured volumetric strain is overestimated because the powder deforms in the z direction with an unknown strain (figure 4.50 middle and bottom). The stress path for the regular determination of the unconfined yield strength (figure 4.48b) is characterized by a sharp change. This happens when the powder breaks and starts shearing. This point was clearly seen from the sudden increase in the membrane deformations. However, in the determination of the unconfined yield strength according to the other two procedures (figure 4.48c and d) a clear endpoint is missing. The powder behaves like being in an underconsolidated state and reaches some state of shear for minimum intermediate stress. The stress path of the maximum intermediate stress did not reach any shear.

For the usual procedure (figure 4.48 b) the powder dilates at the moment the unconfined yield strength is reached. Before the dilation the powder slightly decreases its volume. The other types (figure 4.48 c and d) do not show a dilation, but the volume of the sample is not precisely known as mentioned before and a dilation could occur without being noticed. It is believed that this does not happen because of the fact that there is no sudden increase in the membrane deformations.

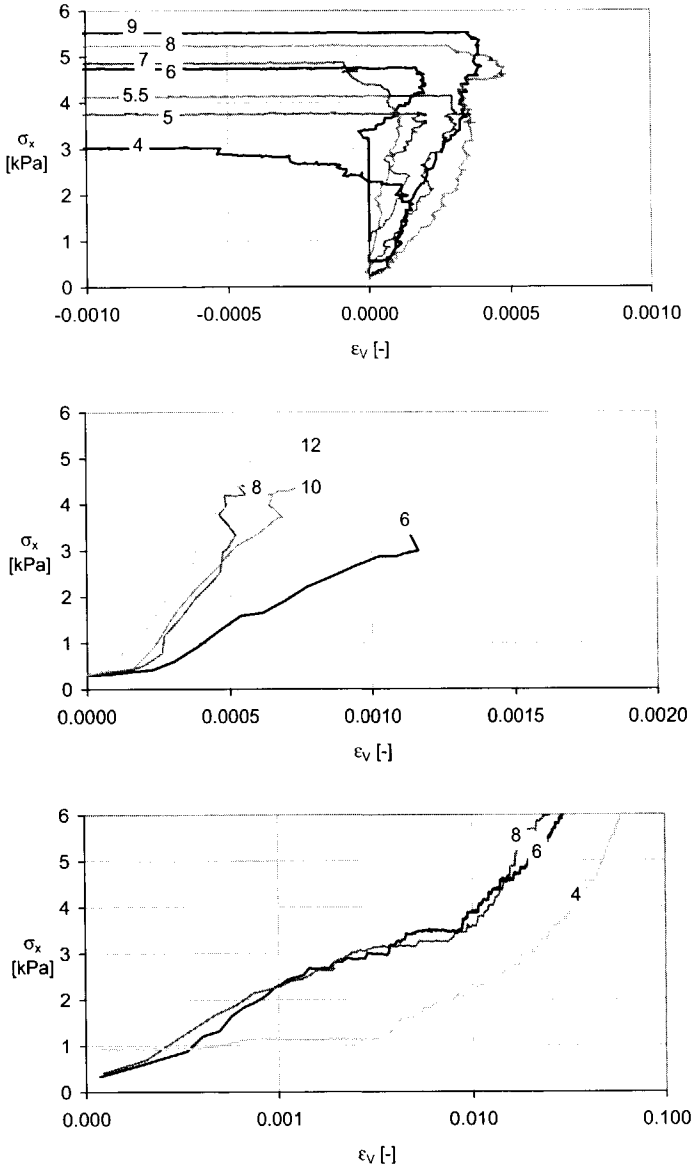


Figure 4.50: Influence of the intermediate stress on the determination of the unconfined yield strength. Sample confined in z direction (top), sample unconfined in z direction with  $\sigma_2 = \sigma_3$  (middle) and sample confined in z direction with  $\sigma_2 = \sigma_1$  (bottom). The numbers indicate the normal stress in kPa at the end of the consolidation step.

In figure 4.51 the deviatoric stress is given versus the mean stress for the three different types of unconfined yield strength measurement (figure 4.48 b, c and d). As mentioned above, both the regular procedure (b) and the procedure in which the

intermediate stress equals the minor principal stress (c) result in a endpoint of the major principal preshear stress. Procedure (d) does not reach such an endpoint and keeps on increasing. This indicates that the powder sample is overconsolidated in type b, underconsolidated in type c and even more underconsolidated in type d. From this it is concluded that the state of consolidation depends on the directions in which the deviatoric stress dominates. In type b this is clearly the same direction as in the preshear step (4.52 b). In type c the deviatoric stress can occur both in the same direction as in the preshear step but also in a new direction (figure 4.52 c). In type d the deviatoric stress occurs in two new directions (figure 4.52 d).

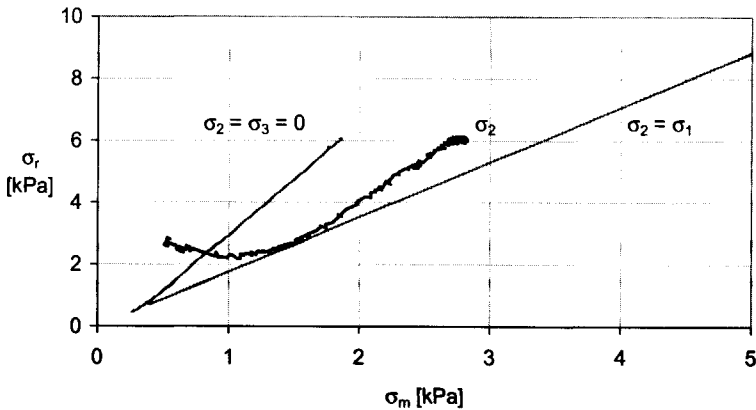


Figure 4.51: Influence of the intermediate stress on the stress path according to figure 4.48 b, c and d. The applied consolidation stress for all experiments is 8 kPa.

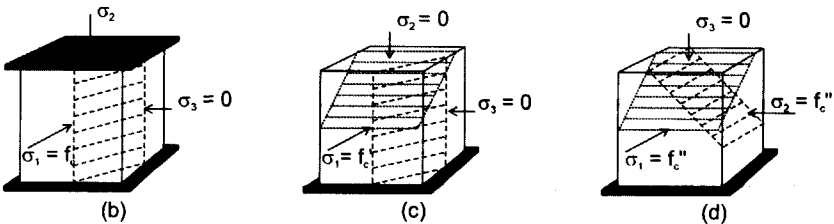


Figure 4.52: Shear plane directions during determination of the unconfined yield strength with sample confined in z direction (b), sample unconfined in z direction with  $\sigma_2 = \sigma_3$  (c) and sample unconfined in z direction with  $\sigma_2 = \sigma_1$  (d). Situations refer to figure 4.48.

It is concluded that the intermediate principle stress has a strong influence on the flow behavior of a cohesive powder. Wong and Arthur (1985) measured the influence of the intermediate stress on sand and found that it is negligible. The cohesion of the sample could be the cause for this difference between sand and limestone.



#### 4.7.4 Shear planes after determination of the unconfined yield strength

The determination of the unconfined yield strength ended in shear of the powder. The shear planes are thought to be characterized by the crack patterns of the powder after opening the tester and retracting the walls. The pictures taken of the three ways of determining the unconfined yield strength according to figure 4.48 are given in figure 4.53.

The difference in the crack pattern for the shear step and the consolidation step (figure 4.32) is obvious. The cracks are not parallel to the axes of the tester and the amount of cracks is much larger. The regular procedure for the determination of the unconfined yield strength (figure 4.48b) leads to vertical cracks all the way down to the bottom of the sample. The pictures of the experiments with the minimum and maximum intermediate stress (figure 4.53 middle and right) show clearly that the cracks are more horizontal now. This confirms idea of the formation of the shear planes drawn in picture 4.52.

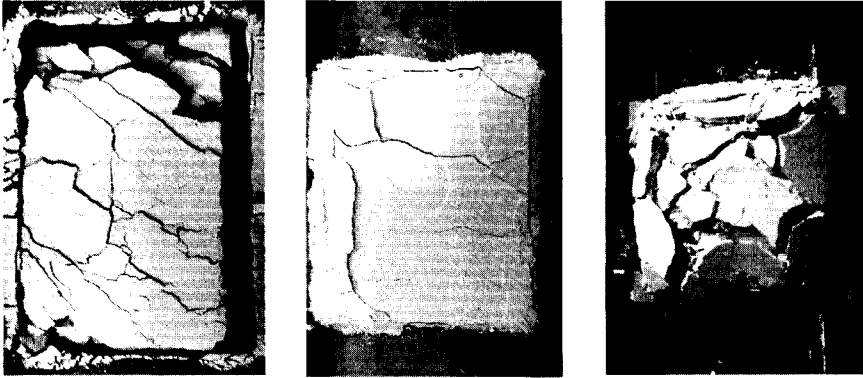


Figure 4.53: Photos of the shear planes in the intermediate stress experiments: normal procedure (left), sample unconfined in  $z$  direction with  $\sigma_2 = \sigma_3 = 0$  (middle) and sample unconfined in  $z$  direction with  $\sigma_2 = \sigma_1$  (right).

#### 4.8 Conclusion

The Flexible Wall Biaxial Tester is a suitable machine to investigate powder on its flow properties because of the divergence in stress and strain patterns that can be applied to the sample. The FWBT is limited in the application of a three dimensional stress or strain path. In comparison with the Braunschweig Biaxial Tester, the FWBT is less precise but is more flexible in the stress and strain paths it can apply. The experiments that are performed with both testers, consolidation and steady-state shear of BCR-limestone, are in good agreement with each other. The influence of the different heights of the testers is unknown.

A number of experiments has been performed with the FWBT to investigate the behavior of cohesive BCR-limestone. Samples of this material have been consolidated in three different ways: biaxially, uniaxially with two moving walls and uniaxially with

one moving wall. The stress paths of the biaxial consolidation lay higher than for the uniaxial consolidation, which agrees with results in literature (Nowak 1993). This is caused by the deviatoric stress or strain that probably facilitates the rearrangement of the particles. The uniaxial consolidation with one wall showed a difference between the normal stresses working on opposite sides. This difference is thought to occur because of the inhomogeneity of the sample.

The consolidation path is also influenced by the strain rate: the slower the experiment is performed the higher the stress for a certain bulk density. This is confirmed by measurements of Maltby (1993) and Cristescu (1988), but it is in contradiction with strain rate experiments of Zetzener et al. (1998).

The flow function of BCR-limestone has been measured and is shown to be higher than the flow functions measured with the Jenike Tester. This is partly caused by time consolidation in the FWBT because the measurement procedure takes much longer than in the Jenike Tester.

The intermediate stress has a major influence on the flow function and, therefore, the flow function is not an unique characterization of the powder flow behavior. This clearly indicates that the flow of powder should be thought of in three dimensions. The development of a true triaxial tester is necessary to make the fundamental investigation of powder flow possible.

# Appendix

## 4A.1 Flow function experiments

Table 4A.1: Overview of the flow function experiments with the FWBT.

Step 1	$\rho_{\text{bulk}}$ after step 1	$\sigma_c$	Step 2						Step 4					$\sigma_{1p}$	$\sigma_{3p}$	$f_c$
			X1	Y2	X3	Y4	Z	X1	Y2	X3	Y4	Z				
			[kPa]						[kPa]							
1	891.7	2.0	3.17	0.81	3.17	0.81	2.13	1.76	0.15	1.81	0.21	1.26	3.17	0.81	1.79	
2	842.4	3.0	4.76	1.25	4.76	1.27	2.72	2.32	0.14	2.32	0.19	1.59	4.76	1.26	2.32	
3	830.3	4.0	6.89	1.00	6.91	1.07	3.68	2.95	0.00	3.13	0.04	2.06	6.90	1.04	3.04	
4	830.9	4.0	5.88	2.12	5.88	2.10	3.33	2.61	0.23	2.56	0.00	1.39	5.88	2.11	2.59	
5	817.3	5.0	7.86	2.1	7.89	2.08	4.21	3.79	0.17	3.62	0.34	1.99	7.88	2.09	3.71	
6	830.6	5.5	9.06	1.93	9.03	1.90	4.79	4.15	0.26	4.15	0.40	2.40	9.05	1.92	4.15	
7	832.6	6.0	9.94	2.03	9.94	2.05	5.21	4.76	0.27	4.76	0.19	2.62	9.94	2.04	4.76	
8	832.0	6.0	10.06	1.90	10.06	1.90	5.04	4.76	0.22	4.79	0.21	2.68	10.06	1.90	4.77	
9	841.0	7.0	11.77	2.22	11.67	2.22	6.25	4.88	0.24	4.86	0.15	2.97	11.72	2.22	4.87	
10	827.6	8.0	13.43	2.56	13.43	2.59	6.63	5.25	0.14	5.25	0.38	2.84	13.43	2.58	5.25	
11	806.9	8.0	12.89	3.20	12.79	3.20	6.79	5.27	0.40	5.23	0.25	2.62	12.84	3.2	5.25	
12	828.2	9.0	15.09	2.91	15.06	2.93	6.97	5.54	0.15	5.52	-0.15	2.93	15.08	2.92	5.53	
13	835.5	10.0	16.85	3.17	16.82	3.17	8.23	6.52	0.24	6.52	0.29	3.51	16.84	3.17	6.52	
14	815.8	11.0	18.14	3.83	18.14	3.86	8.54	6.25	0.15	6.25	0.15	2.98	18.14	3.85	6.25	
15	818.3	12.0	19.73	4.27	19.70	4.27	9.21	6.27	0.20	6.30	0.10	3.30	19.72	4.27	6.29	
16	842.5	14.0	21.88	6.08	21.92	6.54	11.16	6.69	0.41	6.81	0.51	3.52	21.90	6.31	6.75	
17	837.3	14.5	23.93	4.40	24.59	4.42	11.19	6.89	0.29	6.89	0.42	3.74	24.26	4.41	6.89	
18	832.0	15.0	24.51	4.35	25.71	4.32	11.82	7.62	0.27	7.64	0.24	4.70	25.11	4.33	7.63	
19	810.2	16.0	26.10	5.93	26.10	6.57	12.61	8.08	0.33	8.08	0.31	4.61	26.10	6.25	8.08	

Table 4A.2: Overview of the corrected flow function experiments of Kraan (1996).

	Step 1			
	$\sigma_c$	$\sigma_{1p}$	$\sigma_{3p}$	$f_c$
	[kPa]	[kPa]	[kPa]	[kPa]
1	1.51	2.55	0.47	1.84
2	1.51	2.59	0.44	1.74
3	2.95	4.96	0.93	2.97
4	2.95	4.97	0.92	3.09
5	5.10	8.56	1.63	3.88
6	5.10	8.51	1.70	3.72
7	5.10	8.53	1.66	4.33
8	7.24	12.19	2.30	5.21
9	7.24	12.17	2.32	4.82
10	9.39	15.80	2.99	6.43
11	9.39	15.86	2.93	5.82

Table 4A.3: Overview of flow function experiments with the lid of the FWBT taken off in the 4<sup>th</sup> step.

Step 1	Step 1	Step 2					Step 4					$\sigma_{1p}$	$\sigma_{3p}$	$f_c$	
$P_{bulk}$ after step 1	$\sigma_c$	X1	Y2	X3	Y4	Z	X1	Y2	X3	Y4	Z				
		[kPa]					[kPa]								
1	968.7	6.0	9.55	2.25	9.77	2.27	5.11	3.42	0.22	3.44	0.15	*	9.66	2.26	3.43
2	1002.0	8.0	13.28	2.73	13.28	2.71	6.63	4.40	0.27	4.44	0.25	*	13.28	2.72	4.42
3	988.7	10.0	15.16	4.83	15.16	4.83	8.28	4.52	0.28	4.37	0.22	*	15.16	4.83	4.44
4	1027.9	12.0	19.87	4.10	19.90	4.10	10.05	5.32	0.27	5.35	0.39	*	19.89	4.10	5.33

\* The lid has been taken off in the fourth step, the Z stress is assumed to be zero.

# Anisotropy in powder flow behavior

In this chapter a phenomenon of powder is investigated that cannot be explained by the known powder flow theories. This phenomenon is anisotropy and it is seen as a typical feature of structure that can form in powder. Structure is not an issue in the current theory. Work done by other researchers mainly concentrates on the anisotropic behavior of relatively coarse granular material like sand. Much less is known about cohesive powder. In this research the Flexible Wall Biaxial Tester is used to get more insight in anisotropy in cohesive BCR-limestone.

## 5.1 Introduction

One fundamental assumption for most present powder flow testers and the theory of Jenike (1961, 1964) is that powder behaves isotropically. However, from different experiments (Molerus 1975, Gerritsen 1985, Saraber et al. 1991) it appears that the flow properties of a powder depend on the direction of measurement. This phenomenon is called anisotropy and is the subject of this chapter.

The reason for the investigation of anisotropy is that it cannot be explained by existing theories for the flow of powder (Jenike 1961, Hvorslev 1937, Roscoe et al. 1958). It is seen as a typical sign of the existence of structure in powder. This structure forms as a consequence of the process conditions but also as a consequence of the particle properties such as size and shape distribution. The exclusion of structure from theory can have large influences on the characterization of powders (Feise, 1996).

The chapter starts with a literature overview of anisotropy in powder flow. It will be explained why this typical phenomenon cannot be predicted by the known theory and why structure is seen as the missing link. Investigations in the area of soil mechanics have also shown the importance of structure for sands and soils. Developments in the soil mechanics research that are important for the field of powder technology will be reviewed.

The Flexible Wall Biaxial Tester (FWBT) as introduced in chapter 4 will be used to visualize anisotropy in BCR-limestone samples. Therefore, powder samples have been prepared with a biaxial consolidation step and a preshear step during which the volume is kept constant. The samples are then deformed, again with constant volume, in eight different ways.

The goal of this chapter is to prove the existence of anisotropy in cohesive BCR-limestone and therefore show that the assumption of isotropy in powder is incorrect. It will be explained that structure is the parameter that has to be captured in order to

include anisotropic phenomena in powder flow theory. The consequence of anisotropy will be shown by the measurement of an anisotropic flow function in which the direction of the major principal stress during shear rotates  $90^\circ$  with respect to the direction during preshear.

## **5.2 The occurrence of anisotropy**

In this paragraph the anisotropy phenomenon will be defined. An overview of experiments from literature will be given and the ideas and theories for the explanation of anisotropy are presented.

### **5.2.1 Definition of anisotropy**

When a powder sample is isotropic, its properties are independent of the direction in which they are measured. For example, a powder can be isotropic in terms of permeability, electrical conductivity or shear deformation. Anisotropic behavior means that such a property depends on the direction of measurement. In powder flow behavior this can be the direction in which the major principal stress or strain is applied or the direction of shear deformation.

In literature one often speaks of inherent and induced anisotropy. This distinction originates from soil mechanics (Wong, 1985; Arthur et al, 1985) which defines inherent anisotropy as being the result of the deposition process and the grain characteristics and entirely independent of the applied strains. Induced anisotropy is then due to the strain associated with an applied stress. This type also depends on the grain characteristics although Wong does not include this in his definition. This definition of different anisotropy phenomena is based on soil samples taken from sediment layers which are anisotropic due to their deposition history. Subsequently performed experiments with these samples can induce further anisotropy. The definition of inherent and induced anisotropy is purely based on the distinction between the two described situations.

Feise (1998) uses the definitions of inherent and induced anisotropy in powder technology. Inherent anisotropy occurs from the filling procedure and induced anisotropy from the consolidation and following shear steps. In contradiction to Feise (1998), it is believed that the shape and other characteristics of the particles influence both types of anisotropy. Feise suggests that the shape only influences the inherent anisotropy.

Li and Puri (1996) make a distinction between structural or geometrical anisotropy and mechanical anisotropy. The first describes the state of the spatial arrangement of individual particles. This can cause anisotropy in deformation or strength of the powder which is called mechanical anisotropy. The distinction Li and Puri make is based on cause and result for the specific triaxial tests they perform.

In this chapter the definition of inherent anisotropy reflects the state of the powder after filling and induced anisotropy is caused by the stress and strain paths the sample undergoes after filling. Both types of anisotropy may depend both on the basic properties of the powder and on the process that is applied. As Hicher (1998) states: if

it were possible to reconstruct the complete history of the sample, it would not be necessary to distinguish between induced and inherent anisotropy.

### 5.2.2 Anisotropy investigations with simple testers

The Jenike (1961, 1964) procedure for the design of silos uses the flow function, which defines the flow characteristic of a powder. One of the assumptions in the definition of the flow function is that the powder behaves as an isotropic continuum.

Molerus (1975) showed that a yield locus, being part of the procedure to measure the flow function, could be influenced by changing the direction of shear after the preshear step with  $90^\circ$  (figure 5.1).

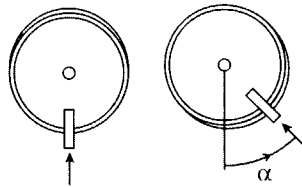


Figure 5.1: Measurement of anisotropy in the Jenike tester as proposed by Molerus (1975). Preshear (left) and shear (right) step for measurement of a yield locus.

Saraber et al. (1991) measured yield loci for angles ranging from 0 to 180 degrees between the direction of preshear and the direction of shear (figure 5.1). The unconfined yield strength resulting from these yield loci is shown to decrease strongly and reaches a minimum after a rotation of approximately 90 degrees (figure 5.2).

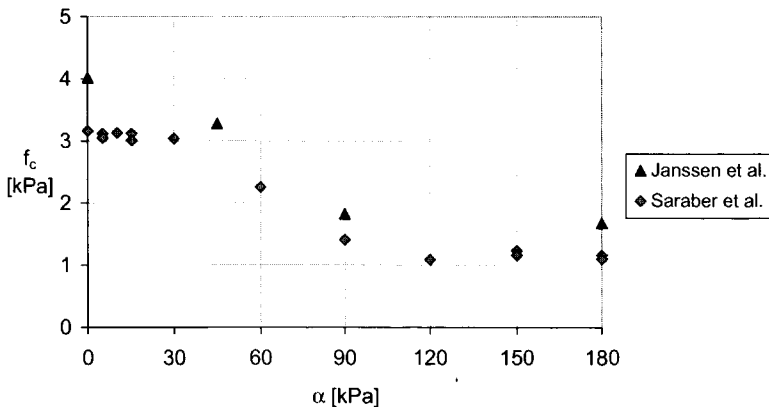


Figure 5.2: The unconfined yield strength as a function of the angle derived from Jenike results with  $\sigma_{1p} \cong 7.7$  kPa (Saraber et al., 1991) and  $\sigma_{1p} \cong 7.0$  kPa (Janssen et al., 1999).

Gerritsen (1985) used a cylindrical triaxial tester to investigate the influence of the consolidation procedure on the anisotropic behavior of powder. He used two types of consolidation: one in which all stresses are equal and one in which the radial stress is

kept at a lower constant value than the axial stress (figure 5.3). The consolidation has been applied for 3 minutes. After that, the stresses have been lowered and subsequently the sample was loaded with an increasing axial stress until the sample fails. This is called step two.

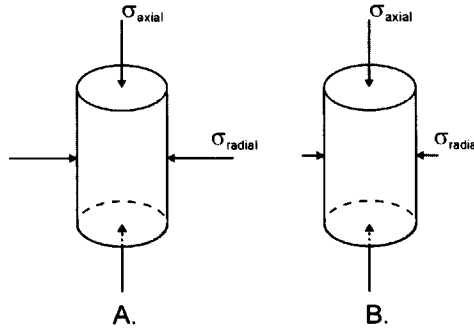


Figure 5.3: Consolidation types used by Gerritsen (1985): all stresses equal (A) and with a constant lower radial stress compared to the axial stress (B).

Gerritsen defines the measured axial stress as the unconfined yield strength. In figure 5.4 results for three different consolidations, i.e. type A: (1)  $\sigma_{1c} \equiv \sigma_{3c}$  and type B: (2)  $\sigma_{3c} = 10$  kPa and (3)  $\sigma_{3c} = 30$  kPa, are given. Gerritsen draws the conclusion that for two samples having the same  $\sigma_{1c}$ , the one with the lowest  $\sigma_{3c}$  has the highest strength.

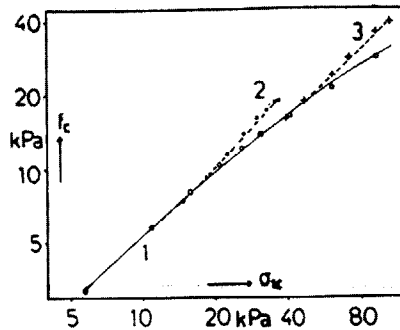


Figure 5.4: Log-log representation of unconfined yield strength versus major principal consolidation stress for limestone (Violet-etikette®). Type A (1)  $\sigma_{1c} \equiv \sigma_{3c}$ ; type B (2)  $\sigma_{3c} = 10$  kPa ; type B (3)  $\sigma_{3c} = 30$  kPa Gerritsen (1985).

No preshear step as defined by Jenike (1961, 1964) is applied in the consolidation procedure of type A (figure 5.3). In type B preshear occurs in a limited way. It is restricted by the radial stress: the lower the radial stress the more preshear occurs. The preshear step increases thus the strength of the sample.



### 5.2.3 Anisotropy in biaxial and triaxial testers

Harder (1986) investigated the influence of the type of consolidation on the shear behavior of a powder sample in the Braunschweig Biaxial Tester. The resulting bulk density of the sample after the consolidation is equal for all types. Types I and III are uniaxial consolidations in x and y direction respectively. Type II is a biaxial consolidation (figure 5.5). This consolidation step is a strain controlled operation.

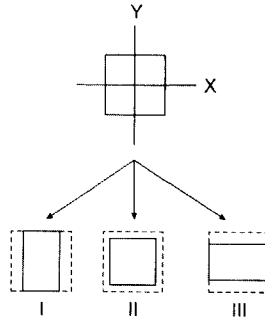


Figure 5.5: Uniaxial consolidation in x (I) and y direction (III) and biaxial consolidation (II) in the biaxial tester (Harder, 1986).

The normal stress paths for the three types were approximately identical according to Harder (1985). After this consolidation procedure the stresses were reduced and in the next step a constant and chosen value of the minimum principal stress  $\sigma_3$  was applied in the y direction while the major principal stress  $\sigma_1$  increased in x direction until steady-state was reached. Harder constructed the flow function with the above described procedure which did not contain a preshear step.

Schwedes and Schulze (1990) showed that the flow function measured by Harder (1986) is dependent on the type of consolidation that is applied (figure 5.6). They also compared these flow functions with a flow function in which a preshear step was included and thus proved that the application of a preshear step does result in a higher flow function (figure 5.6).

Schwedes and Schulze (1990) concluded that if the direction of the major principal stress at consolidation ( $\sigma_{1,c}$ ) is in the same direction as the major principal stress during shear, as in case I, the flow function is higher compared to case II and III. The different types of consolidations can be compared with different testers which have different procedures and different consolidations. The results of Harder (1986) and Schwedes and Schulze (1990) prove that the results of a shear tester depend on the procedure and geometry of the tester, because they both determine the consolidation of the sample.

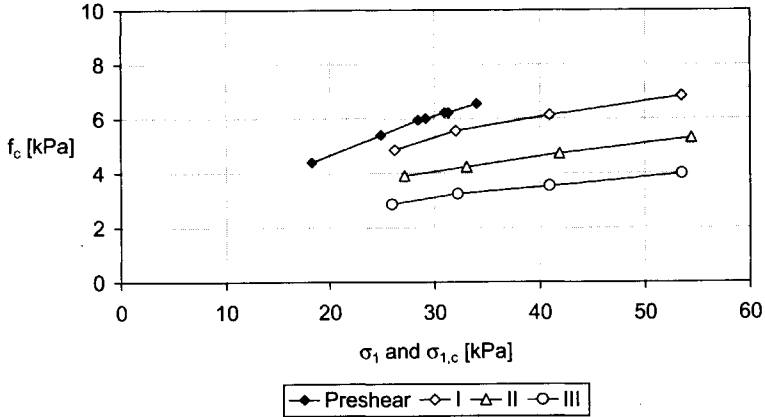


Figure 5.6: Flow function according to the Jenike procedure including preshear (Preshear); flow function with different types of consolidation without preshear (the numbers refer to figure 5.5) (Schwedes and Schulze, 1990).

Saraber et al. (1991) also used a biaxial tester to measure the flow function, but the procedure was different to Harder's in that a preshear step was included. The anisotropy was investigated in the last step: the determination of the unconfined yield strength. The experiment was performed with the major principal stresses of both the preshear step and the shear step in the same direction or perpendicular to each other (see figure 5.7). That means the major principal stress has rotated over an angle of 90 degrees.

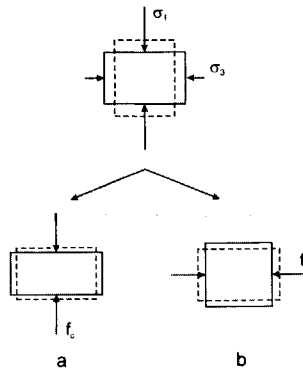


Figure 5.7: Procedure for the determination of the unconfined yield strength in a biaxial tester. Major principal stress in the same direction for both steps (a) and rotated 90 degrees for the measurement of the unconfined yield strength (b) (Saraber et al. 1991).

Saraber et al. (1991) concluded that the flow function of a finely ground limestone ( $d_p < 10 \mu\text{m}$ ) decreases if the direction of the major principal stress is rotated compared to the preshear situation (figure 5.8).

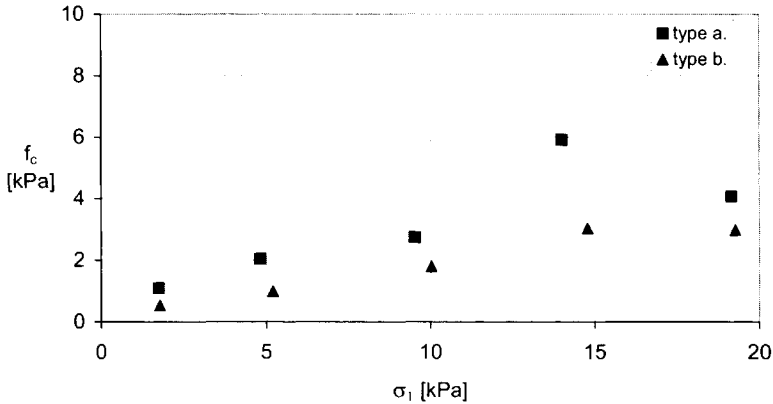


Figure 5.8: Flow function for finely ground natural limestone ( $d_p < 10 \mu\text{m}$ ) measured in a biaxial tester with two procedures (according to figure 5.7) (Saraber et al., 1991).

The experiments performed by Wong and Arthur (1985) on inherent and induced anisotropy in dense Leighton Buzzard sand (600-850  $\mu\text{m}$ ) are unique. For the investigations the Directional Shear Cell (DSC) has been used (see chapter 2). The DSC can apply normal stresses as well as shear stresses and by varying these stresses the principal stress direction can be controlled.

The experiments of Arthur et al. (1972, 1977) and Wong and Arthur (1985) demonstrate the degree of anisotropy which exists at a given moment (called stress path A) by unloading the sample with constant principal stress directions until  $\sigma_1' = \sigma_3'$  and then reloading with a change in major principal stress direction which is again held constant (called stress path B). The stress-strain behavior of this sample can then be compared with another sample subjected to an identical stress path and then reloaded with no change in principal stress direction.

A separation of the effects of inherent and induced anisotropy is achieved because the DSC is essentially a plane strain device and samples can be rained in the direction normal to the plane of strain to achieve initial isotropy in this plane (figure 5.9a). For inherent anisotropy the samples can be rained in the  $y$  direction. The angle  $\delta$  describes the direction of the major principal stress during the experiment with respect to the deposition direction for an inherently anisotropic sample (figure 5.9b).

The DSC can align the major principal stress at any angle to the sample cube within 90 degrees between the  $x$  and  $y$  axes shown in figure 5.9c.  $\psi$  defines the chosen angle of the major principal stress for step A or B in the procedure.  $\Delta\psi$  gives the change in direction of the major principal stress from step A to step B. The direction of the major principal strain increment is given by  $\xi$  (figure 5.9b).

Wong and Arthur (1985) showed that initially isotropic samples develop induced anisotropy in path A, the degree of which depends on the magnitude of the strain in this path. This experiment shows that anisotropy already forms in the stage before steady-state shear is reached. The Jenike Tester experiments (figure 5.2) prove that the anisotropy also exists when steady-state shear has been reached.

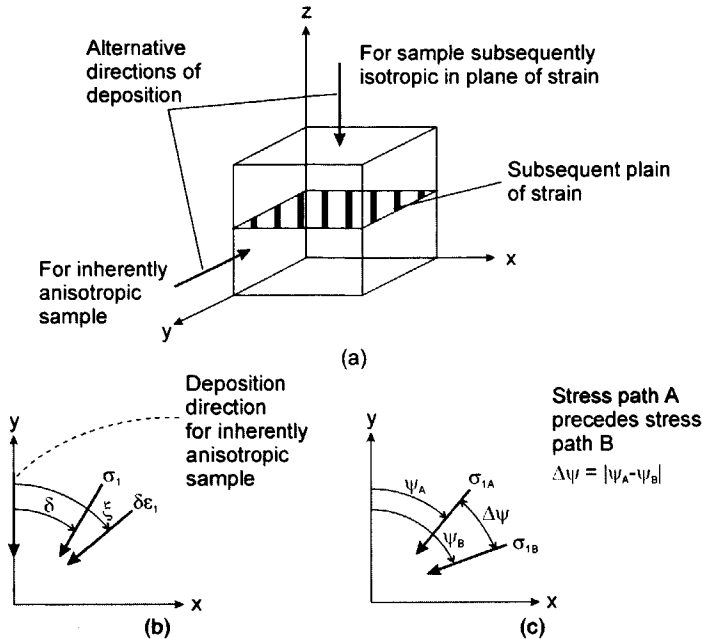


Figure 5.9: Sample orientation (a and b) and direction of the major principal stress (c) for measurement of anisotropy in the DSC (Wong and Arthur, 1985). The angles are defined in the text.

Wong and Arthur also looked at the influence of the change of the direction of the major principal stress ( $\Delta\psi$ ) between path A and B. Generally, the sample is weaker when  $\Delta\psi$  increases. However, for  $\Delta\psi = 70^\circ$  the sample gave a weaker response than with  $\Delta\psi = 90^\circ$ . The explanation for this unexpected behavior is that the rotation of strain increment axes during stress path B for the sample tested with  $\Delta\psi = 70^\circ$  at first align with the softest direction in the sample which is defined by the angular distribution of contacts achieved at the end of stress path A. From this suggestion of Wong and Arthur one can deduce that there is a tendency of the principal axes of stress and strain increment to reach coincidence.

The existence of inherent anisotropy is shown by samples which are weaker when the angle of the major principal stress to the direction of deposition ( $\delta$ ) increased (Arthur et al. 1981). The conclusion is drawn that the initial angular distribution of the particle contacts causes this response.

In conclusion, Wong and Arthur (1985) investigated how the induced anisotropy will be superimposed on the existing inherent anisotropy. A rather large initial strain was imposed by stress path A and by rotating the major principal stress in path B the sample strength shows similar behavior as for the induced anisotropy experiments: a larger change in the direction of the major principal stress weakens the sample. Even after considerable strain in path A and thus considerable induced anisotropy, the inherent anisotropy still influences the results in stress path B. In figure 5.10 the failure of the sample is represented by  $\phi_f$  (equation 5.1) and it can be seen that the failure still depends on the angle between the direction of the major principal stress

and the direction of deposition ( $\delta$ ). This survival of inherent anisotropy is attributed to a very limited change in the angular distribution of particle orientation during strain.

$$\sin \phi_f = \frac{\sigma_1 - \sigma_3}{\sigma_1 + \sigma_3} \quad (5.1)$$

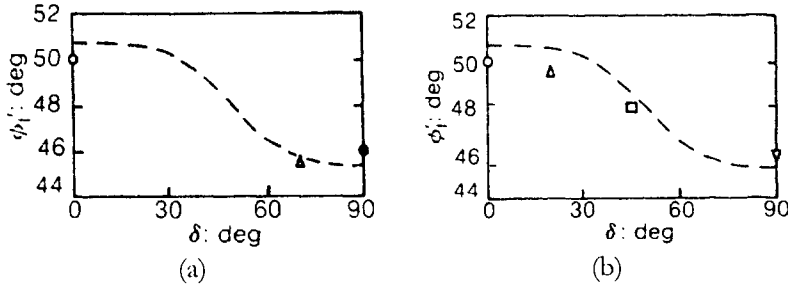


Figure 5.10: Failure of samples with inherent anisotropy (a) and with inherent and subsequent induced anisotropy (b) (Wong and Arthur, 1985).

Li and Puri (1996) investigated four powders (table 5.1) on their inherent anisotropic behavior occurring from a plunging and a tapping filling method using a cubical triaxial tester. The types of test performed are a hydrostatic triaxial loading up to 190 kPa followed by unloading, and a so called conventional triaxial test in which two principal stresses are kept at a fixed value of 34.5 kPa and the third principal stress increases until failure occurs.

Table 5.1: Powders investigated by Li and Puri (1996)

	Irregular shape	Rounded
Cohesive	wheat flour	potato starch
Cohesionless	milled glass fibers	glass beads

Wheat and glass beads showed no anisotropy, starch showed some anisotropy and milled glass fibers showed significant anisotropy. Li and Puri (1996) concluded that the reason why wheat flour and in a certain extent also starch showed no or little anisotropy, is the cohesiveness which prevents a preferred particle orientation to occur during the deposition. The cohesion forces keep particles together so that they cannot rotate freely with respect to each other. They also concluded that the degree of anisotropy tends to decrease with the roundness of particles, being the most extreme with milled glass fibers.

### 5.3 Microscopic view on anisotropy

In the former paragraphs evidence of anisotropic behavior of granular material is presented. These works concentrated on observation of anisotropy and the special behavior it causes. Less work is done on the microscopic explanation of anisotropy. In general it is agreed that granular material forms a structure that causes the anisotropy.

In the area of soil mechanics the structure is often defined by the contact structure between the particles (Oda, 1972).

Arthur et al. (1986) explain the formation of structure in non-cohesive granular materials as particle contacts that are continually made and broken during strain deformation. The angular distribution of normals to particle contacts changes anisotropically, with the maximum and minimum number of contact normals corresponding to major and minor principal strain directions. Subsequent shear of the sample does not change the alignments easily.

In the area of powder technology not much work has been done on anisotropy and even less on the microscopic explanation. Maltby et al. (1995) conclude that steady-state consolidation probably leads to the highest degree of anisotropy, with the greatest strength in the direction of the major principal stress and the lowest strength in the direction of the minor principal stress. Feise (1998) was the first to give a review of experiments on induced anisotropy in cohesive powders. Feise put forward the idea of a favorable structure. Cohesive bulk solids form loose packings with a fairly high porosity. When such a packing is deformed, it develops into a packing structure that gives maximum resistance against this type of deformation. After a change to a different strain path direction, this structure will disassemble. Depending on the type of deformation, a new maximum resistance structure is built up after a change in the strain path direction.

It is clear that some kind of structure in cohesive powder causes the effect of anisotropy. This structure can be translated into the contact point structure between the particles. For larger particles like sand this description may be sufficient to describe anisotropic behavior as the work of Wong and Arthur (1985) has shown. However, for smaller particles cohesive forces are larger and it is believed that the contact structure is of less importance and the distribution of the porosity plays a more important role. The inhomogeneity of the bulk density is, however, a very difficult parameter to measure.

## **5.4 Measurement of anisotropy with the Flexible Wall Biaxial Tester**

In this paragraph the FWBT is used to investigate the occurrence of anisotropy in cohesive powder. As mentioned in paragraph 5.2.1 two types of anisotropy can be distinguished: inherent and induced anisotropy. Here, induced anisotropy is investigated and it is assumed that the sample is homogeneous after filling so no inherent anisotropy exists in the sample. This assumption holds for the xy plane because no direction dependent behavior of the powder after a biaxial consolidation has been observed.

Anisotropy is induced in the powder by two steps that are also used in the determination of the flow function: consolidation and preshear. These two steps create a certain directional structure in the powder. This structure determines the reaction of the powder to different types of deformation that are applied in a third step. The deformations in step three are applied with the same constant volume as in

the preshear step. According to the critical state concept (Roscoe et al. 1958, Jenike 1961, Schwedes 1996), the same steady-state condition should be reached.

All the experiments described in this section have been performed in a strain controlled mode with a strain rate of  $1.0 \cdot 10^{-5} \text{ s}^{-1}$  for the fastest wall. The rates of other walls adapt to this strain rate in order to keep the volume constant.

### 5.4.1 Preparation of the sample

Each strain controlled anisotropy experiment started with the same two preparing steps consisting of an initial consolidation (step 1), in which the volume is reduced with a chosen percentage, and a preshear step (step 2) with constant volume. The strain paths for these steps are given in figure 5.11.

The consolidation step and the preshear step have been discussed in chapter 4. The following sections focus on the third step.

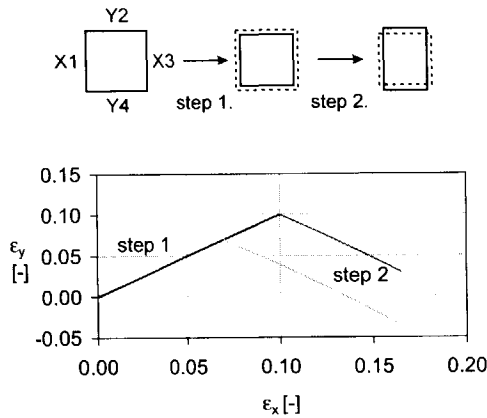


Figure 5.11: Strain path for the consolidation (step 1) and the preshear (step 2). The dotted lines in the figure at the top represent the starting position for that step.

### 5.4.2 Rotation of the principal axes of strain

The first two deformations that will be discussed, have been labeled type I and II. They show the reaction of the powder to a  $90^\circ$  rotation of the direction of the major principal strain. In type I the walls that were moving inwards (X1 and X3 in figure 5.12) during the preshear step, move outwards in the third step. The volume will be kept constant by moving the other two walls inwards (Y2 and Y4 in figure 5.12). Experiments of type II do the opposite in step 3, which means that the type of deformation compared to step two does not change (figure 5.12).

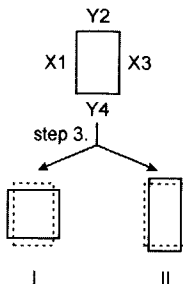


Figure 5.12: Deformation types I (strain in opposite direction as during preshear) and II (strain in same direction as during preshear). The volume remains equal for both types.

The applied absolute strains are given in table 5.2 for biaxial consolidations with a total volume reduction of 13.5 % and 19 %. In the successive preshear steps a larger strain is applied for the volume reduction of 13.5 % in the consolidation step. Typical experiments can be found in the Appendix of this chapter.

Table 5.2: Overview of the applied absolute strains (relative to the starting volume of sample) in the experiments I and II. Total volume reduction of 13.5 % (top set) and 19 % (bottom set).

strain [-]:	consolidation	preshear	I	II
X1	0.07	0.164	-0.094	0.243
Y2	0.07	-0.034	0.210	-0.142
X3	0.07	0.164	-0.094	0.243
Y4	0.07	-0.034	0.210	-0.142
X1	0.10	0.165	-0.164	0.304
Y2	0.10	0.030	0.304	-0.164
X3	0.10	0.165	-0.164	0.304
Y4	0.10	0.030	0.304	-0.164

The results of step 3 are given in figure 5.13 and 5.14 for the consolidations of 13.5 % and 19 % respectively. The stress paths are presented as the deviatoric stress versus the relative strain of the side of the sample that decreases in length: for the type I deformation  $\epsilon_y$  is used and for type II deformation  $\epsilon_x$ . The mean stress paths behave similarly to the deviatoric stress paths. Because the difference between type I and II only arises after application of both a consolidation step and a preshear step and not after application of only the consolidation step, the preshear step is the important cause for the anisotropy.

In the preshear step steady-state should be reached because the volume is constant and the applied strain is long (relative to for example the Jenike Tester). It has already been remarked that steady-state shear is sometimes not perfectly reached in the FWBT. The stresses keep changing over long strain deformations. In figure 4.38 it has been shown that the steady-state values that are reached, are proportional to the maximum consolidation stress at the end of the consolidation path. Therefore, the deviatoric stresses at preshear are different for a volume reduction of 13.5 % and 19 % (figure 5.13 and 5.14). The type II deformation gives the same steady-state value as



during preshear. For the experiment with an initial volume reduction of 13.5 % the stresses have been brought back to zero before step 3 started. During step 3 they increase very quickly to the value that was reached in the preshear step. In the experiment with an initial volume reduction of 19 %, the stresses have not been brought back to zero between step 2 and step 3.

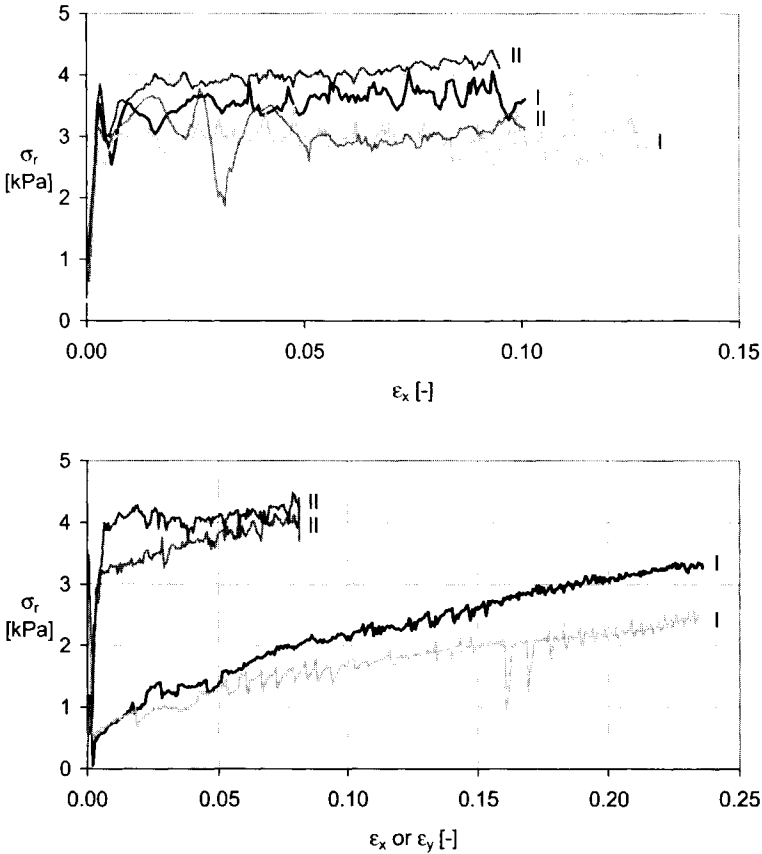


Figure 5.13: Preshear (top) and shear (bottom) of type I and II experiments with a 13.5 % volume reduction.

The type I deformation experiments show that the deviatoric stress drops to almost zero and slowly increases again with increasing strain. Approximately the same value of the deviatoric stress as in the preshear step is reached after a strain of 15 to 20 % in the y direction. This effect occurs for both consolidations and is clearly anisotropic behavior of the BCR-limestone. The powder is much weaker in the direction perpendicular to the direction in which the major principal strain is applied during the preshear step. One could say that after the preshear step the powder is critically consolidated in the direction of the major principal strain and underconsolidated in the direction of the minor principal strain. The terms "underconsolidated" and

"critically consolidated" are now direction dependent. A direct consequence of these results is that the flow properties of a powder can be manipulated by choosing the direction in which stress or strain is applied.

During the consolidation and preshear step a certain structure has been formed in the powder, which adapted itself to the combination of the x walls moving inwards and the y walls moving outwards. Feise (1996) calls this a favorable structure for this type of shear. In the x direction the weak spots in the powder have been removed up to a certain extent. In the y direction this has not or only partly occurred. This structure explains why the stresses decrease when the direction of movement of the walls is turned. In a loose cohesive powder these weak spots are places in the material where the porosity is relatively high. Because the major principal strain is directed, the places which are easily destroyed by that strain will vanish. This causes a direction dependency.

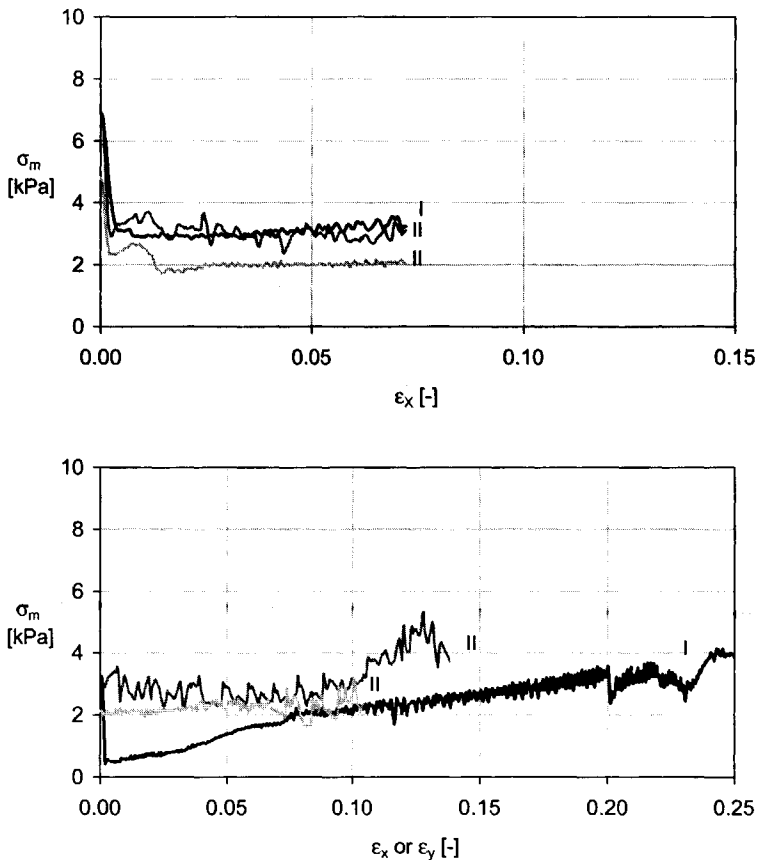


Figure 5.14 Preshear (top) and shear (bottom) of type I and II experiments with a 19 % volume reduction.

It is believed that the mechanism that causes the structure is different in cohesive powder from that in coarser materials (e.g. sand) in which the orientation of the contacts between the particles causes the direction dependency. The idea is that particles in cohesive powder will form clusters which deform and move as a whole. Therefore, it is more the inhomogeneity of the bulk density, that is the spacing between the particles, than the orientation of the contacts that determines the anisotropic behavior. It is difficult to estimate the size of the clusters that particles would form. Maybe the cluster size adapts itself to the geometry of the test volume. It can be an important parameter in relation to the size of shear testers. This idea needs further research.

### 5.4.3 Six other deformations

The occurrence of induced anisotropy is clearly shown by deformation types I and II in cohesive BCR-limestone. In this section the behavior of the powder is investigated with six other types of deformation after the application of a consolidation and a preshear step. The six types differ from type I and II in that one or two walls are not moving (figure 5.15). The volume remains constant during these steps as in deformation types I and II. If the powder behaves homogeneously these types should not differ from types I and II.

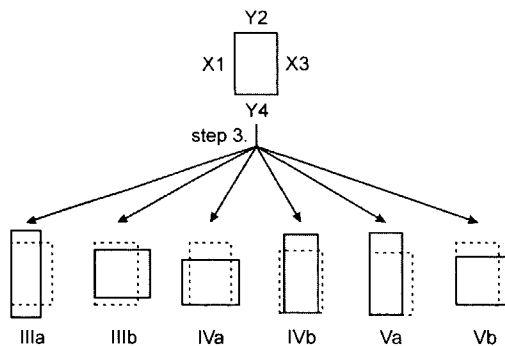


Figure 5.15 Six types of deformation for which the volume is kept constant. The dotted lines represent the starting position of the step.

Deformation types IIIa, IVb and Va are in fact a modified type I deformation. Type IIIb, IVa and Va are modified type II deformations. In the type III deformation wall X1 doesn't move and X3 moves inwards (IIIa) or outwards (IIIb). In type IV wall Y4 doesn't move and Y2 moves inwards (IVa) or outwards (IVb). In type V wall X1 and Y4 don't move and X3 moves inwards (Va) or outwards (Vb). The precise values for the applied strains can be found in table 5.3. Typical experiments of each type can be found in the Appendix of this chapter.

Table 5.3: Overview of the applied absolute strains (relative to the starting volume of the sample) in the experiments IIIa to Vb. Total volume reduction of 13.5 % (top set) and 19 % (bottom set).

strain [-]:	consolidation	preshear	IIIa	IIIb	IVa	IVb	Va	Vb
X1	0.07	0.164	0.164	0.164	0.035	0.206	0.164	0.164
Y2	0.07	-0.034	-0.081	0.104	0.242	-0.145	-0.145	0.236
X3	0.07	0.164	0.236	-0.094	0.035	0.206	0.249	-0.088
Y4	0.07	-0.034	-0.081	0.104	-0.034	-0.034	-0.034	-0.034
X1	0.10	0.165	0.304	0.136	0.028	0.229	0.267	-0.110
Y2	0.10	0.030	-0.059	0.176	0.030	0.030	0.030	0.030
X3	0.10	0.165	0.165	0.165	0.028	0.229	0.165	0.165
Y4	0.10	0.030	-0.059	0.176	0.304	-0.130	-0.096	0.304

All the experiments shown here are performed in a strain controlled manner with a strain rate of  $1 \cdot 10^{-5} \text{ s}^{-1}$ . For these particular experiments that means that the strain rate is defined for one wall: for type III that is wall X3, for type IV that is wall Y2, and for type V that is wall X3. The other walls adapt in order to keep the volume constant at all time. Due to the physical limitations of the FWBT, the applied strain is larger in the third step for experiments IIIb, IVa and Vb.

Figures 5.16 and 5.18 show the preshear steps for samples that were consolidated with a volumetric strain of 13.5 % and 19 % respectively. In most cases some kind of steady-state is reached. The third step is presented in figures 5.17 and 5.19. The deviatoric stress is presented versus the relative strain of that side of the sample that decreases in length. For the experiments in which the direction of movement of the walls turns around (IIIb, IVa and Vb), this is  $\epsilon_y$ , for the other types (IIIa, IVb and Va) this is  $\epsilon_x$ .

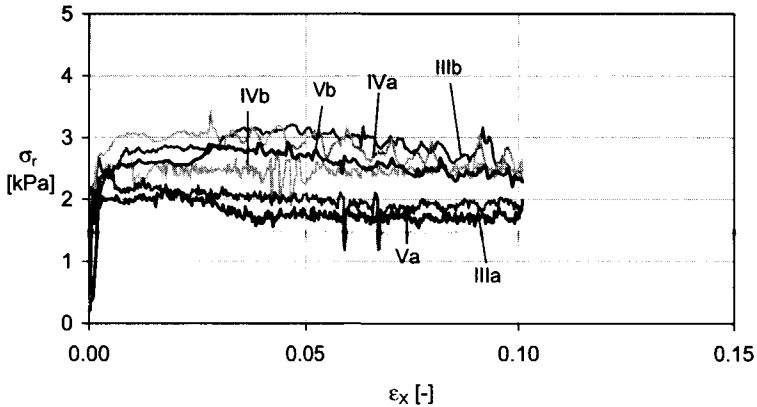


Figure 5.16 Results for types IIIa to Vb experiments (13.5 % volume reduction): preshear.

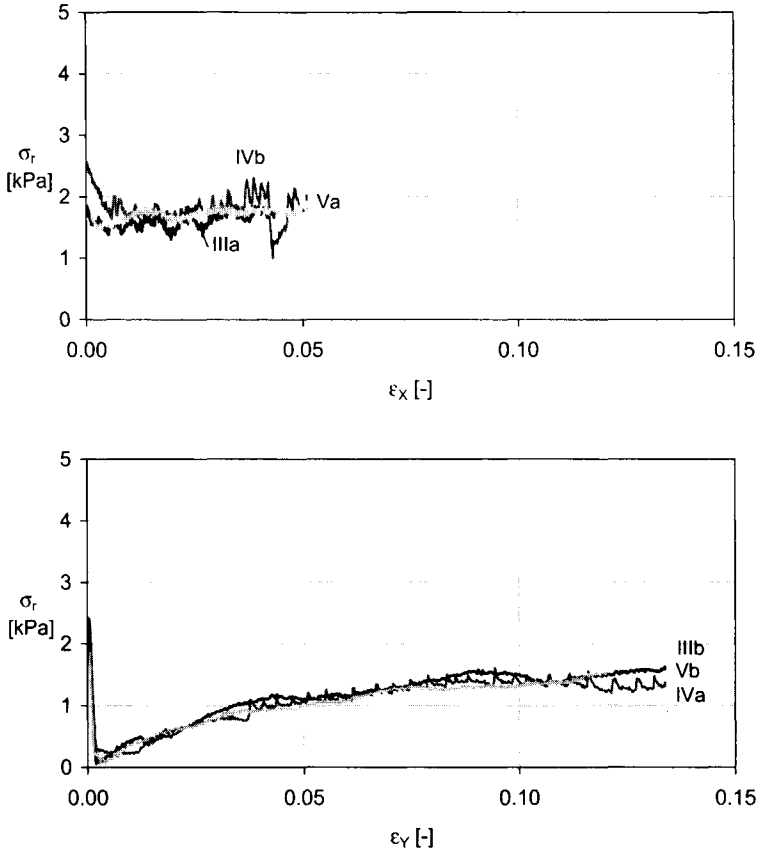


Figure 5.17 Results for types IIIa to Vb experiments (13.5 % volume reduction): shear.

The deviatoric stress paths of the six types of deformation can be divided into two groups that react similarly as deformation type I or II. The stress path of types IIIa, IVb and Va stay at approximately the same value as has been reached in the preshear step. The deviatoric stress of the deformation types IIIb, IVa and Vb drops to almost zero and then increases very slowly up to the value that has been reached in the preshear step. All three types show the same rate of increase. The same reaction as for the type I and II experiment is seen here. The powder is weaker in the direction perpendicular to the direction of the major principal strain in the preshear step.

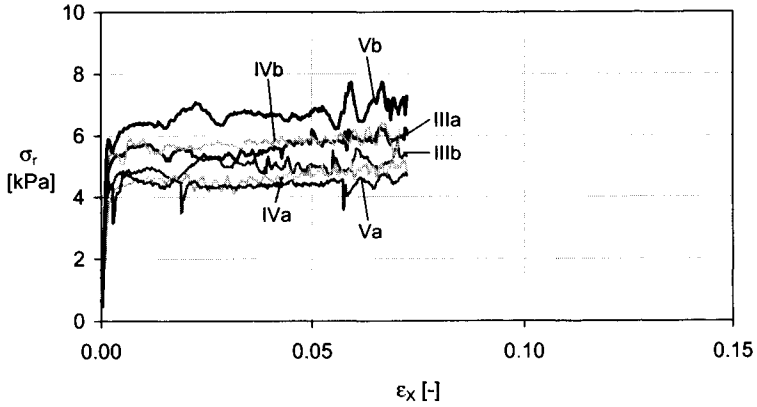


Figure 5.18 Results for type IIIa to Vb experiments (19 % volume reduction): preshear.

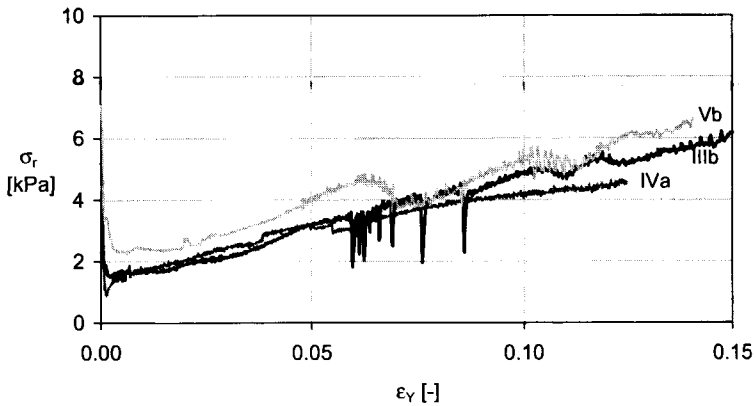
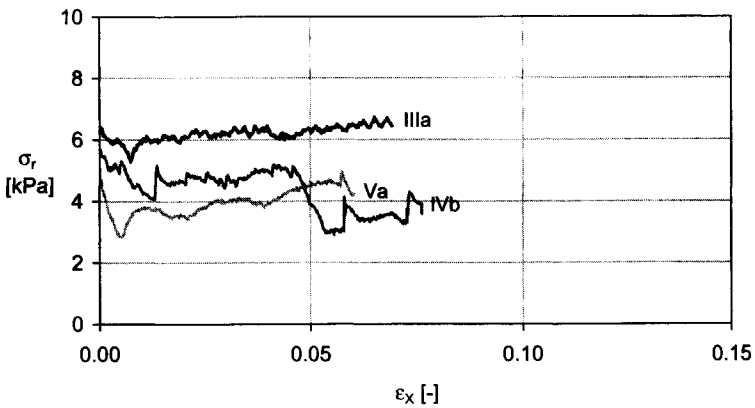


Figure 5.19 Results for type IIIa to Vb experiments (19 % volume reduction): shear.

In figure 5.20 the normal stresses for step 3 are given for the different deformation types IIIa to Vb (volume reduction 19 %). At the moment the third step starts, the stress paths react. In the type IIIa experiment the normal stress on X3 increased relative to X1. The same happened in experiment Va. In experiments of type IVa and Vb the Y2 normal stress increased relative to the Y4 normal stress. No similar effects have been observed in experiments of type IIIb and IVb. The observations that are reported here, are based on 5 to 10 experiments of each type. It should be remarked that the differences in the normal stress of opposite walls partly also occurred during the preshear step and are prolonged during the shear step. However, especially experiments of type IIIa and Va did show a clear drop of the X1 normal stress relative to the X3 stress at the start of the third strain step.

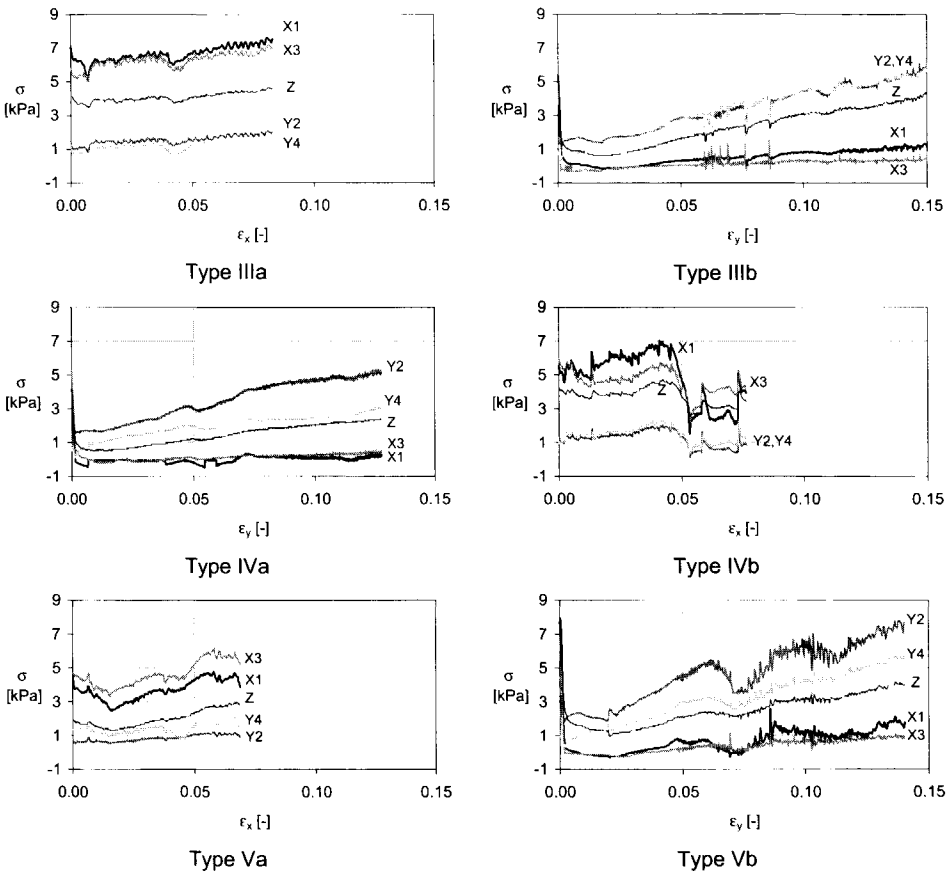


Figure 5.20: Normal stresses during step 3 for experiments of type IIIa to Vb experiments (19 % volume reduction).

In order to check whether the membrane deformation has an influence on the behavior of the powder and on the observed differences between normal stresses on opposite walls, experiments of type Va have been repeated with an imposed

membrane deformation of 200  $\mu\text{m}$  on each membrane. This had no visible effect on the trend of the experiments. Because the membrane deformations are usually about 10  $\mu\text{m}$ , it is concluded that the membrane deformation has no effect on the reaction of the powder to the different deformation types.

The difference in the normal stresses on opposite walls indicates that there are shear stresses. The shear stresses work between the membranes and the powder. The configuration of the side wall membranes is such that they deform homogeneously and if the powder would deform homogeneously as well, no shear stress should appear. The friction between the top and bottom membrane is reduced to a minimum by the application of a lubricant (figure 4.14).

In the former section the idea of a favorable structure (Feise, 1996) has been introduced. This structure is thought to exist due to the direction dependent elimination of weak spots in the powder. This process occurred in the consolidation and preshear steps of these experiments. During the preshear the sample is strengthened in one direction, while the other direction did not experience a direct strengthening. When the strain is applied from just one wall as in the deformation types in figure 5.15, the favored structure that has been built up during the preshear has to adapt to the new deformation type. If the powder would behave perfectly homogeneously the stresses would be the same on opposite sides. However, the fact that shear stresses arise, indicates that the powder behaves inhomogeneously.

All deformation types show that the stresses tend to increase to the value that has been reached during the preshear step. However, the strain needed for that can be very large and some stresses keep on increasing. It could be that the changing shape of the sample volume influences the powder because the shear pattern that occurs has to change as well. If the steady-state stresses are not equal to the value as has been reached during preshear, the critical state is not unique for a certain bulk density. However, the experiments in this section did not reach steady-state yet and no conclusion can be made about the critical state.

#### **5.4.4 Shear planes**

The different reaction of the powder to the type I and II deformation (figure 5.12) can also be seen in the crack patterns that form when the tester is opened after the experiment (figure 5.21).

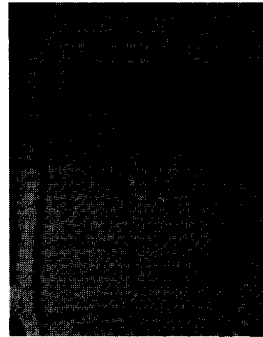
About 20 experiments have been visually inspected and it is concluded that in the type II experiments a long crack travelling from wall to wall tends to arise. This crack has a direction perpendicular to the direction of the major principal strain in the last step (step 3) and is positioned halfway the sample. Type I experiments did not have this tendency. The photos of the experiments with the other six types of deformation did not show a recognizable pattern.

It is assumed that the cracks are positioned at the places where the powder is the weakest, which are the places where the shear planes were in the shear step. As remarked before, no clear pattern in the supposed shear planes has been found for the different type of experiments.

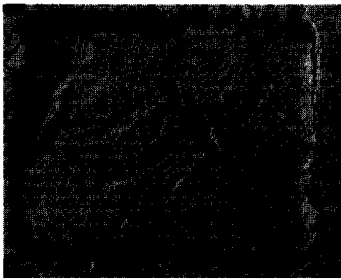




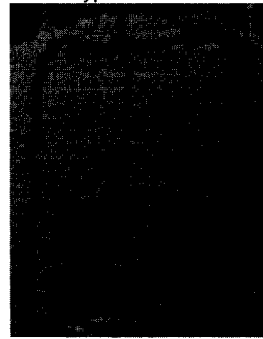
Type I: 11.6%



Type II: 11.6%



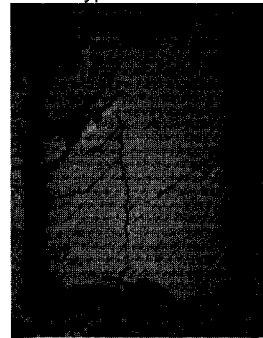
Type I: 13.5%



Type II: 13.5%



Type I: 19%



Type II: 19%

Figure 5.21: Photos of the anisotropy experiments as described in figure 5.12. Wall X1 is on the left and Y2 on the bottom of all pictures.

## 5.5 Principal axes of stress and strain

The experiments described in section 5.4.3 are performed in a strain controlled mode. Thus, the axes of the tester are the principal axes of strain. In the recorded stress paths, differences between the normal stresses on opposite walls have been observed. These differences are shear stresses between the membranes and the powder. The existence of these shear stresses without shear strains being applied, indicates that the principal axes of stress could locally not be aligned with the axes of the tester and with the principal axes of strain.

Jenike (1961, 1964) assumes the principle of coaxiality in his procedure which states that the principal axes of stress and strain are coincident. It is equivalent to saying that there can be no shear stress on planes on which there is no shear strain (Nedderman, 1992).

Wong and Arthur (1985) have reported non-coaxiality for sand samples (see paragraph 5.2.3). They attribute anisotropic behavior of the samples to the distribution of particle orientation. An initial distribution in a sample defines the initial principal axes of strain that do not have to be aligned with the principal axes of stress. In all experiments, however, the principal axes of strain rotate in favor of the existence of coaxiality. Joer et al. (1993) confirms the phenomenon of non-coaxiality in a two dimensional sample. Allersma (1982) observed optically significant deviation between the major axes of stress and strain increment.

A hollow cylindrical torsional shear apparatus which allows independent control of axial force, torque, and inner and outer cell pressures has been used by Pradel et al. (1990) and Gutierrez et al. (1991) to apply a stress rotation with constant principal stress values to Toyoura sand. They concluded that coaxiality only occurred when the principal axes of stress are fixed. The deviation between the two sets of principal axes became smaller with increasing shear stress level, and finally reached coaxiality when the sample failed.

The work reviewed above is all done in the area of soil mechanics. As far as known, there are no similar conclusions for cohesive powders so far. The experiments in the FWBT do not prove the existence of non-coaxiality, but it is likely that non-coaxiality exists locally due to the inhomogeneous behavior. However, this topic needs further research in specialized testers like the DSC (Arthur et al. 1981).

## **5.6 Anisotropic flow function**

In this paragraph the influence of induced anisotropy on the flow function is investigated. The flow function of BCR-limestone is measured according to the procedure described in figure 4.53 with one difference: the last step applies the major principal stress in the direction perpendicular to the direction of the major principal stress in step 2. The unconfined yield strength is measured at a 90° angle with respect to the normal unconfined yield strength measurement. This strength will be called the anisotropic unconfined yield strength. This procedure has also been used by Saraber et al. (1991). The consolidation and preshear step are similar to the ones for the normal flow function measurement in chapter 4 and will not be given here.

In figure 5.22 the anisotropic flow function is given together with the regular flow function as measured with the FWBT (also table 5A.1). The anisotropic flow function is lower than the normal flow function. The stress paths and the volume of the sample during the determination of the anisotropic unconfined yield strength are given in figure 5.23.

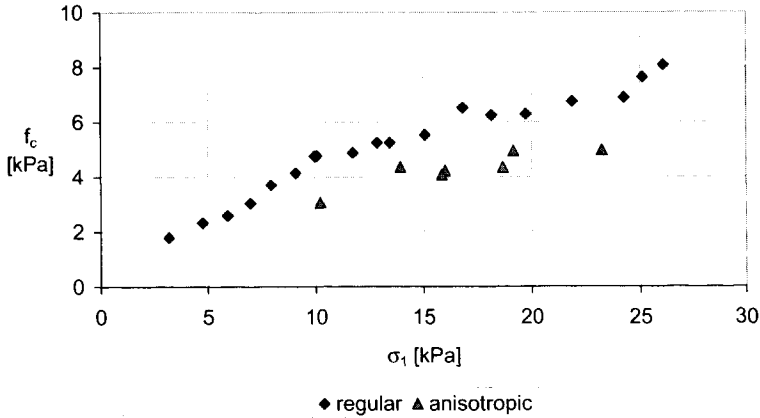


Figure 5.22: Flow function of BCR-limestone measured with the FWBT: regular and anisotropic.

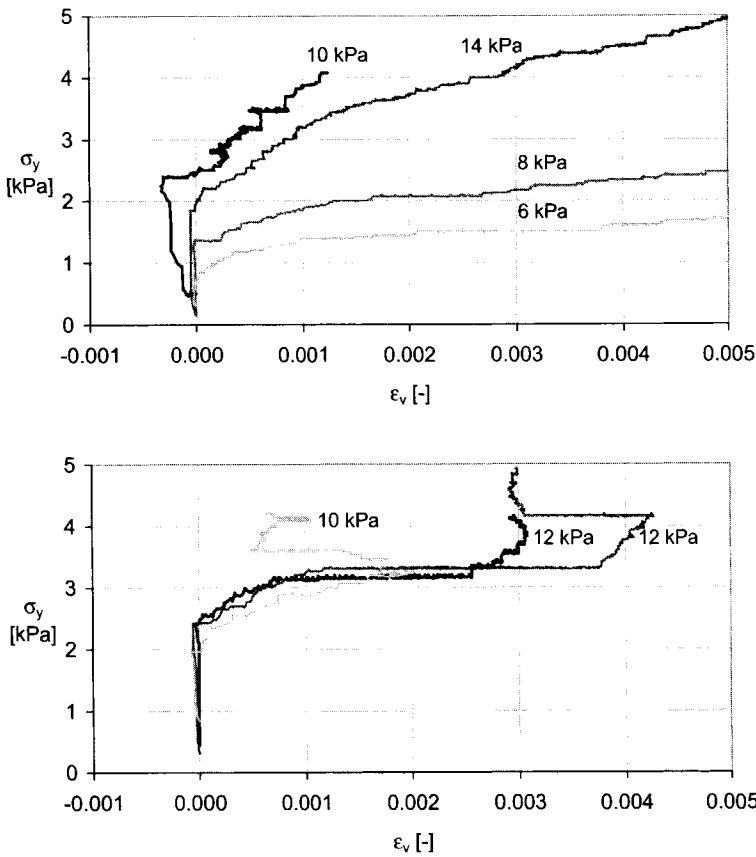


Figure 5.23: Determination of the anisotropic unconfined yield strength for different consolidations (values on the right are consolidation).

The anisotropic determination of the flow function is characterized by a much slower rise of the normal stress compared to the regular procedure for the flow function. Some stress paths proceed in steps (figure 5.23 bottom) in which the stress remains constant as a function of the strain deformation. At a certain level the stresses start increasing again. These steps are due to corrections of the membrane deformations that had to be corrected before the stress could be increased any further. Dilatancy does not occur, which indicates that the powder is not critically consolidated.

These observations give rise to the question whether the measured endpoint of the stress path should be called unconfined yield strength. The powder is in some kind of underconsolidated state for the direction in which the stress is applied in the last step of the procedure caused by the consolidation and preshear step.

The powder is weaker if the direction of the principal axes is rotated over  $90^\circ$  compared to the flow function without rotation. It is likely that the normal flow function is the highest possible flow function and that any rotation of the principal stresses will cause a lower flow function. This means that the flow function as measured with the Jenike Tester produces the highest possible flow function.

The results of Saraber et al. (1991) have the same trend compared to figure 5.22, but the flow functions were lower. This is due to the fact that two different powders were under investigation: natural limestone ( $d_p < 10 \mu\text{m}$ ) and BCR-limestone ( $d_p = 4.3 \mu\text{m}$ ). However, Saraber et al. (1991) use the Postec Flexible Wall Biaxial Tester (chapter 2) and, it is not completely clear how the unconfined yield strength has been measured. Maltby (1993) uses a procedure, as described in chapter 4, that does not measure the same unconfined yield strength. It is not clear whether Saraber et al. use the same procedure. That could be another explanation for the difference between the results of Saraber et al. and figure 5.22.

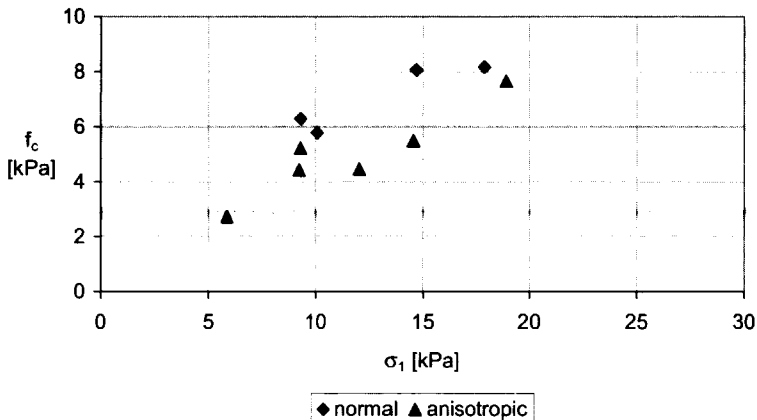


Figure 5.24: Regular and anisotropic flow function of Avicel MCC PH 102 measured with the FWBT.

The difference between the regular and the anisotropic flow function has been found as well with Avicel PH 102 microcrystalline cellulose (MCC) (figure 5.24). This is a product designed primarily for pharmaceutical solid dosage formulations. This

material appears to be less cohesive, mainly due to its larger particle size ( $d_p = 90 \mu\text{m}$ ), than BCR-limestone. The change of the direction of the major principal stress results also for this powder in a lower unconfined yield strength. Again the structure that formed is the reason for the lower flow function, but this structure probably exists in this case of the contacts between particles. The shape of the highly fiber-like particles very likely plays an important role.

## 5.7 Conclusion

Anisotropy has been shown to be a powder property that is not included in the current powder flow theory. It is proven that this is due to the structure that can form in powder. In literature (Wong and Arthur, 1985) it is shown for non-cohesive sand that both inherent and induced anisotropy have a large effect on the flow behavior.

In this chapter it is shown by means of the Flexible Wall Biaxial Tester that anisotropy occurs in cohesive powder as well. It is concluded that during a preshear step in which the volume of the sample remains constant a certain structure originates in the powder that is favorable for that type of deformation. This structure consists of inhomogeneity of the bulk density of the powder in contrast to non-cohesive sand in which the number of contacts is thought to be the main component that forms the structure. The inhomogeneity of the bulk density is thought of as the spacing between the particles that can vary in different directions. The porosity is not a good parameter to describe the structure because it is a scalar.

The second observation from these experiments is that it is doubted whether the principal axes of strain are in the same direction as the principal axes of stress at every position in the powder. This observation is known in literature for non-cohesive sand (Joer et al. 1998). To prove the existence of non-coaxiality a specialized tester is needed.

The influence of anisotropy on the flow function has been investigated by changing the direction in which the unconfined yield strength is measured with 90 degrees with respect to the major principal stress during the preshear step. It appears that the powder is much weaker in this direction resulting in a lower flow function. In fact the powder reacts as being underconsolidated. This result makes it possible to manipulate the flow properties of powder just by changing the direction in which the major principal stress is applied. The effect of anisotropy on the flow function is shown for both BCR-limestone and for MCC PH 102.



# Appendix

## 5A.1 Type I, II, IIIa, IIIb, IVa, IVb, Va and Vb experiments

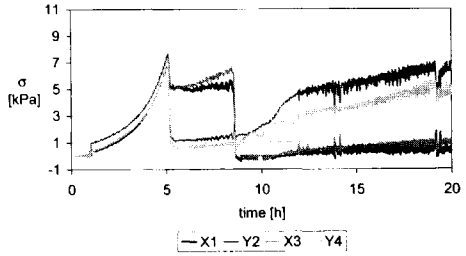
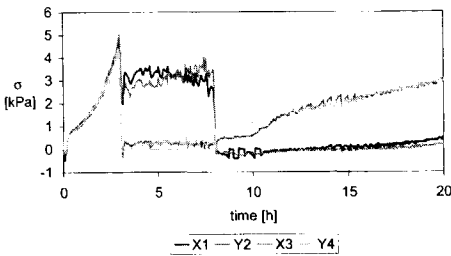


Figure 5A.1: Type I experiment: 13.5 % (left) and 19 % (right) volume reduction.

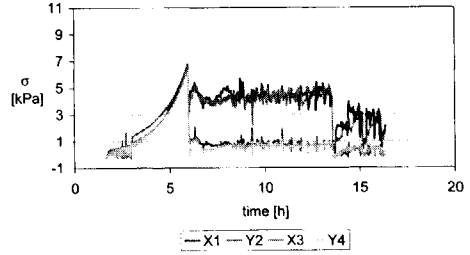
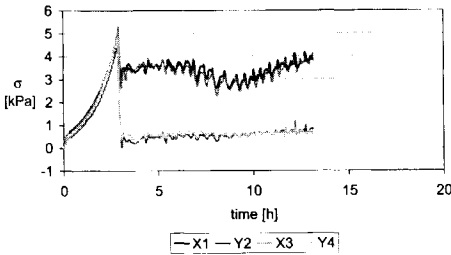


Figure 5A.2: Type II experiment: 13.5 % (left) and 19 % (right) volume reduction.

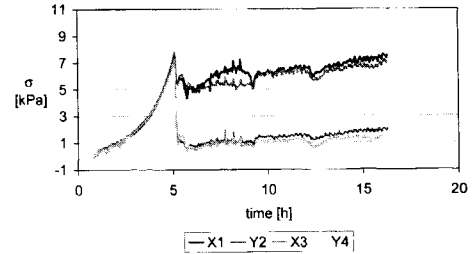
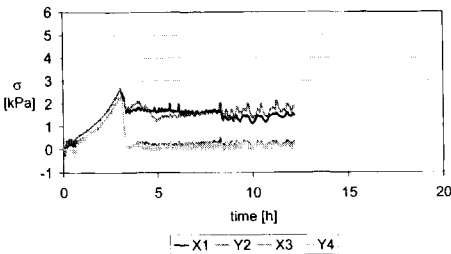


Figure 5A.3: Type IIIa experiment: 13.5 % (left) and 19 % (right) volume reduction.

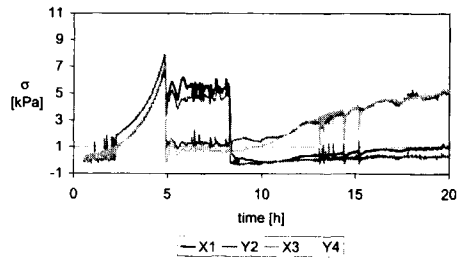
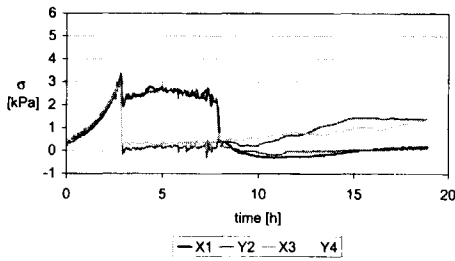


Figure 5A.4: Type IIIb experiment: 13.5 % (left) and 19 % (right) volume reduction.

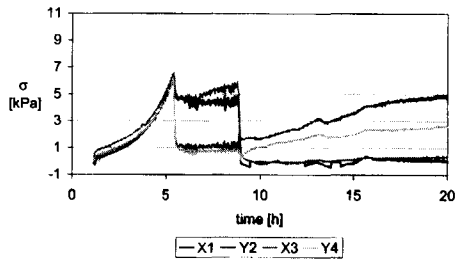
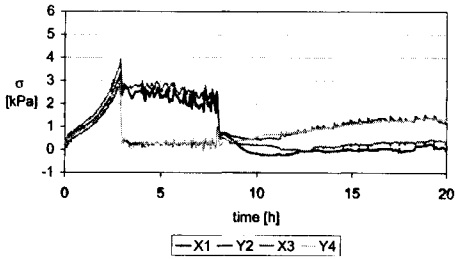


Figure 5A.5: Type IVa experiment: 13.5 % (left) and 19 % (right) volume reduction.

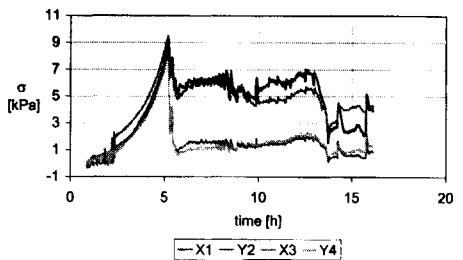
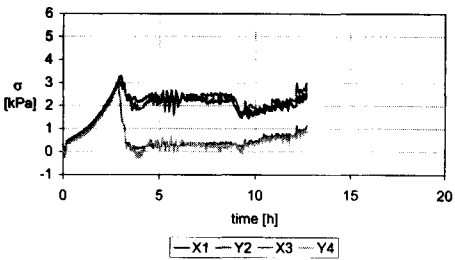


Figure 5A.6: Type IVb experiment: 13.5 % (left) and 19 % (right) volume reduction.

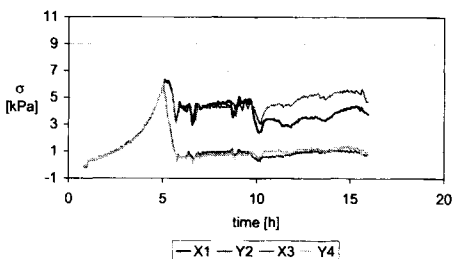
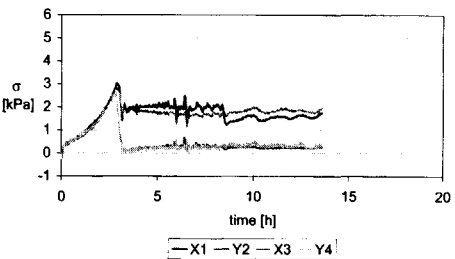


Figure 5A.7: Type Va experiment: 13.5 % (left) and 19 % (right) volume reduction.



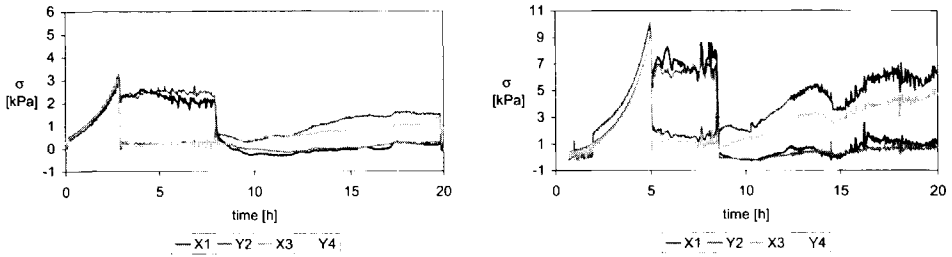


Figure 5A.8: Type Vb experiment: 13.5 % (left) and 19 % (right) volume reduction.

## 5A.2 Anisotropic flow function

Table 5A.1: Overview of flow function experiments with anisotropy.

	Step 1		Step 2					Step 4					$\sigma_{1p}$	$\sigma_{3p}$	$f_c$
	$\rho_{B_{i,j,k}}$ after step 1	$\sigma_c$	X1	Y2	X3	Y4	Z	X1	Y2	X3	Y4	Z			
			[kPa]					[kPa]							
1	937.2	6.0	10.23	1.73	10.21	1.73	5.36	0.27	3.20	0.25	2.93	1.73	10.22	1.73	3.06
2	955.0	8.0	13.89	2.03	13.97	2.05	7.42	0.25	3.71	0.25	3.35	2.07	13.93	2.04	3.53
3	972.3	10.0	16.02	3.96	16.04	3.96	8.34	0.28	4.22	0.27	4.25	2.26	16.03	3.96	4.24
4	974.6	10.0	15.89	4.15	15.85	4.13	8.23	0.44	4.13	0.41	4.05	2.75	15.87	4.14	4.09
5	957.0	12.0	19.14	4.88	19.14	4.86	9.47	0.25	5.05	0.25	4.83	2.82	19.14	4.87	4.94
6	975.0	12.0	18.68	5.37	18.63	5.32	10.21	0.40	4.40	0.43	4.32	3.66	18.66	5.35	4.36
7	991.7	14.0	23.07	4.57	23.44	5.42	11.60	0.28	4.98	0.26	4.98	3.05	23.25	4.99	4.98

---

## Microscopic structure in powder flow

In this chapter the structure that particles form in a powder will be investigated. The simulation code 3DSHEAR of Walton and Braun (1986a, 1986b) will be used to generate a particle assembly that is subjected to consolidation and shear similar to the experiments performed in earlier chapters. Finally, some suggestions for a structure tensor will be given.

### 6.1 Introduction

What is so often called the history or memory of a powder is in fact the state of the structure of the powder. This state includes the position and orientation of all particles, but also the number of contacts and their direction. If this information for the whole particle assembly is known then no history knowledge in terms of stress and strain paths is needed.

However, even if the information of the particle assembly is known, it has to be translated into meaningful parameters in order to design the constitutive equations for powder flow. Nowadays, constitutive equations often use fit parameters, making them dependent on the type of test and on the powder. The lack of insight in what is happening with the individual particles and how that adds up to the behavior of the whole is the main cause for this failure.

The combination of powder flow experiments and discrete element simulations will be the solution to this lack of knowledge about the microscopic behavior of the particles in a powder. Discrete element simulations can work like a microscope and give information about the position and the movement of each particle. The major drawback is that discrete element simulations use a lot of computer time and at this moment the maximum possible number of particles that can be simulated in 3D and in a reasonable amount of time is around  $1 \cdot 10^5$ . This number is increasing rapidly due to new computers. However, for comparison, a BCR-limestone sample in the Jenike Tester consists of about  $1 \cdot 10^{11}$  particles. The method to investigate the microscopic behavior of powder, consists of comparison of the outcome of DEM simulations with results of macroscopic experiments. If those are comparable, it is assumed that the microscopic response of the simulated sample resembles that of the real sample. Investigations on the structure are then performed with the simulated particle array.

The goal of this chapter is to investigate the structure that occurs on a particle level. The simulation code 3DSHEAR version 2.05b by Walton and Braun (1986a, 1986b, Walton 1993, Hanes and Walton 2000) is used to generate particle assemblies.

These assemblies are subjected to different types of consolidation and to shear similar to experiments described in previous chapters. These assemblies are investigated on their structure in order to find an explanation for the macroscopic behavior.

## 6.2 Structure in literature

It is difficult to measure the structure that particles form in real samples, because most techniques are intrusive and destroy the structure. The Neutron Depolarization technique, presented in Chapter 3, does not disturb the sample and can actually measure the orientation of particles. It does not, however, give direct qualitative information about the contacts between the particles. In this paragraph an overview of the work on the microscopic mechanics of powders and granular materials is given.

Cundall et al. (1982) and Oda (1972) used the normals of particle contacts to describe the structure in granular materials. They showed in experiments (Oda 1972) and 2D simulations (Cundall et al. 1982) that the directional distribution of the contact normals alters radically during strain. This alteration is initially a gain in particle contacts with normals approximately parallel to the major principal stress direction and then a loss of particle contacts with normals nearly parallel to the direction of the minor principal stress. Cundall et al. (1972) pointed out that forces are never transmitted uniformly through a sample, but sequences of particles close to the direction of major principal stress carry the load. Sliding contacts were almost never observed in these sequences of particles.

Thornton (2000) has produced DEM results for consolidation and shear that are in good agreement with laboratory experiments both for stress strain response and for porosity change. A loose and a dense packing of 5000 polydisperse spheres reached steady-state and a critical porosity. Thornton argues that the structural anisotropy that occurs in an axisymmetric compression of hard particles with constant mean stress is relatively small. The load is, agreeing to Oda (1972) and Cundall et al. (1982), transmitted primarily through chains of particles forming a network of larger than average contact forces (Thornton, 1997). The particles are thought to form pathways along which force transmission may be achieved in order to establish a stable stress state. The system does not use all pathways to the full extent. A change in the loading direction rapidly changes the pathways that are used. The most favorable contact orientations are chosen in the direction of the major principal stress. The distribution of the favorable contact orientations defines the structural anisotropy which is just partly visualized by the change in the overall contact normal distribution because the contact structure already exists (Thornton, 2000).

Thornton and Antony (1998) distinguished two types of interparticle contacts: the contacts carrying below-average normal contact forces and the contacts carrying above-average normal contact forces (figure 6.1). In this relatively rigid, heavily stressed backbone structure, an increase of the interparticle friction decreases the percentage of sliding contacts, but it also stabilizes the system and favors reorientation of force transmission paths without particle rearrangement. Sliding contacts occurred more in the subnetwork of contacts transmitting less than average forces (Thornton, 1998). Therefore, Thornton concludes that shear strength is primarily due to the development of the strong force network rather than due to work done in sliding

particles over each other. Regarding soft particle systems, Thornton remarks that the force transmission is more uniformly distributed.

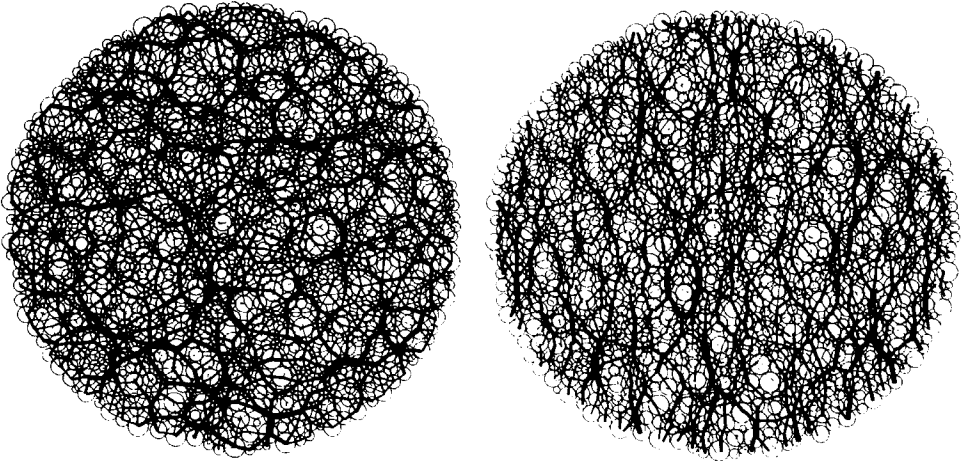


Figure 6.1: Contact force transmission in a 2D array of polydisperse discs: (left) isotropic stress state; (right) deviatoric stress state (Thornton, 1997). The same network is used to transmit the stresses.

The existence of stress chains has been visualized experimentally with relatively large photoelastic particles by Barber (1972, figure 6.2) and other researchers. These particles change the polarization of light when they are stressed and thus the stress paths can be seen. There is no technique that can show stress paths in powder with particles of micrometer size.

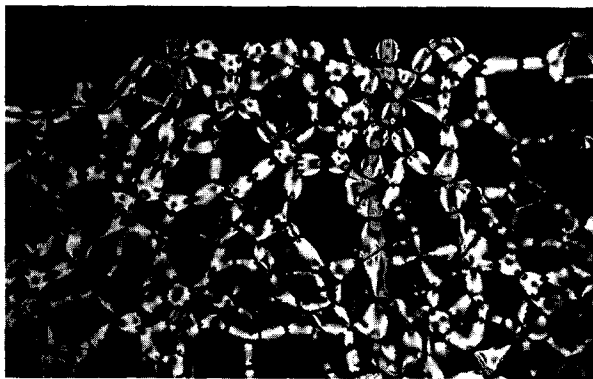


Figure 6.2: Bed (2D) of photoelastic particles with submerged load (Barber, 1972).

Arthur et al. (1986) related the anisotropic behavior of sand (600-850  $\mu\text{m}$ ) measured in the Directional Shear Cell (chapter 2) to the changing of interparticle contacts. The anisotropy of contact distribution is shown to be related to the accumulated value of

the major principal strain rather than to the stress. This relation ends when failure occurs.

A qualitative approach of the structure in powder has been done by Oda (1972) who tried to find the mechanism that controls the fabric reconstruction which occurs during the deformation of granular sand. In tedious experiments the orientation of particles were measured in thin slices of a specimen that has been hardened with a resin solution. The ratio of the projected contact areas on the  $xy$ ,  $yz$  and  $xz$  planes have been shown to describe closely the stress ratio in the sample. Satake (1982) has defined a fabric tensor that is quite often used:

$$\phi_{ij} = \frac{1}{N} \sum_{i=1}^N n_i n_j \quad (6.1)$$

in which  $M$  is the number of contacts and  $n_i$  denotes the contact normal. Thornton and Antony (1998) used this fabric tensor and decomposed it for the network of particle chains in a part for the weak subnetwork and a part for the strong subnetwork of particles.

$$\phi_{ij} = (1-q)\phi_{ij}^w + q\phi_{ij}^s \quad (6.2)$$

The proportion of contacts transmitting larger than average contact forces is called  $q$ . The strong subnetwork developed a strongly anisotropic structure both for hard-particle and for soft-particle systems. The weak subnetwork was only slightly anisotropic. This led to the conclusion that the strong subnetwork determines the deviatoric stress. All results from simulations are subject to the influence of statistics due to the relatively small number of particles that can be simulated.

A remark should be made with respect to DEM simulations. Many of these work with periodic boundaries which is a doubtful operation. As long as it is unknown on what length scale microscopic structure forms and maybe repeats itself, the choice of the size of a sample with periodic boundaries is without any found knowledge about the influence of the size. A two dimensional simulation of 10000 particles gives a sample with a length of 100 particles. A structure feature that could be building up in a normal, larger sample is disrupted because particles are almost in contact with themselves. Of course, rigid boundaries also limit the evolving or not evolving of a particular structure but this is transmitted to the boundary as stress or strain. The use of periodic boundaries destroys the typical granular behavior and makes the sample more like a continuum.

### 6.3 Simulation software code by Walton and Braun

An established discrete element method has been developed by Cundall and Strack (1979). This code forms the basic idea for the simulation code of Walton and Braun. A detailed description of the software code is given by Walton and Braun (1986a, 1986b) and Walton (1993). In this section only the basics and some adaptations are introduced.

The simulation code 3DSHEAR version 2.05b calculates the motion of a 3D system of inelastic, frictional spheres as they interact via contact forces, gravity and with boundaries. The software code performs cyclic calculations during which it alternates between the application of Newton's second law to the spheres and a force-displacement law at the contacts (figure 6.3). Newton's second law gives the motion of a particle resulting from the forces acting on it. The force-displacement law is used to find contact forces from displacements. In the program overlapping of the particles at the contact points is allowed and is seen as the deformation of individual particles. The magnitude of the overlap is related directly to the contact force. The overlaps are kept small in relation to the particle size. During the cycle new contacts and contacts that no longer exist are identified.

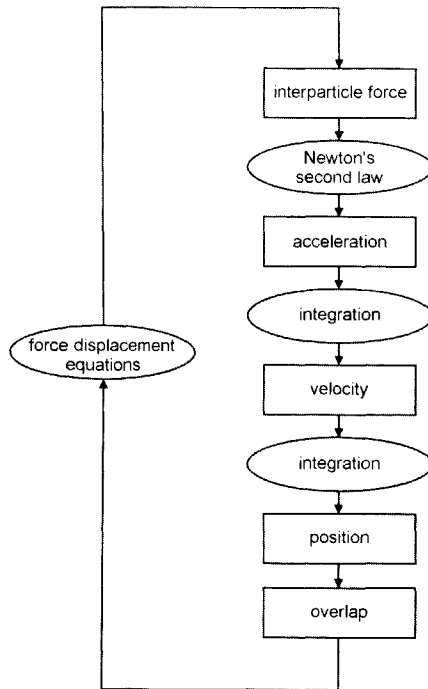


Figure 6.3: Calculation cycle for particle assemblies according to Cundall and Strack (1979).

The simulations in this chapter have been done with the hysteretic contact normal-force model described by Walton and Braun (1986a, 1986b). It consists of a linear loading and a stiffer unloading path. The tangential friction force model is based on the theoretical studies by Mindlin and Deresiewicz (1953) and is described in detail by Hancs and Walton (2000). The simulation code has no option to simulate cohesion.

The parameters utilized in the simulation are the coefficient of friction (0.3 between particles and 0.0001 between particles and walls), the coefficient of restitution (0.8), the effective stiffness of the contact force-displacement relation ( $25000 \text{ N/m}^2$ )

and the ratio of the tangential to normal stiffness (0.8). The values for these coefficients have been estimated from Hanes and Walton (2000).

3DSHEAR has been adapted slightly to simulate a 3D sample volume with six rigid walls. Four of these walls can move and experiments similar to the experiments in the Flexible Wall Biaxial Tester can be simulated. The configuration of the standard simulated volume is given in figure 6.4.

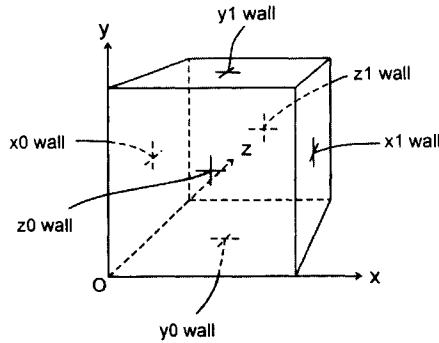


Figure 6.4: Setup of standard simulation volume.

## 6.4 Consolidation simulations

The first simulations performed are three different types of consolidation, analogue to the consolidation experiments in the FWBT (chapter 4). These types are: biaxial, uniaxial with two opposite moving walls and uniaxial with only one moving wall (figure 6.5). The simulated sample consists of a mixture 2500 spheres with a diameter of  $2\ \mu\text{m}$  and a density of  $5180\ \text{kg/m}^3$  and 2500 spheres with a diameter of  $8\ \mu\text{m}$  and a density of  $2500\ \text{kg/m}^3$ . The initial simulated cell has a volume of  $115 \times 115 \times 115\ \mu\text{m}^3$  which brings the initial porosity on 0.552.

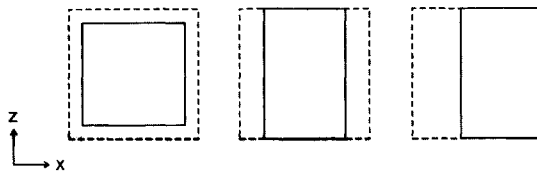


Figure 6.5: Types of consolidation: biaxial (left), uniaxial with two walls (middle), uniaxial with one wall (right).

The applied volumetric strain is 36 % and 38 % for the biaxial and both uniaxial experiments respectively. The porosity decreases to 0.301 and 0.278 respectively. The consolidations appeared to occur in two steps. In the first step, the stresses on the walls did not increase as expected. This is caused by the initial setup of the sample. The particles are placed randomly in the simulated sample volume with a random movement. A certain volumetric strain is needed for the applied deformation to have effect on the particles. This can be seen from the number of particle contacts that only starts to rise after a certain delay (figure 6.6). In the initial situation particles are not



touching and therefore, the stresses are not transmitted through the sample. The transition from the initial situation is a very fast increase of the number of contacts that ends when the particles are more or less fixed (figure 6.6). The number of contacts increases more slowly now. In this second region, particle interactions based on friction are more dominant. The sample reacts more like a continuum than in the first region.

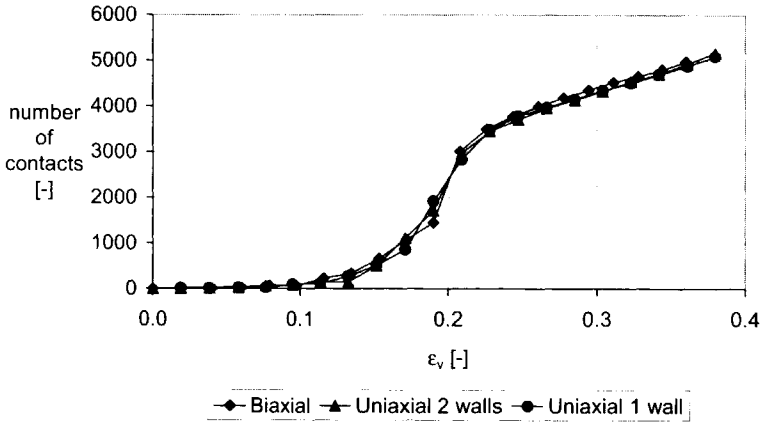


Figure 6.6: Number of contacts in the consolidation simulations.

In the second region, the normal stresses on the walls increase and the consolidation curves are similar to those in the real experiments (figure 4.24). The normal wall stresses are given in figures 6.7. The shear stresses on the walls are negligible, because the coefficient of friction between particles and the wall is kept very small.

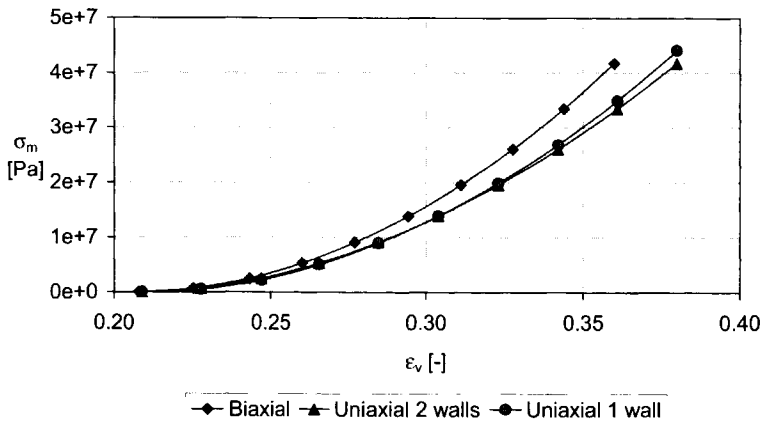


Figure 6.7: Simulations of the different consolidation simulations.

The consolidation curve of the biaxial consolidation is higher than the consolidation curves of both types of uniaxial consolidation. The same result has been seen in the

consolidation experiments with the FWBT (figure 4.24). Therefore, it is assumed that the structure of the particle assemblies resembles the structure of the BCR-limestone in the FWBT with respect to the aspects that cause the deviation between the consolidation curves.

The structure in the simulated samples is characterized by the fabric tensor as defined in equation 6.1. In order to see if the structure has a preferred orientation, the deviatoric fabric is defined as  $(\phi_1 - \phi_3)$ .

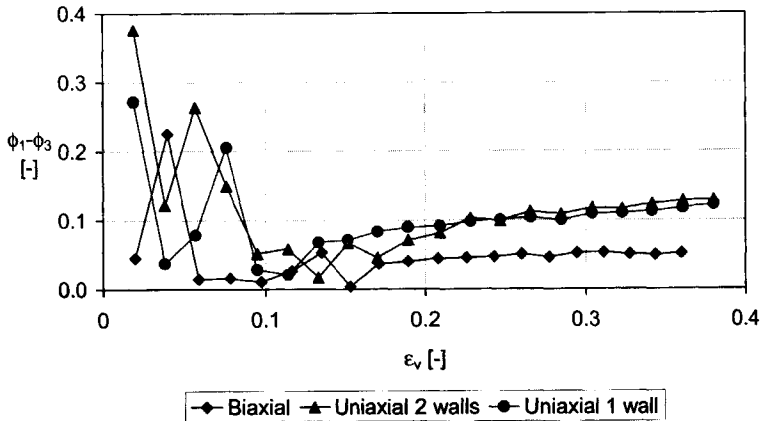


Figure 6.8: Deviatoric fabric for the different consolidations.

It is evident from figure 6.8 that the two uniaxially consolidated samples have built up a more oriented structure than the biaxially consolidated sample. The fact that the deviatoric fabric for the biaxial consolidation does not equal zero, is due to the preferred orientation of the contact normals in the  $xz$ -plane.

In cohesive BCR-limestone it is believed that a similar deviatoric fabric develops, but not defined by the contact normals but more likely by the directional distribution of the voids between particles.

## 6.5 Shear simulation

In this section a shear region is simulated as has been investigated in chapter 3. Therefore, a shear region is forced upon a simulated array of 4850 spheres with a diameter of  $8 \mu\text{m}$  (porosity is 0.380 and density  $2500 \text{ kg/m}^3$ ). The geometry of the shear cell is formed resembling the simple shear tester (figure 3.83.8). The size of the tester is  $128 * 128 * 128 \mu\text{m}^3$ , and a shear deformation of  $64 \mu\text{m}$  has been applied (figure 6.9) in the  $x$  direction.

The cell is preconsolidated by initially placing the particles in a higher volume which is then reduced by moving the top wall down until the required volume is reached. At the end of the preconsolidation the number of particle contacts is 7500 and this number remains approximately constant at 8000 during the entire shear deformation.

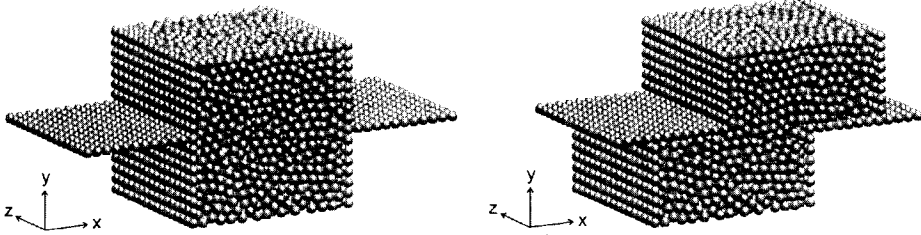


Figure 6.9: Shear simulation: start (left) and end (right).

In figure 6.10 the translation and the rotation of the particles around the z axis is given. The trajectories show a lens shaped shear zone. The rotations show a more uniform, slightly tilted zone over the x axis. Especially in top left corner of the bottom part and the bottom right corner of the top part rotation takes place while the translation is minimal.



Figure 6.10: Trajectories (left) and rotation around the z axis (right) of the particles projected on the xy plane. The shear deformation is 32  $\mu\text{m}$ . The rotation of a particle is given by a dot; the larger the rotation, the darker the dot.

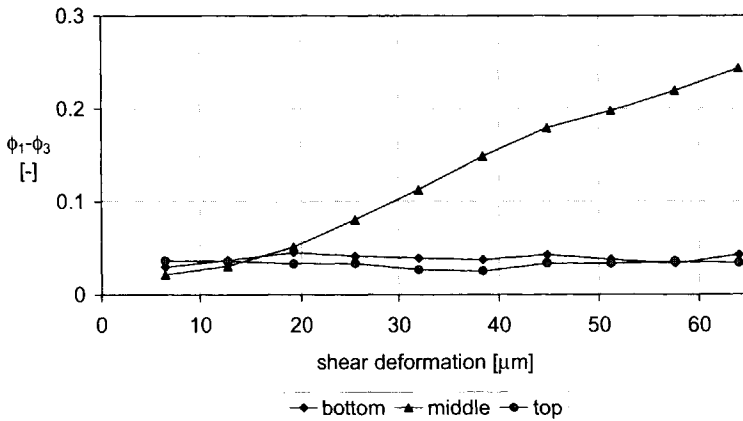


Figure 6.11: Deviatoric fabric tensor for three different slices of the sample.

The deviatoric tensor (equation 6.1) is again a measure for the structural changes in the particle assembly. The tensor has been calculated for three slices of the tester: top, middle and bottom (figure 6.11). It is obvious that the structure in the middle part where the shear zone is forced upon the sample is changing continuously, while in the top and bottom of the tester no changes occur.

In order to compare the simulation results with the results of the visualization of the shear zone in figure 3.25 the rotations around the z axis have been averaged for each xz plane (figure 6.12).

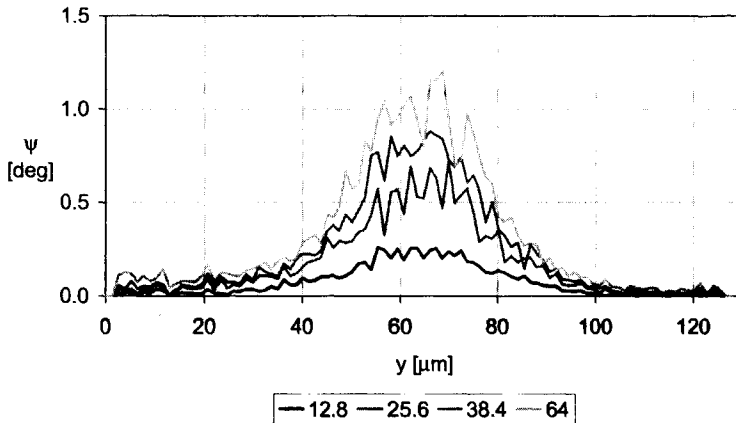


Figure 6.12: Rotation of the particles around the z axis as a function of the height. The numbers are the applied deformations in  $\mu\text{m}$ .

Figure 6.12 shows the same trend as has been measured with the ND technique (figure 3.25). In the simulation, as in the experiments, only the  $\psi$  rotation is preferred, showing that the particles rotate as would be expected from the applied shear.

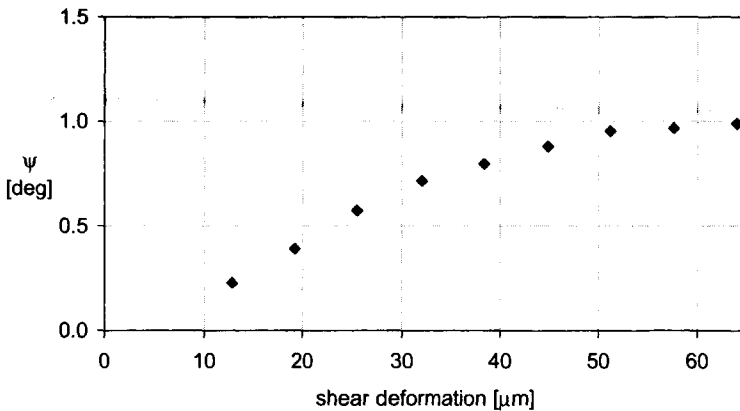


Figure 6.13: Rotation versus translation of the particles for the shear simulation in the middle of the shear zone.

In figure 6.13 the rotation in the middle of the shear zone is plotted versus the applied shear deformation. This relation is proportional for lower shear deformations, but levels off for higher values. This is due to the fact that the contact area between the particles in the bottom and top half of the tester reduces significantly during the shear (figure 6.9). The proportional relation has been seen experimentally as well (figure 3.26).

From figures 6.10 and 6.12 the width of the shear region can be estimated at 5 or 6 times the particle diameter. This is in good agreement with the measurements in literature (table 3.1) for non-cohesive particles. The change in the rotation in figure 6.12 in relation to the shear deformation is comparable to the results with cohesive BCR-limestone in chapter 3. However, the simulations do not include cohesion and it is expected that this is the reason why the width of the shear region in cohesive BCR-limestone is much wider.

## 6.6 Suggestions for the structure tensor in powder

A powder consists of an array of particles that interact with each other. In principle, every particle can have a different size and shape and they may be arrayed in an infinite number of ways. Nevertheless, some properties, e.g. bulk density, are reproducible to a certain extent. Therefore, the relation between the microscopic and macroscopic properties is not unique, a different array leads to a different relationship. The type of array that particles form, depends on the process conditions and on the history of the powder. The array itself is dictated by the distribution of particle size and shape. This fundamental principle is further elaborated in Scarlett et al. (1998).

The general structure tensor that relates the stress and strain tensor should be of the fourth order (equation 6.3). This structure tensor consists of 81 terms and it is believed that the concept of this tensor can be built up from simpler first and second order tensors. In this paragraph structure tensors of first and second order are investigated for their possibility to describe the information that is important to relate the stress tensor to the strain tensor.

$$\underline{\underline{T}} = \underline{\underline{S}} \underline{\underline{E}} \quad (6.3)$$

The structure of a particle array is thought to consist of different components (figure 6.14). First, the positions of the particles are important. They determine the bulk density and the homogeneity of the bulk density. The orientation of the particles is significant in case of a non-spherical shape. The shape of the particles is thought to influence the ratio of sliding and rotating contacts. The third contributor to the structure of a particle assembly are the established point contacts.

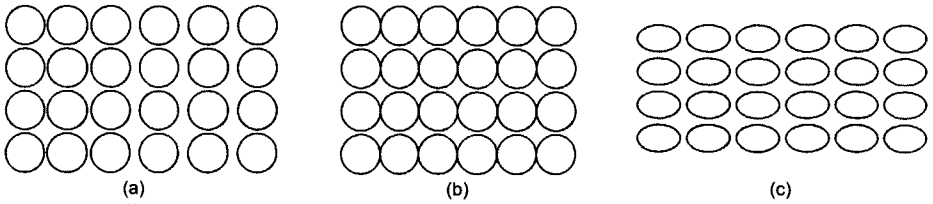


Figure 6.14: Three factors contributing to the structure in a particle assembly: position (a), contact structure (b), shape (c).

To describe these contributions mathematically the position vector  $\mathbf{r}$  of an element of surface  $ds$  of the particle and the surface normal vector  $\mathbf{n}$  is defined (figure 6.15).

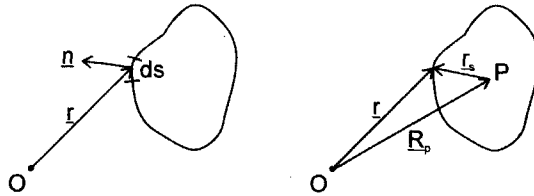


Figure 6.15: Position vector  $\mathbf{r}$  and normal vector  $\mathbf{n}$  of a surface element  $ds$ . The position vector  $\mathbf{r}$  is built from the position vector of the particle  $\mathbf{R}_p$  and the relative position vector  $\mathbf{r}_s$  of surface element.

From these two vectors a number of tensors of various rank can be constituted that when integrated over the whole sample, describe parts of the structure in the powder. The tensors are presented in the dyadic notation (Weatherburn, 1957).

The first tensor is a scalar based on the surface normal vector  $\mathbf{n}$ . It describes the projected area of a particle in a certain direction (here  $\mathbf{i}$ ).

$$\frac{1}{2} \int ds |\mathbf{n} \cdot \mathbf{i}| \tag{6.4}$$

Integrated over all particles this parameter shows the orientation of the particles when resolved in any direction (figure 6.14c). The parameter is independent of the size and position of the particles.

The position vector in figure 6.15 can be used to make up a parameter that describes the homogeneity of the bulk density. The integration of the position vector over the whole particle surface (equation 6.5) describes the center of gravity of the particle and when it is integrated over the whole powder sample it describes the center of gravity of the sample (figure 6.14a) and is thereby a measure for the homogeneity.

$$\int ds \mathbf{r} \tag{6.5}$$

The following tensors are made up of two vectors. The first one is a symmetric tensor consisting of the dyad of the unit normal vector at a surface element  $ds$ .

$$\int d\underline{s} \underline{n} \quad (6.6)$$

The scalar invariant of this tensor integrated over all particles is equal to the total surface of the particle assembly. The vector invariant of the dyad is zero which means that the tensor is symmetric. This tensor has the following form:

$$\int d\underline{s} \underline{n} = \begin{pmatrix} \int d\underline{s} \underline{n} : \underline{i}_1 \underline{i}_1 & 0 & 0 \\ 0 & \int d\underline{s} \underline{n} : \underline{i}_2 \underline{i}_2 & 0 \\ 0 & 0 & \int d\underline{s} \underline{n} : \underline{i}_3 \underline{i}_3 \end{pmatrix} \quad (6.7)$$

The terms on the diagonal represent two times the amount of area in the direction  $\underline{i}$ . This tensor contains the same information as the scalar in equation 6.4 resolved in three perpendicular directions. Thus, it gives information about the particle structure as shown in figure 6.14c.

The dyad built from the position vector and the unit normal vector in figure 6.15 is given in equation 6.8.

$$\int d\underline{s} \underline{r} = V \underline{I} \quad (6.8)$$

The scalar invariant of this tensor is three times the volume of a particle and, in fact, this tensor is trivial because it equals the idem factor times the volume. However, the tensor can be applied to an array of particles representing the total volume of all particles. The pore volume in the array can be calculated by defining an imaginary boundary around the array and applying the scalar invariant of equation 6.8 to it. This defines the enclosed volume. Subtraction of the total particle volume gives the pore volume. The tensor is invariant with respect to the origin.

Finally, a dyad formed from the position vector is evaluated. A special point of each particle is chosen (figure 6.15) such that:

$$\int d\underline{s} \underline{r}_s = 0 \quad (6.9)$$

The dyadic consists of four parts:

$$\begin{aligned} \int d\underline{s} \underline{r} \underline{r} &= \int d\underline{s} (\underline{R}_p + \underline{r}_s) (\underline{R}_p + \underline{r}_s) = \\ &= \int d\underline{s} \underline{R}_p \underline{R}_p + \int d\underline{s} \underline{R}_p \underline{r}_s + \int d\underline{s} \underline{r}_s \underline{R}_p + \int d\underline{s} \underline{r}_s \underline{r}_s \end{aligned} \quad (6.10)$$

Equation 6.10 is reduced because two of these parts equal zero:

$$\int ds \underline{r} \underline{r} = \int ds \underline{R}_p \underline{R}_p + \int ds \underline{r}_s \underline{r}_s \quad (6.11)$$

However, the last term on the right hand side in equation 6.11 is independent of the particle position and is a measure for the size of the particles. The first term on the right hand side reduces to a simple tensor which does not describe a useful part of the structure:

$$\int ds \underline{R}_p \underline{R}_p = S \underline{R}_p \underline{R}_p \quad (6.12)$$

For that reason the dyadic based on the position vector of a surface element  $ds$  does not describe a useful aspect of the structure. The particle spacing as pictured in figure 6.14a is not described by this tensor. However, the tensor described in equation 6.5 is a measure for the homogeneity and thus indirect for the particle spacing.

The above described tensors have only the capabilities to describe parts of the structure components as pictured in figure 6.14a and c. However, the interparticle contacts are not captured yet. The parameter introduced in equation 6.1 (Satake, 1982) has the possibility to do that, but this parameter does not start from basic particle properties.

These reflections show that the structure in a powder can be approached with tensors. In future work 3<sup>rd</sup> and 4<sup>th</sup> order tensors should be investigated to develop the structure tensor. This tensor is not only needed for the correct description of the flow behavior of powder, but it is needed to manipulate the flow properties and make a powder with a chosen flow characteristic. This can be done by choosing the mixture of particle sizes, shapes and other particle properties that result in the desired structure tensor.

## 6.7 Conclusion

In this chapter the structure that forms in a cohesionless sample of particles is studied. Both consolidations and a shear experiment have been simulated in order to compare the results to the experimental results in chapters 3 and 4. The structure tensor defined by Satake (1982) is a good measure for the orientation of the structure.

The simulation of the shear plane experiment resulted in a width of the shear region that agrees with literature for non-cohesive materials, but not with the shear experiments done on BCR-limestone. It is very likely that the cohesion plays an important role in the shear behavior of powder.

The simulation of the biaxial and uniaxial consolidations proved that an oriented structure builds up in the contacts between the particles. The position of the consolidation curves showed the same trend as in the experiments in chapter 4. This results strengthens the conclusion that particles can rearrange more easily in a uniaxial consolidation.

Finally, a number of tensors have been presented that are thought to describe different components of the structure in powder. The challenge for the future will be



to use individual particle properties for the development of powder with chosen flow properties by means of the structure tensor.



## Conclusion

The research in the area of powder technology is characterized by a lack of fundamental breakthroughs for the last 30 years. Many different types of shear testers have been built in order to measure flow behavior of powder, but this has not led to a substantial increase in the understanding of powder flow. It is stated that the reason for this situation is the fact that an important parameter is missing in the existing theory: structure. It is very difficult to measure or model structure, which explains the slow progress in this research area. In this thesis, powder flow is investigated with a shear tester that is purely developed for the investigation of fundamental powder flow: the Flexible Wall Biaxial Tester. The aim of this work is to enhance the knowledge about powder flow behavior focussing on shear regions and on structure in powder.

The flow of a powder occurs by the formation of shear regions. The shear region that forms in a simple direct shear tester has been investigated in this work with the Neutron Depolarization (ND) technique. This technique has proven to be a very powerful tool for the microscopic investigation of a shear region because aspects like the shape and width of the region can be visualized as well as the rotations of the particles and the local bulk density. The visualization of the rotation of the particles makes the ND technique superior to X-ray scanning. The sample powder that is used, is a mixture of BCR-limestone and 3 weight % Ferroxdure.

The ND experiments show that the rotation of particles in a shear region is proportional to the applied shear deformation. The rotation has a preferred direction which agrees with the direction in which shear is applied. A uniaxial loading experiment without applied shear deformation also showed rotation of the particles proportional to the translational downward movement of the particles. This rotation did not have a preferred orientation and was a function both of time and of the applied load.

The size of the shear region is about 1000 to 2000 particle diameters and it remained constant during the application of shear deformation up to 3 mm. It seemed that the shear region width increased with the applied consolidation load, but this observation needs further investigation.

Pictures of the shear plane showed a particular wave form that first moves down and then upwards in the direction of the shear deformation. This pattern has been shown by other researchers (Schwedde, 1971). It is generally accepted that the shear region has a lens shape and the ND technique indicates this as well. However, it remained unclear whether the shear region consists of individual shear zones with stagnant regions in between or whether the particles in the region all contribute to the

rotation. This work shows that the assumption that the shear plane is flat and horizontal, as made in many direct shear testers, is incorrect.

The Flexible Wall Biaxial Tester has been built by Kraan (1996) with the objective of the fundamental investigation of powder flow. In this thesis this tester is evaluated and is found to be very flexible in the types of experiments it can perform partly as a result of the possibility to operate in stress or strain controlled mode. The Flexible Wall Biaxial Tester has been improved to make operation easier and experiments can be performed automatically without interference of the operator. This was necessary because experiments are time consuming due to the slow strain rates that are applied. The major disadvantage of the tester are the membranes, which are vulnerable and difficult to make. It has been shown that the shear stresses applied by the side walls is zero when the powder deforms homogeneously. The top and bottom membrane do apply a shear stress which is kept to a minimum level by using a lubricant.

The first experiments performed with the Flexible Wall Biaxial Tester are consolidations of three different types: biaxial, uniaxial and uniaxial with strain applied with one wall. The spread in the consolidation stress paths versus the bulk density is quite large, although the shape of the lines is equal. As predicted by Roscoe et al. (1958), the consolidation line of the uniaxial consolidations is lower than that of the biaxial consolidation due to the deviatoric stress.

Comparison of the Braunschweig Biaxial Tester with the Flexible Wall Biaxial Tester consisted of both a biaxial and a uniaxial consolidation followed by a shear step. Again the spread in the consolidation curve versus the bulk density is quite large, but the relation between the major and minor principal stress does agree very well for both the biaxial and the uniaxial consolidations. The steady-state shear stresses in both testers lay on the same failure line. It can be concluded that the Braunschweig Biaxial Tester and the Flexible Wall Biaxial Tester are consistent in their results. The dependency of the consolidation curve on the initial bulk density needs further investigation.

For a complete evaluation of the Flexible Wall Biaxial Tester the flow function of BCR-limestone has been measured and has been compared with flow functions produced in other shear testers. The flow function of the FWBT is higher than the standard flow function by Akers (1992). The effect of time consolidation causes the main part of this difference. The flow function in this thesis is also consistent with the corrected flow function of Kraan (1996).

In the determination of the flow function, the intermediate stress has always been assumed to play a negligible role. This has been investigated in the Flexible Wall Biaxial Tester by manipulating the intermediate stress by taking the top lid off. It is proven that a low intermediate stress decreases the unconfined yield strength and a high intermediate stress increases the failure stress. In this context the definition of the unconfined yield strength is incomplete. As a result of this, the flow function procedure of Maltby (1993) produces a different flow function as measured by conventional testers.

---

Anisotropy in powder flow is a phenomenon that cannot be explained by the classical theory. It is postulated that anisotropy is caused by structure in powder. This structure cannot be described completely by porosity or bulk density, which are regarded as just a shadow of the whole structure parameter.

The Flexible Wall Biaxial Tester is used to induce anisotropy in cohesive BCR-limestone by applying a consolidation and preshear step. It has been shown that the powder is weaker in the direction perpendicular to the direction in which the major principal stress has been applied during the preshear step. This is thought to be caused by a favorable structure that forms in the powder during the preshear step.

The effect of the induced structure is shown by investigating the powder with different strain paths. These strain paths caused shear stresses which indicates that the powder behaves inhomogeneously. This could mean that the principal axes of stress and strain are locally not aligned. Non-coaxiality has been shown by Wong and Arthur (1985) for non-cohesive sand but it has not been shown for BCR-limestone. A specialized tester is needed to investigate non-coaxiality in cohesive powder.

The influence of anisotropy on the flow function has been measured by rotating the principal axes of stress in the unconfined yield strength determination with respect to the preshear step. This anisotropic flow function is lower than the regular one, because the powder is weaker when the major principal stress has rotated over 90 degrees. Manipulation of the flow properties can thus take place by changing the direction of the principal axes.

The discrete element simulation with 3DSHEAR of Walton and Braun (1986a 1986b) of a biaxial and a uniaxial consolidation has shown that the structure of the particle array can be described by a simple structure tensor defined by Satake (1982). Also a shear region in a direct shear tester has been simulated. The width of that shear region agrees with literature for non-cohesive materials, but not with the shear experiments done on BCR-limestone. This is most likely due to the cohesion of powder.

The structure that forms in a granular material consists of different contributions, like the spacing, the orientation and the distribution of the contact normals. In order to develop the mathematical relation between stress and strain, the structure has to be captured in a tensor. Suggestions have been given for tensors that can describe these different components.

Jenike's definition of powder flow by means of normal stress, shear stress and porosity is too simple. The research on powder flow behavior should combine the increasing capabilities of computer simulations with the capabilities of true biaxial and triaxial testers in order to measure and manipulate the parameter that is missing in the present theory: structure. If the relation between the stress and strain tensor via the structure tensor becomes more clear, it will be possible to develop powder properties by manipulating particle properties. This will lead to the fundamental breakthrough needed in powder flow research.



# List of symbols

$\alpha$	constant	1.5	[m]
$\gamma_{ij}$ ( $i, j = x, y, z$ )	strain in $j$ -direction on plane normal to $i$ -direction		[kPa]
$\dot{\gamma}_{ij}$ ( $i, j = x, y, z$ )	shear strain rate		[1/s]
$\delta$	diameter of magnetic clusters		[m]
$\delta$	deposition direction of sample		[°]
$\Delta$	membrane deformation		[ $\mu$ m]
$\varepsilon$	porosity		[-]
$\varepsilon_a$	constant		[-]
$\varepsilon_{crit}$	critical porosity		[-]
$\varepsilon_i$ ( $i = x, y, z$ )	normal strain in $i$ -direction on plane normal to $i$ -direction		[kPa]
$\dot{\varepsilon}_i$ ( $i = x, y, z$ )	strain rate		[1/s]
$\varepsilon_{ii}$ ( $i = x, y, z$ )	normal strain in $i$ -direction on plane normal to $i$ -direction		[kPa]
$\theta$	rotation		[deg]
$\theta$	angle of the shear plane		[deg]
$\kappa$	constant		[-]
$\lambda$	wavelength of neutrons	$1.6 \cdot 10^{-10}$	[m]
$\rho_{bulk}$	bulk density		[kg/m <sup>3</sup> ]
$\rho_{ferroxdure}$	density of ferroxdure	5180	[kg/m <sup>3</sup> ]
$\rho_{limestone}$	density of BCR-limestone	2500	[kg/m <sup>3</sup> ]
$\rho_{material}$	density of material		[kg/m <sup>3</sup> ]
$\sigma$	normal stress		[kPa]
$\sigma_1$	major principal stress		[kPa]
$\sigma_{1c}$	major principal stress after consolidation		[kPa]
$\sigma_{1p}$	major principal stress at steady-state		[kPa]
	preshear		[kPa]
$\sigma_2$	intermediate principal stress		[kPa]
$\sigma_3$	minor principal stress		[kPa]
$\sigma_{3c}$	minor principal stress after consolidation		[kPa]
$\sigma_{3p}$	minor principal stress at steady-state		[kPa]
	preshear		[kPa]
$\sigma_{axial}$	axial normal stress		[kPa]

$\sigma_c$	normal stress in consolidation step	[kPa]
$\sigma_i$ ( $i = x, y, z$ )	normal stress in i-direction on plane normal to i-direction	[kPa]
$\sigma_{ii}$ ( $i = x, y, z$ )	normal stress in i-direction on plane normal to i-direction	[kPa]
$\sigma_m$	mean stress = $\frac{1}{3}(\sigma_1 + \sigma_2 + \sigma_3)$	[kPa]
$\sigma_p$	normal stress at steady-state preshear	[kPa]
$\sigma_r$	deviatoric stress	[kPa]
$\sigma_{\text{radial}}$	radial normal stress	[kPa]
$\sigma_s$	normal stress on shear plane at failure	[kPa]
$\Sigma$	constant	[m <sup>3</sup> /kg]
$\tau$	shear stress	[kPa]
$\tau_{ij}$ ( $i, j = x, y, z$ )	shear stress in j-direction on plane normal to i-direction	[kPa]
$\tau_p$	shear stress at steady-state preshear	[kPa]
$\tau_s$	shear stress on shear plane at failure	[kPa]
$\varphi$	precession angle	[deg]
$\Phi_1 - \Phi_3$	deviatoric fabric tensor	[-]
$\Phi_f$	angle of failure	[deg]
$\Phi_i$ ( $i = x, y, z$ )	mean magnetization in i-direction	[rad]
$\Phi_{ij}$ ( $i = x, y, z$ )	fabric tensor	[-]
$\Phi_{y,0}$	initial mean magnetization in y-direction	[rad]
$\Phi_{z,0}$	initial mean magnetization in z-direction	[rad]
$\Delta\psi$	= $ \psi_A - \psi_B $	[°]
$\psi$	rotation	[deg]
$\psi_A$	direction of $\sigma_{1A}$	[°]
$\psi_B$	direction of $\sigma_{1B}$	[°]
I	invariant of the characteristic equation	[kPa]
II	invariant of the characteristic equation	[kPa <sup>2</sup> ]
III	invariant of the characteristic equation	[kPa <sup>3</sup> ]
$B_s$	average magnetic field of sample	[T]
$B_{s,0}$	initial average magnetic field of sample	[T]
$c = \frac{(c_2 \lambda)^2}{2}$	constant	[T <sup>-2</sup> m <sup>-2</sup> ]
$c_2$	constant	$4.637 \cdot 10^{14}$ [T <sup>-1</sup> m <sup>-2</sup> ]
$c_{\text{ferrox}}$	volume fraction of ferroxdure particles	[-]
$\underline{D}$	depolarization matrix	[-]
$D_1$	diameter of piston	[m]
$D_2$	diameter of opening	[m]
$D_3$	diameter of cilinder	[m]



$d_{\text{eff}}$	effective magnetic thickness	[m]
Det	determinant of rotation matrix	[-]
$D_{ij}$ ( $i, j = x, y, z$ )	element of depolarization matrix (3*3)	[-]
$d_p$	particle diameter	[m]
ds	element of surface	[m <sup>2</sup> ]
$d_{\text{tester}}$	diameter of tester	[m]
c	void ratio	$= \frac{\epsilon}{1 - \epsilon}$ [-]
$\underline{E}$	strain tensor	[-]
$f_c$	unconfined yield strength	[kPa]
$F_c$	normal consolidation force	[N]
$F_s$	normal force at failure	[N]
h	expansion of bed	[m]
$h_{\text{sample}}$	height of sample	[m]
$h_{\text{tester}}$	height of tester	[m]
H	depth of shear	[m]
$\underline{i}$	unit vector	[-]
$\underline{I}$	idem factor	[-]
$I_0$	intensity measured without sample	[-/s]
$I_{\text{average, monitor}}$	averaged monitor intensity	[-/s]
$I_{\text{background}}$	background intensity	[-/s]
$I_{ij}$ ( $i, j = x, y, z, Z$ )	intensity	[-/s]
$I_{\text{monitor}}$	monitor intensity	[-/s]
$I_{\text{sh}}$	shim intensity	[-/s]
$I_{\text{sh, measured}}$	measured shim intensity	[-/s]
$l_i$ ( $i = X1, ..Y4$ )	wall position	[m]
$l_{i,0}$ ( $i = X1, ..Y4$ )	begin position of wall	[m]
$l_{\text{tester}}$	length of tester	[m]
$l_x$	x length of sample	[m]
$l_y$	y length of sample	[m]
$\Delta l_i$ ( $i = x, y, z$ )	deformation of sample in i direction	[m]
$\Delta l_x$	x deformation of sample	[m]
$\Delta l_y$	y deformation of sample	[m]
m	mass of sample	[kg]
$\underline{n}$	unit normal vector	[-]
$n_i$ ( $i = x, y, z$ )	contact normal in x, y or z direction	[-]
N	number of contact normals	[-]
$\underline{P}$	polarization vector of outgoing beam	
$\underline{P}_0$	polarization vector of incoming beam	
q	proportion of contacts	[-]
$\underline{r}$	position vector of surface element ds	[m]
$\underline{r}_s$	radius of particle at surface element ds	[m]
$R_p$	position vector of particle	[m]
S	surface of particle	[m <sup>2</sup> ]
S	surface of shear plane	[m <sup>2</sup> ]

---

$\underline{\underline{S}}$	structure tensor	[-]
$\underline{\underline{S}}_r$	deviatoric stress tensor	[kPa]
$\Delta t$	timestep	[s]
$\underline{\underline{T}}$	stress tensor	[kPa]
$V$	volume	[m <sup>3</sup> ]
$V_{\text{tester}}$	volume of tester	[m <sup>3</sup> ]

## References

- Akers R.J., **1992**, The certification of a limestone powder for Jenike shear testing, Community Bureau of Reference-BCR, CRM 116, Brussels.
- Allersma H.G.B., IUTAM Conference on Deformation and Failure of Granular Materials, 31 Aug. - 3 Sept., Delft, The Netherlands, 345-353.
- Arthur J.R.F., Bekenstein S., Germaine J.T., Ladd C.C., **1981**, Laboratory shear strength of soil, ASTM Spec. Tech. Publ. 740, Symposium June 25, Chicago, III.
- Arthur J.R.F., Koenders M.A., Wong R.K.S., **1986**, Acta Mechanica, 64, 19-29.
- Arthur J.R.F., Chua K.S., Dunstan T., **1977**, Géotechnique, 27, 1, 13-30.
- Arthur J.R.F., Menzies B.K., **1972**, Géotechnique, 22, 1, 115-128.
- Barber B., **1972**, Stress distributions in particulate systems, Ph.D. thesis Loughborough University of Technology.
- Bardet J.P., Proubet J., **1991**, Géotechnique, 41, 4, 599-613.
- Bell T.A., Ennis B.J., Grygo R.J., Scholten W.J.F., Schenkel M.M., **1994**, Bulk solids handling, 12, 1.
- Bell T.A., Grygo R.J., Duffy S.P., Puri V.M. , **1995**, Preprints Partec, Nürnberg, Germany, 79-88.
- Cambou B., **1982**, IUTAM Conference on Deformation and Failure of Granular Materials, 31 Aug. - 3 Sept., Delft, The Netherlands, 3-12.
- Carson J.W. , **1992**, Letter to the editor, Bulk solids handling, 12, 2, 332.
- Cristescu N., **1988**, Rock rheology, Kluwer, London.
- Cundall P.A., Drescher A., Strack O.D.L., **1982**, IUTAM Conference on Deformation and failure of granular materials, Delft, 31 Aug.- 3 Sept., 355-370.
- Cundall P.A., Strack O.D.L., **1979**, Géotechnique, 29, 47-65.
- De Josselin de Jong B., **1971**, Géotechnique, 21, 155-163.
- EFCE Working Party on the Mechanics of Particulate Solids, **1989**, Standard shear testing technique for particulate solids using the Jenike Shear Cell, The Institution of Chemical Engineers, Rugby, England.
- Enstad G.G., Maltby L.P. , **1992**, Bulk solids handling, 12, 2, 451-454.
- Feise H.J., **1996**, Modellierung des mechanischen Verhaltens von Schüttgütern, Ph.D. thesis Technical University of Braunschweig, Germany.
- Feise H.J., **1998**, Powder Technol., 98,191-200.

- 
- Gerritsen A.H., **1985**, Powder Technology, 43, 61-70.
- Gutierrez M., Ishihara K., Towhata I., **1991**, Soils and foundations, 31, 4, 121-132.
- Hanes D.M., O.R. Walton, **2000**, Powder Technology, 109, 133-144.
- Harder J., **1986**, Ermittlung der Fließeigenschaften kohäsiver Schüttgüter mit einer Zweiaxialbox, Ph.D. thesis Technical University of Braunschweig, Germany.
- Hicher P.-Y., **1998**, in: Behaviour of granular materials, ed. Cambou B., Springer, 1-48.
- Hvorslev M.J., **1937**, Ingeniorvidenskab., Skrifter A 45.
- Janssen H.A., **1895**, Zeitschrift des Vereines deutscher Ingenieure, XXXIX, 35, 1045-1049, or: **1995**, Preprints Partec, Nürnberg, March 21-23, Germany, 2-6.
- Janssen R.J.M., Raharja A.W.W., Scarlett B., **1999**, Proceedings Reliable flow of particulate solids III, Porsgrunn, Norway, 159-165.
- Jenike A.W., **1961**, Gravity flow of bulk solids, Bulletin no. 108, Eng. Experiment Station, The University of Utah, Salt Lake City.
- Jenike A.W., **1964**, Storage and flow of solids, Bulletin no. 123, Eng. Experiment Station, The University of Utah, Salt Lake City.
- Joer H.A., Lanier J., Fahey M., **1998**, Geotechnique, 49, 5, 605-619.
- Johanson J.R., **1992a**, Bulk solids handling, 12, 2, 237-240.
- Johanson J.R., **1992b**, Bulk solids handling, 12, 3, 456.
- Johanson J.R., **1993**, Proceedings Reliable flow of particulate solids II, Norway, 1-19.
- Kraan van der M., **1996**, Techniques for the measurement of cohesive powders, Ph.D. thesis Delft University of Technology, The Netherlands.
- Kruyt N.P., **1994**, Aspects of constitutive relations for cohesionless granular materials, Ph.D. thesis Delft University of Technology, The Netherlands.
- Li F., Puri V.M., **1996**, Powder Technology, 89, 197-207.
- Macosko C.W., **1994**, Rheology principles, measurements, and applications, VCH Publishers Inc.
- Maltby L.P., **1993**, Investigation of the behaviour of powders under and after consolidation, Ph.D. thesis Telemark Institute of Technology, Porsgrunn, Norway.
- Maltby L.P., Enstad G.G., **1993**, Bulk Solids Handling, 13, 135.
- Maltby L.P., Enstad G.G., De Silva S.R., **1995**, Particle and Particle Systems Characterization, 12, 1, 16-27.
- Mandl G., De Jong de L.N.J., Maltha A., **1977**, Rock Mechanics, 9, 95-144.
- Marjanovic P., Geldart D., Orband J.L.R., Mooney T., **1995**, Preprints Partec, Nürnberg, Germany, 69-78.
- Marjanovic P., McGee E., **1999**, Proceedings Reliable flow of particulate solids III, Porsgrunn, Norway, 151-158.
- Menzies B.K., Phillips A.B., **1972**, Géotechnique, 22, 153-155.
- Merrow E.W., **1988**, Chemical Engineering, 10, 89-92.
-

- Mindlin R.D., Deresiewicz H., **1953**, *Journal of Applied Mechanics Trans ASME Series E*, 20, 327-344.
- Molerus O., **1975**, *Powder Technology*, 12, 259-275.
- Mühlhaus H.B., Vardoulakis I., **1987**, *Géotechnique*, 37, 3, 271-283.
- Nedderman R.M., **1992**, *Statics and kinematics of granular materials*, Cambridge University Press, Cambridge, UK.
- Nowak M., **1993**, *Spannungs-/Dehnungsverhalten von Kalkstein in der Zweiaxialbox*, Ph.D. thesis Technical University of Braunschweig, Germany.
- Oda M., **1972**, *Soils and foundations*, 12, 2, 1-18.
- Oda M., Kazama H., Konishi J., **1998**, *Mechanics of materials*, 28, 103-111.
- Oda M., Iwashita K., **2000**, *International Journal of Engineering Science*, 38, 1713-1740.
- Orange project, **2000**, *Student reports in cooperation between Engineering Research Centre and Particle Technology Group Delft, University of Florida and Delft University of Technology*.
- Ose S., De Silva S.R., **2000**, *Proceedings Third Israeli conference on conveying and handling of particulate solids*, May, Dead Sea, Israel, 3.73-3.78.
- Peschl I.A.S.Z., **2000**, *Course Quality control and powder technology*, University of Bremerhaven, June 5-7.
- Ploof D.A., Carson J.W., **1994**, *Bulk solids handling*, 14, 1, 127-132.
- Por P.T., **1995**, *Neutron Depolarisation in Magnetic Recording Materials*, PhD thesis Delft University of Technology, The Netherlands.
- Pradel D., Ishihara K., Gutierrez M., **1990**, *Soils and foundations*, 30, 1, 87-99.
- Rekvedt M.Th., **1989**, *Textures and Microstructures*, 11, 127-142.
- Reynolds O., **1885**, *On the dilatancy of media composed of rigid particles in contact*, *Philosophical Magazine*, 20, 127.
- Roscoe K.H., Schofield A.N., Wroth C.P., **1958**, *Géotechnique*, 8, 22-53.
- Roscoe K.H., **1970**, *Géotechnique*, 20, 129-170.
- Saraber F., Enstad G.G., Haaker G., **1991**, *Powder Technology*, 64, 183-190.
- Satake M., **1982**, *IUTAM Conference on Deformation and failure of granular materials*, Delft, 31 Aug.- 3 Sept., 63-68.
- Scarlett B., Kraan van der M., Janssen R.J.M., **1998**, *Philosophical Transactions of the Royal Society of London A*, 356, 2623-2648.
- Scarlett B., Todd A.C., **1968**, *Transactions of the ASME*, 68 MH-20, 1-10.
- Scarpelli G., Wood D.M., **1982**, *IUTAM Conference on Deformation and failure of granular materials*, Delft, 31 Aug.- 3 Sept., 473-484.
- Schrauwers A., **1998**, *Delft Integraal*, publication of Delft University of Technology, 6, 13-17.
- Schwedes J., **1971**, *Scherverhalten leicht verdichteter, kohäsiver Schüttgüter*, Ph.D. thesis Technische Universität Braunschweig.

- 
- Schwedes J., **1996**, Powder Technology, 88, 285-290.
- Schwedes J., **1999**, Proceedings Reliable flow of particulate solids III, Norway, 3-40.
- Schwedes J., Schulze D., **1992**, Letter to the editor, Bulk solids handling, 12, 3, 454-455.
- Scott A.M., Bridgwater J., **1976**, Self-diffusion of spherical particles in a simple shear apparatus.
- Teunissen J.A.M., Vermeer P.A., **1988**, International Journal for Numerical and Analytical Methods in Geomechanics, 12, 323-340.
- Thornton C., **1997**, Kona, 15, 81-90.
- Thornton C., Antony S.J., **1998**, Philosophical Transactions of the Royal Society of London A, 356, 2763-2782.
- Thornton C., **2000**, in: Constitutive modelling of granular materials, Kolymbas D. (ed.), Springer, 193-208.
- Velthuis te S.G.E., **1999**, Phase transformations in steel - A neutron depolarization study, Ph.D. thesis Delft University of Technology, The Netherlands.
- Verlinden A., **2000**, Experimental assessment of shear testers for measuring flow properties of bulk solids, Ph.D. thesis University of Bradford, UK.
- Walton O.R., R.L. Braun, **1986a**, Acta Mechanica, 63, 73-86.
- Walton O.R., R.L. Braun, **1986b**, J. Rheology, 30, 5, 949-980.
- Walton O.R., **1993**, Mechanics of materials, 16, 239-247.
- Weatherburn C.E., **1957**, Advanced vector analysis, G.Bell and Sons Ltd., London, UK.
- Wong R.K.S., Arthur J.R.F., **1985**, Géotechnique, 35, 4, 471-481.
- Zetzener H., Schwedes J., **1998**, Preprints Partec, Nürnberg 10-12 March, Germany, 199-208.
- Zetzener H., Schwedes J., **2001**, Preprints Partec, Nürnberg 27-29 March, Germany, 1-8.

## Samenvatting

Processen waarin poeders en korrelvormige materialen verwerkt worden, vormen een belangrijk onderdeel van de industrie. De kennis over deze poederprocessen is echter vaak zeer gering omdat er weinig bekend is over het fundamenteel gedrag van poeders. Dit proefschrift heeft het stromingsgedrag van cohesief poeder tot onderwerp. Een typisch voorbeeld van de stroming van poeder vindt men in silo's. De fundamentele kennis op het gebied van poederstroming is gebaseerd op het werk van Jenike (1961, 1964) uit het begin van de jaren zestig en op de poedertester die hij ontwierp. Sinds die tijd zijn vele nieuwe poedertesters ontworpen, maar meestal gebruiken zij de principes die Jenike bedacht heeft, zoals bijvoorbeeld de yield locus. Deze beschrijft de kracht die nodig is om een poeder te breken - te laten stromen - als functie van de voorgeschiedenis van dat poedermonster. Deze definitie is een typisch voorbeeld van het gebrek in inzicht in de relatie tussen de microscopische eigenschappen van de deeltjes en het macroscopische gedrag van het poeder. Microscopisch gezien, bewegen en draaien de deeltjes terwijl ze contacten vormen met andere deeltjes. Hoe dat precies gebeurt, wordt beïnvloed door de deeltjesgrootte, de deeltjesvorm en het materiaal waaruit de deeltjes bestaan. De relatie tussen het microscopisch gedrag en het resulterende macroscopische poedergedrag is dus erg complex. De eerder gedefinieerde yield locus maakt geen gebruik van enige microscopische informatie en het is daarom niet verwonderlijk dat de yield locus niet volledig in staat is om poederstroming te beschrijven. Het doel van dit proefschrift is om de kennis over het stromen van cohesief poeder te vergroten en wel op het gebied van afschuifvlakken en de structuur in het poeder.

Als een poeder stroomt ontstaan er afschuifvlakken. Dat zijn de gebieden waarin de deeltjes het meest bewegen. In de literatuur (Scarlett et al., 1968) wordt als vuistregel voor de dikte van zo'n afschuifvlak 10 deeltjesdiameters aangenomen. In dit proefschrift is het afschuifvlak onderzocht met de Neutronendepolarisatie techniek die zeer veel informatie geeft over de rotatie van de deeltjes, de porositeit en de vorm en dikte van het afschuifvlak.

Er is bewezen dat een mengsel van cohesief BCR-kalksteen en 3 gewichtsprocent ferroxdure een afschuifvlak vormt dat 1000 tot 2000 deeltjesdiameters breed is. De deeltjes in dit afschuifvlak roteren evenredig met de opgelegde afschuiving en hebben een voorkeursrichting waarin ze draaien. Deze voorkeursrichting is in de richting waarin de afschuiving wordt aangebracht. Wanneer er alleen een consolidatie opgelegd wordt dan is de rotatie minder en bestaat er ook geen voorkeursrichting. De Neutronendepolarisatie techniek gaf aan dat het afschuifvlak lensvormig is, maar inspectie van het vlak na het experiment liet een golfvormig patroon zien. Dit

---

golfvormige patroon is ook door andere onderzoekers waargenomen. De aanname die vaak gedaan wordt in o.a. de Jenike Tester, dat het afschuifvlak horizontaal en vlak is, blijkt dus niet juist te zijn.

Het fundamenteel onderzoek naar het stromingsgedrag van poeders is uitgevoerd met de Flexible Wall Biaxial Tester (Kraan, 1996). Aangetoond is dat de consolidatiecurve voor een biaxiale consolidatie hoger ligt dan voor een uniaxiale consolidatie. Dit wordt veroorzaakt door een hogere schuifspanning in het poeder in het geval van een uniaxiale consolidatie, die er waarschijnlijk voor zorgt dat deeltjes makkelijker ten opzichte van elkaar bewegen. In vergelijking met de Braunschweig Biaxial Tester is gebleken dat de spreiding van de consolidatiecurves groot is. De relaties tussen de grootste en de kleinste principiële hoofdspanning komen echter goed overeen voor zowel de biaxial als de uniaxiale consolidatie.

De klassieke beschrijving van poederstroming gebeurt met de flow function. De standaard flow function voor BCR-kalksteen (Akers, 1992) blijkt af te wijken van de flow function die gemeten is met de Flexible Wall Biaxial Tester. Deze afwijking wordt veroorzaakt door tijdsconsolidatie in de Flexible Wall Biaxial Tester. De flow function bleek ook af te hangen van de tweede, tussenliggende, principiële spanning. De definitie van de unconfined yield strength is daarom incompleet omdat deze de hoogte van de tussenliggende principiële spanning niet definieert.

De flow function wordt ook beïnvloedt door anisotropie. Een draaiing van 90 graden van de grootste principiële hoofdspanning in de bepaling van de unconfined yield strength verlaagt de flow function. De huidige theorie kan dit niet verklaren en de reden hiervoor is dat een essentiële parameter in die theorie ontbreekt: de structuur die de deeltjes vormen in het poeder. Het effect van geïnduceerde anisotropie is aangetoond door verschillende vervormingen op te leggen aan het poeder terwijl het volume constant gehouden werd. Deze experimenten leverden sterke aanwijzingen dat het poeder zich inhomogeen gedraagt en daardoor de principiële spanningsassen lokaal niet overeen zouden kunnen komen met de principiële vervormingsassen. Hetzelfde verschijnsel is waargenomen door Wong en Arthur (1985) in niet cohesief zand. Om deze non-coaxialiteit in cohesief poeder te kunnen onderzoeken is een gespecialiseerde tester nodig.

De structuur in een matrix van deeltjes is onderzocht door deze deeltjes te simuleren met de software programma 3DSHEAR van Walton en Braun (1986a, 1986b). De resultaten van deze simulaties tonen aan dat het verschil tussen een biaxiale en een uniaxiale consolidatie van niet cohesieve deeltjes veroorzaakt wordt door de richtingsafhankelijkheid van de contactverdeling tussen de deeltjes. Ook een afschuifvlak is gesimuleerd, waaruit bleek dat de breedte van het afschuifvlak voor niet cohesieve deeltjes overeenkomt met de waarde gegeven in de literatuur. Hieruit blijkt dat de cohesie tussen deeltjes waarschijnlijk een belangrijke rol speelt in de vorming van een afschuifvlak.

Het onderzoek naar poederstroming zou zich moeten toespitsen op de structuur in poeder. De porositeit van een monster is een scalaire grootheid en kan niet de gehele structuur van het poeder beschrijven. De combinatie van simulaties van niet ronde deeltjes met de discrete elementen methode en de ontwikkeling van geavanceerde triaxiale testers zullen leiden tot het volledige begrip van poederstroming.



# Acknowledgement

Aangekomen bij het dankwoord is het werk van afgelopen vier jaar bijna afgerond. Het was voor mij een belangrijke en zeer leerzame periode. Op de eerste plaats wil ik daarvoor professor Scarlett bedanken. Ik ben u zeer dankbaar dat u mij de mogelijkheid geboden heeft om te promoveren. Uw enthousiasme en vertrouwen zijn voor mij een enorme stimulans geweest. Ik wens u veel succes in Florida met de volgende stap: de True Triaxial Tester.

De experimenten die uitgevoerd zijn op het Interfacultair Reactor Instituut hadden niet gedaan kunnen worden zonder medewerking van Wicher Kraan, Niels van Dijk en Theo Rekveldt. Hen wil ik bedanken voor de vele uitleg over deze techniek en voor hun inzet om dit onderzoek te laten slagen.

Two students helped me with the tedious experiments in the Flexible Wall Biaxial Tester and with lots of discussions. Andreas Raharja and Virgilio Spera, thank you very much for your effort. Gita Kamal was very friendly in showing me how to adapt the 3DSHEAR code to my wishes. Martin Koller worked, in an always cheerful mood, on the understanding of this code and on the visualization of the results. I want to thank Otis Walton for his assistance and permission to use the software code 3DSHEAR. Many thanks also go to the people of the Engineering Research Center of the University of Florida and their students for their hospitality during the Orange project. Marco Verwijs heeft veel bijgedragen aan dit uiteindelijke proefschrift, niet alleen met experimenten in de FWBT maar ook met veel discussie. Veel succes met het voort zetten van het werk op het gebied van poederstroming in je promotie onderzoek.

Seit der Konferenz in Nürnberg in 1998 habe ich viel diskutiert mit Professor Schwedes und Harald Zetzener. Professor Schwedes hat diese Zusammenarbeit immer gestützt, wofür ich ihm sehr dankbar bin. Harald, vielen Dank für Deine Gastfreundschaft und die guten Diskussionen über Schüttgut. Viel Glück für deine Promotion.

De werkgroep stortgoedtechnologie onder leiding van de heer De Jong wil ik bedanken voor de bijzonder interessante excursies naar de praktijk van de poedertechnologie.

Mijn onderzoek heb ik uitgevoerd in de deeltjesgroep in Delft. In de afgelopen vier jaar hebben daar veel bezoekers, studenten, promovendi en stafleden deel van uitgemaakt. Hen bedank ik allen voor de bijdrage die zij geleverd hebben aan de sfeer in de groep. Alexander, Wim, Damien, Hans en Martin als oude garde bedankt voor jullie adviezen. Ook Fieneke, Gabriele, Henk N., Herman, Renske en Wil veel dank

---

voor jullie hulp en Henk M. bedankt voor de vele goede raad tijdens de koffiepauzes. Met veel genoegen kijk ik terug op de wintersportvakantie met de groep in de Franse "sneu". Voor een zeer bijzondere collegialiteit en culinaire hoogstandjes wil ik de lunchgroep bedanken: Daan, Evelien, Flip en Kees. Evelien, ik heb het als een grote steun ervaren jou als kamergenoot te hebben gehad. Ik wens je samen met Daan en Kees veel succes met jullie promotie toe opdat we in de voetsporen van de - inmiddels senior - dr. Flip treden. Inmiddels heeft de deeltjesgroep een gedeeltelijke bezettingswisseling ondergaan en ik wil de groep veel succes wensen in de toekomst. Stefan Luding, ich wünsche Ihnen viel Erfolg bei der Arbeit mit dem FWBT.

Tijdens mijn promotie heb ik me altijd goed kunnen ontspannen met Pracque Attacque. Ik heb altijd met veel plezier met jullie djembe gespeeld en ik wil Pracque bedanken voor de vele mooie momenten en optredens. Gedurende de laatste loodjes hebben Ajiet, Evelien, Henk M., Marion en Noortje me bijgestaan met lezen en corrigeren. Erik T. heeft werkelijk iets schitterends uitgevoerd met een vakantiefoto resulterend in de kaft.

De altijd drijvende en steunende kracht achter alles wat ik doe, zijn mijn ouders en Robert. Hen wil ik bedanken voor hun nimmer aflatende begrip en stimulans. Dit proefschrift is voor jullie. Zum Schluß bedanke ich mich bei dir, Marion, für die viele Geduld und das viele hin und her Reisen. Besos y abrazo fuerte!

Richard Janssen

## Curriculum vitae

Richard Janssen was born on the 10<sup>th</sup> of February in 1972 in Margraten, The Netherlands.

- |           |  |
|-----------|--|
| 1984-1990 | Lyceum, Coriovallum College, Heerlen.  |
| 1990-1996 | Chemical Engineering, Delft University of Technology, Delft.                     |
| 1997-2001 | Ph.D. student, Particle Technology Group, Delft University of Technology, Delft. |
| 2001      | DSM Research, Centre for Particle Technology, Geleen.                            |

---

---



ISBN 90-407-2241-2  
DUP Science